

University of Windsor

## Scholarship at UWindor

---

Electronic Theses and Dissertations

Theses, Dissertations, and Major Papers

---

10-1-2017

# Thermal Modeling and Optimization of Lithium-Ion Batteries for Electric Vehicles

Maryam Ghalkhani  
*University of Windsor*

Follow this and additional works at: <https://scholar.uwindsor.ca/etd>

---

### Recommended Citation

Ghalkhani, Maryam, "Thermal Modeling and Optimization of Lithium-Ion Batteries for Electric Vehicles" (2017). *Electronic Theses and Dissertations*. 7260.

<https://scholar.uwindsor.ca/etd/7260>

This online database contains the full-text of PhD dissertations and Masters' theses of University of Windsor students from 1954 forward. These documents are made available for personal study and research purposes only, in accordance with the Canadian Copyright Act and the Creative Commons license—CC BY-NC-ND (Attribution, Non-Commercial, No Derivative Works). Under this license, works must always be attributed to the copyright holder (original author), cannot be used for any commercial purposes, and may not be altered. Any other use would require the permission of the copyright holder. Students may inquire about withdrawing their dissertation and/or thesis from this database. For additional inquiries, please contact the repository administrator via email ([scholarship@uwindsor.ca](mailto:scholarship@uwindsor.ca)) or by telephone at 519-253-3000ext. 3208.

# **Thermal Modeling and Optimization of Lithium-Ion Batteries for Electric Vehicles**

by

**Maryam Ghalkhani**

A Dissertation

Submitted to the Faculty of Graduate Studies  
through the Department of Electrical and Computer Engineering  
in Partial Fulfillment of the Requirements for  
the Degree of Doctor of Philosophy  
at the University of Windsor

Windsor, Ontario, Canada

2017

© 2017 Maryam Ghalkhani

# **Thermal Modeling and Optimization of Lithium-Ion Batteries for Electric Vehicles**

by

Maryam Ghalkhani

APPROVED BY:

---

C. Wang, External Examiner

Wayne State University

---

A. Fartaj

Department of Mechanical, Automotive and Materials Engineering

---

M. Ahmadi

Department of Electrical and Computer Engineering

---

R. Rashidzadeh

Department of Electrical and Computer Engineering

---

M. Saif, Advisor

Department of Electrical and Computer Engineering

---

G-A. Nazri, Co-Advisor

Department of Electrical and Computer Engineering

---

September 8, 2017

## DECLARATION OF CO- AUTHORSHIP/PREVIOUS PUBLICATION

---

### *I. Co-Authorship Declaration*

I at this moment declare that this thesis incorporates material that is the result of joint research.

This thesis contains the outcome of an investigation undertaken by me under the supervision of *Dr. Mehrdad Saif* and *Dr. Gholam-Abbas Nazri*. The collaboration is covered in Chapters 3, 4 and 5 of the thesis. The measurements presented in chapter 3 were the results of collaboration with *Dr. Narayan Kar* and my supervisors *Dr. Mehrdad Saif* and *Dr. Gholam-Abbas Nazri*. The mathematical models and simulation results presented in chapter 4, and 5 were the outcome of the research undertaken in collaboration with my lab colleague *Farid Bahiraei* and my supervisors. In all cases, the key ideas, first contributions, experimental measurements, simulation, data analysis, and interpretation, were performed by the author of this thesis, and the input of co-authors was primarily through the provision of valuable suggestions and help in the comprehensive analysis of the experimental results submitted for publication.

I am aware of the University of Windsor Senate Policy on Authorship, and I certify that I have correctly acknowledged the contribution of other researchers to my thesis, and have permission from each of the co-author(s) to include the above material(s) in my thesis. I certify that, with the above qualification, this thesis, and the research to which it refers, is the product of my work.

## ***II. Declaration of Previous Publication***

This thesis includes original papers that have been previously published/submitted for publication in peer-reviewed conferences and journals, as follows:

<b>Thesis Chapter</b>	<b>Publication title/full citation</b>	<b>Publication status</b>
Chapter 3	<b>M. Ghalkhani</b> , G-A. Nazri, NC. Kar and M.Saif, Heat response of prismatic Li-ion cells, ITEC 2014	Published
Chapter 4	<b>M. Ghalkhani</b> , F. Bahiraei, G-A. Nazri and M.Saif, Experimental and Numerical Investigation of Electrochemical–Thermal Behavior of a Prismatic Lithium-Ion Battery, MRS 2016	Published
	<b>M. Ghalkhani</b> , F. Bahiraei, G-A. Nazri and M.Saif, Electrochemical–Thermal Model of Pouch-type Lithium-ion Batteries, <i>Electrochimica Acta - Journal of Elsevier</i> , 2017	Published
Chapter 5	<b>M. Ghalkhani</b> , F. Bahiraei, G-A. Nazri and M.Saif, Modeling and Experimental Analysis of Lithium-ion Battery Key Parameters, <i>Electrochimica Acta - Journal of Elsevier</i> , 2017	Submitted

I certify that the above material describes work completed during my registration as a graduate student at the University of Windsor.

I declare that, to the best of my knowledge, my thesis does not infringe upon anyone's copyright nor does it violate any proprietary rights and that any ideas, techniques, quotations, or any other material from the work of other people included in my thesis, published or otherwise, are fully acknowledged in accordance with the standard referencing practices. Furthermore, to the extent that I have included copyrighted material that surpasses the bounds of fair dealing within the meaning of the Canada Copyright Act, I certify that I have obtained written permission from the copyright owner(s) to include such material(s) in my thesis. I declare that this is an actual copy of my thesis, including any final revisions, as approved by my thesis committee and the Graduate Studies office and that this thesis has not been submitted for a higher degree of any other University or Institution.

## ABSTRACT

---

This dissertation contributes to the modeling and optimization of Lithium-ion battery's thermal management for electrified vehicles (EVs). EVs in automotive technology is one of the principal solutions to today's environmental concerns such as air pollution and greenhouse impacts.

Light duty and heavy duty EVs can decrease the amount of the pollution efficiently. EV's receive their power from installed rechargeable batteries in the car. These batteries are not just utilized to power the car but used for the functioning of lights, wipers and other electrical accessories. The Lithium-ion batteries (LIBs) have attracted a lot of research interest in recent years, due to their high potential as compared to the conventional aqueous based batteries, high gravimetric and volumetric energy density, and high power capability. However, Li-ion batteries suffer from high self-heating, particularly during high power applications and fast charging, which confines their lifetime and cause safety, reliability and environmental concerns. Therefore, the first part of this study consists of the experimental investigation of the charge-discharge behavior and heat generation rate of lithium ion cells at different C-rates to monitor and record the thermal behavior of the cell. A further concern regarding LIBs is strongly dependent on the quality and efficiency of battery thermal management system. Hence, this is extremely important to identify a reliable and accurate battery management system (BMS). Here in the second part, we show that thermal management and the reliability of Li-ion batteries can be drastically improved using optimization technique.

Furthermore, a LIB is a compact system including high energy materials which may undergo thermal runaway and explode the battery if overcharged due to the decomposition of battery materials within the electrolyte and electrodes that generate flammable gaseous species. The application of this kind of technology needs many laboratory experiments and simulations to identify the fundamental thermal characteristics of the system before passing it to the real use. An accurate battery model proposes a method to simulate the complex situations of the system without performing time consuming actual tests, thus a reliable scheme to identify the source of heat generation and required parameters to optimize the cell performance is necessary.

For this reason, the latest phase of this research covers the development and comparison of a model based on adjustable design parameters to predict and optimize battery performances. This kind of model provides a relationship with the accuracy and simplicity to estimate the cell dynamics during charge and discharge.



## DEDICATION

---

*To my parents and sibling who always encouraged for higher studies and remembered me in their prayers.*

*To my family and friends who provided emotional support throughout the period of this research.*

*To all my teachers and mentors, who trusted me with my abilities, guided me and provided me with the knowledge to undertake doctorate level research.*

## ACKNOWLEDGMENTS

---

First of all, I would like to thank Almighty God for His blessing, mercy upon me and His support to complete this thesis. I would like to offer my heartiest gratitude to my supervisors *Dr. Mehrdad Saif* and *Dr. Gholam-Abbas Nazri* for their invaluable advice, guidance, and support on my research, without which, I could not have achieved this precious degree. I am incredibly grateful to them for their academic, moral and emotional support. It has been a great honor to learn from them and work with them. I have received persistent inspiration, great advocacy, valuable suggestion, and compassionate attitude from them throughout my research. I would also like to thank *Dr. Majid Ahmadi*, *Dr. Rashid Rashidzadeh* and *Dr. Amir Fartaj* for serving on my committee, and helping me with their valuable suggestions and contributions for the improvement of this work. I would like to thank *Farid Bahiraei* my fellow graduate student and colleague of Battery Research Lab at University of Windsor for sharing his thoughts and ideas and having a wonderful time throughout this research. I would also like to acknowledge the support I have received from many teachers and staff members of Department of Electrical and Computer Engineering, especially to *Andria Ballo* for her administrative advice and support throughout the period of my research. I would like to thank my friends who helped me academically or socially during my study at the University of Windsor. Moreover, I would like to thank my parents for their consistent support and encouragement throughout the duration of my doctorate.

# TABLE OF CONTENT

---

Declaration of Co- Authorship/Previous Publication.....	III
Abstract.....	VI
Dedication.....	VIII
Acknowledgments .....	IX
List of tables .....	XIV
List of figures.....	XV
List of abbreviations .....	XIX
Nomenclature.....	XX
<b>Chapter 1</b> .....	<b>1</b>
<b>Introduction and Literature Review</b> .....	<b>1</b>
1.1 Background.....	1
1.2 Challenges in LIBs.....	3
1.3 Motivation for This Dissertation.....	5
1.4 Dissertation Objectives .....	6
1.5 Dissertation Layout.....	7
1.6 References.....	9
<b>Chapter 2</b> .....	<b>11</b>
<b>COMSOL Overview</b> .....	<b>11</b>
2.1 Introduction.....	11
2.2 Materials .....	12
2.3 The Geometry Node.....	13
2.4 The Lithium-ion battery interface.....	14

2.5	The ODE and DAE Interfaces .....	15
2.6	The Heat Transfer in Solids Interface .....	17
2.7	Meshing.....	18
2.8	Study .....	19
2.9	References.....	20
<b>Chapter 3</b> .....		<b>21</b>
<b>Heat Response of Prismatic Li-ion Cells</b> .....		<b>21</b>
3.1	Summary.....	21
3.2	Introduction.....	21
3.3	Geometry and operating conditions .....	23
3.4	Experimental setup and results .....	26
3.5	Conclusion .....	31
3.6	Reference .....	32
<b>Chapter 4</b> .....		<b>33</b>
<b>Electrochemical–Thermal Model of Pouch-type Lithium-ion Batteries</b> .....		<b>33</b>
4.1	Summary.....	33
4.2	Introduction.....	34
4.3	Experimental Study.....	38
4.3.1	Experimental setup.....	38
4.3.2	Experimental results.....	42
4.4	Model development .....	47
4.4.1	Electrical model .....	48
4.4.2	Thermal model .....	52
4.4.3	Simulation results.....	54

4.4.4	3D electrochemical –thermal model .....	61
4.5	Conclusion .....	72
4.6	Acknowledgments.....	73
4.7	Reference .....	73
<b>Chapter 5</b>	.....	<b>77</b>
<b>Modeling and Experimental Analysis of Lithium-ion Battery Key Parameters</b>	.....	<b>77</b>
5.1	Summary.....	77
5.2	Introduction.....	78
5.3	Experimental .....	81
5.4	Model description .....	86
5.5	Mathematical modeling .....	89
5.5.1	Electrochemical Kinetic at the interface .....	91
5.5.2	Charge conservation.....	91
5.5.3	Electron transport in the solid phase and lithium ion transport in the electrolyte phase.....	93
5.5.4	Mass conservation.....	93
5.5.5	Energy balance.....	94
5.5.6	Estimation of Battery State of Charge (SOC).....	96
5.6	Numerical method.....	98
5.7	Results and discussion .....	100
5.8	Conclusions.....	125
5.9	Acknowledgement .....	126
5.10	References.....	127
<b>Chapter 6</b>	.....	<b>132</b>
<b>Conclusions and Future Research Directions</b>	.....	<b>132</b>

6.1	Summary of thesis.....	132
6.2	Suggested Future Work.....	133
<b>Vita Auctoris</b>	.....	135

## LIST OF TABLES

---

Table 3.1. Physical properties of materials [9]. .....	27
Table 4.1. Specifications of the commercial $\text{LiNiCoAlO}_2$ .....	39
Table 4.2. Model parameter in different regions. ....	42
Table 5.1. Characteristics of the LP6745135-10C-type LIB. ....	82
Table 5.2. Model parameter in different regions. ....	99

## LIST OF FIGURES

---

Figure 1.1. Several battery technologies comparison regarding volumetric and gravimetric energy density [1]. .....	2
Figure 2.1. Screenshot from COMSOL desktop.....	11
Figure 2.2. Add material, the batteries & fuel cells material library, and settings windows. 12	
Figure 2.3. The geometry setting view. ....	14
Figure 2.4. The Lithium-ion battery node interface.....	15
Figure 5.5. The ODE and DAE Interfaces windows. ....	16
Figure 2.6. The Heat Transfer in Solids Interface. ....	17
Figure 2.7. Adding, Editing, and Building Meshing Sequences.....	18
Figure 2.8. Study configuration. ....	20
Figure 3.1. Multi-folded-layer structure of a prismatic cell [7].....	24
Figure 3.2. Two parallel Li-ion cells (GMB 654765).....	26
Figure 3.3. Charge and discharge voltage profile for two parallel cells (C/2-rate). ....	27
Figure 3.4. Temperature behavior of the battery pack with two parallel cells (C/2 rate), graphs indicate thermal response of thermocouple at 1) close to the tab, 2) at the center, and 3) at the bottom of the cell. ....	28
Figure 3.5. Charge and discharge voltage profile of a single cell (C/2-rate) during first three charge and discharge cycles.....	29
Figure 3.6. Temperature & voltage behavior of a single cell vs Time at C-rate. ....	30
Figure 3.7. Temperature & Voltage vs Time at C/2 rate for a single cells. ....	30
Figure 4.1. The stacked structure of the actual experimental battery with the pouch case. ..	40
Figure 4.2. The experimental setup with the measuring T-type thermocouples and voltage sensors attached to the batteries surface and tabs, respectively.....	41
Figure 4.3. Surface temperature profiles at a) 0.1 C-rate, b) 0.5C-rate and c) 0.8C-rate. d) Temperature is measured closed to the positive tab (T1, blue lines), close to the negative tab	



(T2, orange lines), center (T3, red lines) and at the bottom of the battery (T4, yellow lines)..... 44

Figure 4.4. Current and voltage profiles versus time during charge and discharge containing a short rest period of 5 minutes at 0.8 C-rate..... 45

Figure 4.5. Experimental data on the variation of battery voltage versus capacity for different discharge conditions in C-rate. .... 46

Figure 4.6. Schematic of a unit cell of the battery including positive and negative porous electrodes, a porous separator, and current collectors during charge and discharge process.49

Figure 4.7. Charge/Discharge current and voltage at 0.8C as a function of time. .... 55

Figure 4.8. a) Comparison of over potential and electrolyte potential at the beginning and end of discharge. b) Electrolyte concentration outline at different times..... 57

Figure 4.9. Local current density distribution within the battery during the discharge at various times..... 58

Figure 4.10. Concentration distribution of lithium in the solid particle. .... 59

Figure 4.11. Comparison of simulation results to experimental during the discharge constant current at 0.5 and 0.8 C-rates. a) Variation of battery open circuit voltage versus time. b) Average surface temperature profiles of the battery. Symbols correspond to measured values and lines represent the calculated values. .... 62

Figure 4.12. a) Temporal evaluation of ohmic heat and entropic heat at the end of discharge process. b) The total heat generated within the battery during charge/discharge process. .... 64

Figure 4.13. a) Schematic of a single cell unit assembly. b) Geometry of the computational domain (electrode-separator stack) of a pouch-type 3D LIB consisting of 18 double layers cells. .... 65

Figure 4.14. a) The electrode current density vector within the battery (red streamlines) is shown the current enter into the negative tab and exit to positive tab during the discharge process (t=55 min). b) The electrode current density magnitude within the battery is shown using contours. .... 66

Figure 4.15. Electric potential distribution on the positive current collector during the discharge process at 0.8C: a) after 10 seconds, b) after 30 minutes, and c) after 55 minutes..... 67

Figure 4.16. Surface temperature distribution from based battery model during the discharge at 0.8C constant current. a) After 1 minute. b) After 30 minutes. c) After 55 minutes. d) From four different locations (close to the positive tab, close to the negative tab, center of the battery

and bottom of the battery) are shown to validate the time dependent temperature results obtained from the 3D model. .... 69

Figure 4.17. 3D model performance validation: a) calculated average surface temperature profile of the battery at 0.8C constant current is compared to experimental temperature measurement, b) calculated OCV voltage response of the battery during constant-current di discharge process at 0.8C rate validated by experimental OCV measurement. .... 71

Figure 5.1. a) The stacked structure of the original experimental battery with the pouch case. The cell is constructed from 40 double side coated plates making 20 cells connected in Parallel. b) Simplified schematic layout of a prismatic cell. .... 83

Figure 5.2. a) XRD analysis of anode and the cathode. b) XRD Reference for layered oxide cathode. .... 84

Figure 5.3. a) Current and voltage profiles versus time during charge and discharge containing a rest period of 30 minute at different C-rates. b) Characteristics of the cell voltage variation during discharge period and rest period. .... 85

Figure 5.4. a) Schematic of a unit cell of the battery including positive and negative porous electrodes, a porous separator, and current collectors during charge and discharge process. b) The electrical equivalent circuit of a cell including open-circuit-voltage, cell ohmic resistance  $R_{int}$  and  $R_p$  and  $C_p$  of the RC-circuit. .... 87

Figure 5.5. Comparison of simulation and experimental measured Cell voltage at various rates. The thin solid lines are displaying the simulation results, and the thicker connected markers are showing the experimental data; a) without film resistance, and b) with film resistance. .... 102

Figure 5.6. Comparison of measured OCV against time with simulation results at 0.5C and 1C rates during the discharge process. .... 104

Figure 5.7. a) Estimated total polarization (voltage difference) against time at different current rates. b) Calculated changing the trend of internal resistance at various current rates. c) Comparison of the experimental and simulated average cell temperature during different discharge rates. d) Effect of current rate on internal resistance and mean temperature evolution. .... 107

Figure 5.8. Electrolyte lithium concentration profile at 4C discharge rate: a) across the cell, b) at the positive electrode, c) at the negative electrode. c) Solid lithium concentration across the cell at 4C discharge rate. .... 110

Figure 5.9. Comparison of the measured and simulation data at various rates. Markers are measured data, and solid lines are simulation results. a) Ragone plot. b) Effect of current rate on decreasing energy and rising power. .... 112

Figure 5.10. Influence of various current value on total polarization and energy efficiency evolutions..... 113

Figure 5.11. Effect of various initial SOC at 4C rate on: a) Discharge voltage and open circuit voltage characteristics, b) Total polarization, c) Internal resistance, and d) Energy efficiency..... 116

Figure 5.12. a) Averaged internal resistance and polarization value at various SOC. b) Battery charge acceptance indicating the slope of recharge currents at different SOC levels. .... 117

Figure 5.13. Effect of different particle size value of the positive electrode material at SOC of 100%: a) polarization and b) Internal resistance evolutions. Effect of different porosity value of the positive electrode at various SOC on: c) polarization and d) internal resistance evolutions. The dashed lines are the original value from the experimental cell..... 120

Figure 5.14. Variation of polarization and resistance as a function of: a) porosity and b) particle size. .... 122

Figure 5.15. Cell response comparison at different design parameters: a) polarization, b) internal resistance. The dashed lines are actual parameters, solid lines are combination of actual parameters and estimated parameters, dashed lines with markers are estimated parameters. c) Comparison of energy efficiency against SOC. d) Comparison of specific energy versus specific power of the cell including actual design parameters and estimated parameters. .... 124

## LIST OF ABBREVIATIONS

---

Battery management system	: BMS
Battery thermal management system	: BTMS
Current collector	: CC
Depth of discharge	: DOD
Electrified vehicles	: EVs
Electrochemical-thermal	: ECT
Finite Elements Method	: FEM
Hybrid electric vehicles	: HEVs
Infrared Camera Incorporation	: ICI
Lithium-ion batteries	: LIBs
One-dimensional	: 1D
Phase change material	: PCM
State of charge	: SOC
State of health	: SOH
Three-dimensional	: 3D
X-ray Diffraction	: XRD

## NOMENCLATURE

---

$A$	: battery surface area ( $m^2$ )
$a_v$	: active specific surface
$a_{v,dl}$	: double layer area ( $m^{-1}$ )
$Bi$	: Biot number
$C_{dl}$	: electrical double layer capacitance ( $F.m^2$ )
$c_s$	: lithium concentration on the surface ( $mol.m^{-3}$ )
$c_{s,avg}$	: average species concentration ( $mol.m^{-3}$ )
$c_{s,avg,cycl}$	: average cyclable lithium concentration ( $mol.m^{-3}$ )
$c_{s,max}$	: maximum lithium concentration ( $mol.m^{-3}$ )
$c_{s,surf}$	: surface species concentration ( $mol.m^{-3}$ )
$c_{s,surf,cycl}$	: cyclable surface species concentration ( $mol.m^{-3}$ )
$c_l$	: electrolyte salt concentration ( $mol.m^{-3}$ )
$c_{l,ref}$	: electrolyte reference concentration ( $mol.m^{-3}$ )
$C_p$	: heat capacity of the battery ( $J.kg^{-1}.K^{-1}$ )
$C_R$	: reduced species expression ( $mol.m^{-3}$ )
$C_O$	: oxidized species expression ( $mol.m^{-3}$ )
$D_s$	: Intercalation diffusivity ( $m^2.s$ )
$D_{l,eff}$	: effective electrolyte salt diffusivity ( $m^2.s^{-1}$ )
$E$	: specific energy ( $Wh.kg^{-1}$ )
$E_{eq}$	: open circuit potential ( $V$ )
$F$	: Faraday's constant ( $C.mol^{-1}$ )
$\Delta G$	: Gibbs energy change ( $J.K^{-1} mol^{-1}$ )
$h$	: convection heat transfer coefficient ( $W.m^{-2}K^{-1}$ )
$h_{tab}$	: tab's height ( $mm$ )
$i_l$	: electrolyte ionic current density ( $A.m^{-2}$ )
$i_s$	: electrical current density ( $A.m^{-2}$ )
$i_{loc}$	: local charge transfer current density ( $A.m^{-2}$ )

$i_0$	: exchange current density ( $A.m^{-2}$ )
$i_{total}$	: total interface current density ( $A.m^{-2}$ )
$i_{v,total}$	: total electrode reaction current density ( $A.m^{-3}$ )
$i_{v,m}$	: electrode reaction current density ( $A.m^{-3}$ )
$i_{dl}$	: double layer current density ( $A.m^{-2}$ )
$i_{v,dl}$	: double layer current source ( $A.m^{-3}$ )
$K$	: ionic conductivity ( $S.m^{-1}$ )
$k$	: thermal conductivity ( $W.m^{-1}.K^{-1}$ )
$k_a$	: anodic rate constant ( $m.s^{-1}$ )
$k_c$	: cathodic rate constant ( $m.s^{-1}$ )
$K_{T,x}$	: thermal conductivity in the x direction ( $W.m^{-1}.K^{-1}$ )
$K_{T,y}$	: thermal conductivity in the y direction ( $W.m^{-1}.K^{-1}$ )
$K_{T,i}$	: thermal conductivity of different layers ( $W.m^{-1}.K^{-1}$ )
$l_c$	: characteristic length (cell volume/surface area)
$M$	: battery mass ( $kg$ )
$n$	: the charge number pertaining to the reaction
$N_l$	: flux of lithium ions
$P$	: specific power ( $W.kg^{-1}$ )
$\dot{q}_{entropy}$	: volumetric heat generation ( $W.cm^{-3}$ )
$Q_{pol}$	: polarization heat generation ( $W.cm^{-3}$ )
$Q_{ohm}$	: ohmic heat generation ( $W.cm^{-3}$ )
$Q_{rea}$	: reaction heat generation ( $W.cm^{-3}$ )
$\dot{q}_{entropy}$	: volumetric heat generation ( $W.cm^{-3}$ )
$R$	: gas constant, ( $J.mol^{-2} K^{-1}$ )
$R_{int}$	: internal resistance ( $m\Omega$ )
$R_{film}$	: film resistance ( $\Omega.m^2$ )
$r_p$	: particle size ( $m$ )
$f_{\pm}$	: average molar activity coefficient
$\Delta S$	: entropy change ( $J.K^{-1}$ )

$t$	: time ( $s$ )
$t_+$	: transference number of lithium ions
$T$	: cell temperature ( $K$ )
$T_a$	: ambient temperature ( $K$ )
$V$	: potential of each electrode ( $V$ )
$V_{cell}$	: voltage of Li-ion battery ( $V$ )
$V_{oc}$	: open circuit voltage ( $V$ )
$W_{out}$	: energy output ( $J$ )
$W_{in}$	: energy input ( $J$ )
$w_{tab}$	: tab's width ( $mm$ )

**Greek letters:**

$\alpha_a$	: anodic charge transfer coefficient
$\alpha_c$	: cathodic charge transfer coefficient
$\varepsilon_s$	: electrode volume fraction
$\varepsilon_l$	: electrolyte volume fraction
$\rho$	: density of the battery ( $kg.m^3$ )
$\rho_i$	: density of the different layers of the cell( $kg.m^3$ )
$\Phi_s$	: solid phase potential ( $V$ )
$\Delta\Phi_{s,filtn}$	: solid phase film potential ( $V$ )
$\Phi_l$	: electrolyte phase potential ( $V$ )
$\gamma$	: Bruggeman tortuosity exponent
$\sigma_s$	: electrical conductivity ( $S.m^{-1}$ )
$\sigma_s^{eff}$	: effective conductivities of the solid phase ( $S.m^{-1}$ )
$\sigma_l^{eff}$	: effective conductivity of the electrolyte phase ( $S.m^{-1}$ )
$\eta$	: local surface overpotential ( $V$ )
$\eta_e$	: energy efficiency
$\omega$	: frequency

# CHAPTER 1

## INTRODUCTION AND LITERATURE REVIEW

---

### *1.1 Background*

Throughout the past few centuries, we have been dependent on fossil fuels to power our industries, and transportation. The limited fossil fuel resources, and environmental issues associated with the release greenhouse gases, as well as complexity of socio-political aspects of fossil fuels, have forced the nations to search for a sustainable, affordable alternative energy sources, and non-zero emission technologies.

Developing electric vehicles could decrease the amount of carbon dioxide in the atmosphere since they can operate on clean and environmentally friendly energy sources. Consequently, replacing the combustion engine powered by fossil fuel with the electric vehicular technology provides a feasible solution to improve the global warming problem, limits the emission of toxic hydrocarbons and its by-products in the atmosphere.

Considering the current transportation system based on combustion engine with very low efficiency as one of the most polluting technology, the electric vehicles that run on energy storage device such as battery may provide a practical solution as they are conceptually simple and sound.

Lithium-ion batteries are one of the most promising technology since these systems have shown excellent performance on board of a vehicle, and they are environmentally friendly



system with long lifespan as compared with other battery technologies. Additionally, LIBs are offering further advantages such as capability of rapid charging, and very low self-discharge. Therefore, these traits are quickly developing LIBs as the preferred rechargeable battery and maintain the dynamism of EVs [5-8].

One major advantage of lithium battery is that the lithium is the most lightweight metal in the periodic table, as illustrated in Figure 1.1 and it has very high electrochemical potential which can produce the greatest specific energy per weight. Hence, LIBs have properties of high energy and power density against other types of batteries, and are well-suited for automotive applications [5, 6, 9, 10].

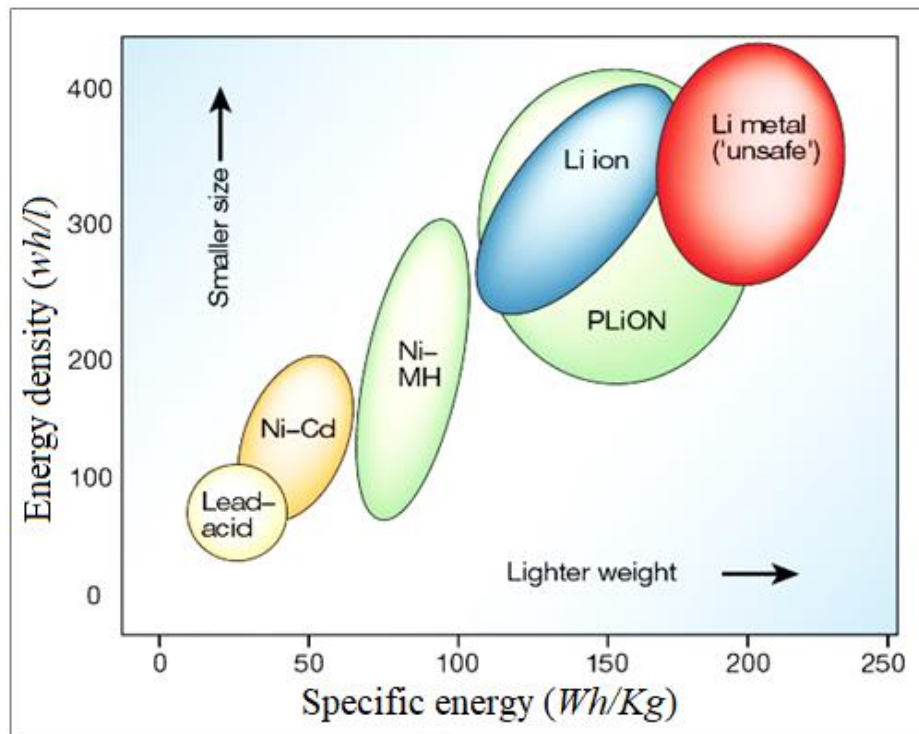


Figure 1.1. Several battery technologies comparison regarding volumetric and gravimetric energy density [1].

The existing LIBs are in multiple forms such as coin, cylindrical, and prismatic types. Prismatic LIBs have high potential power output and high packing factor than the other types. Furthermore, the battery electrochemical materials in prismatic types are made in parallel layers. Their large surface area offers an advantage in thermal management because of minimum temperature gradient in the thickness of the battery which makes them well-suited to particular automotive applications.

## ***1.2 Challenges in LIBs***

The strategy for electrifying vehicles with high power batteries is one of the most significant challenges that call for the development of LIB technology. Since a lithium-ion battery is a compressed energy storage device that contains high energy materials, it may generate high heat during overcharge and at high power applications causing thermal runaway that leads to cell explosion [11].

The active materials in the lithium ion battery are the negative electrodes that contains carbonaceous material in most of the commercial lithium cells, and the positive electrode that contains mixed transition metal oxides or metal phosphates and silicates.

Many studies have been devoted in discussing the performance of LIB's using different cathode material. The common positive electrode material in lithium-ion batteries could be Lithium manganese oxide  $\text{LiMn}_2\text{O}_4$  (LMO), Lithium iron phosphate  $\text{LiFePO}_4$  (LFP), Lithium cobalt oxide,  $\text{LiCoO}_2$  (LCO), Lithium nickel-cobalt-manganese oxide  $\text{LiNiMnCOO}_2$  (NCM), Lithium nickel cobalt aluminum oxide  $\text{LiNi}_{0.8}\text{Co}_{0.15}\text{Al}_{0.05}\text{O}_2$  (NCA) [12-20].

The lithium ion battery materials are not highly conductive, and may induced Ohmic losses, particularly at high current drainage. The ohmic drops in the matrix of active material phases, contact resistances between the current collector and the porous active material, and transport limitations of lithium ions in the electrode and electrolyte phases, causes restriction of the power capability of the lithium iron [21].

The Lithium cobalt oxide has been used in the first Sony cells, and due to the high cost of lithium cobalt oxide, a lower cost nickel oxide based cathode has been introduced. However, due to instability of pure lithium nickel oxide, the mixed oxides cathode such as NCA has been developed as a practical candidate for commercial cells used for EVs applications [20]. Since the primary source of heat generation in the Li-NCA cells is the lithium transport in cathode, the performance of the cathode electrode has to be improved by improving its electronic conductivity. The thermal characteristics of lithium batteries with different combinations of anode and cathode have been reported. However, Newman introduced the first LIB thermal modeling for the development of a battery thermal management system [13, 22].

The internal cell resistance is a dynamic [parameter and is influenced by several parameters such as the state of charge (SOC), the cell initial temperature, and the current rate of charge or discharge. The internal resistance is resulting from an electric current through an ohmic resistive components of the electrode or the electrolyte which is significantly affect the battery performance during the charge-discharge process [23]. Park was found the cell component variables particularly the cathode thickness has the greatest impact on the charging time of Lithium-ion cells [24].

### *1.3 Motivation for This Dissertation*

Although, the LIB is one of the technologies of choice for EV development in the coming years; the battery-powered vehicles just could not satisfy the high energy/high power demand and most EVs are limited in range. In addition, use of lithium ion battery for high power application, such as vehicle start up, acceleration and hill climbing is challenging, due to its issues with battery safety, durability, and cycle life.

The EV's performance is essentially depending on the battery power/energy ratio. The rechargeable lithium-ion batteries are still the most attractive proposition to be used in high-performance EV's as compared to other types of batteries, yet its operation restricted within the safe and reliable operating temperature and voltage windows. The performance of the LIBs diminishes in higher temperatures quickly, and its power capability is very limited at low temperatures ( $<10^{\circ}\text{C}$ ). The heat generation due to Joule heating inside the battery pack is much greater at higher currents. Therefore, a dedicated battery thermal management system (BTMS) is required to maintain the battery temperature within the desirable range to achieve the optimal vehicle performance. This research is motivated by the idea to improve a fundamental understanding of heat generation inside a battery and its effect on the battery operation, and assign a proper temperature control, and cell design optimization using electrochemical-thermal simulation.

To accomplish this aim, a series of modeling studies are developed to predict the transient distribution of electro-thermal behavior of the battery at different operating conditions. The results have been confirmed with the experimental measurement to evaluate and improve the

amount of heat generation at the cell level. Accordingly, the model can be extended to a module/pack level to compose a computationally effective multi-physics BTMS.

#### ***1.4 Dissertation Objectives***

Thermal concerns of the electric vehicles are all associated with the battery performance. Hence, a strong battery thermal models are required to predict the fundamental heat transfer and heat distribution in the cell, cell performance characteristics in a wide temperature range, to design an efficient thermal management system for variety of charge/discharge conditions. The final mathematical model for BTMS design should be computationally affordable to be applied for the development of cell, module and the battery pack.

The main objective of this dissertation is to describe and simulate the thermal response of the prismatic LIB under real operating conditions at the various current rates to achieve an optimal cell design.

More specifically, these purposes involve the following steps:

- To develop experiment protocols to collect the data required for generating the multi-physics models that can predict the battery performances.
- To develop an in-depth perception of heat distribution of temperature and current density profiles across the Li-ion batteries under various current loads.
- To develop the interaction between the electrochemical and thermal behavior of Li-ion batteries under different current rates.

- To develop a computationally dynamic modeling approach from full numerical to analytical models to optimized cell energy and power delivery that can be implemented in BTMS design.
- To provide experimental data base required for the modeling and validation of to validate the proposed models, a battery testing procedure was used in the battery laboratory of the University of Windsor.

The main components of the battery test-set are:

- A battery cycler (MACCOR model 4300) for charge/discharge of the battery.
- A small chamber to maintain the cell temperature within desirable range.
- An Infrared Camera Incorporation (ICI) P9000 to capture real-time thermal images.
- T-type thermocouples placed in different locations to measure the surface temperature.

### ***1.5 Dissertation Layout***

This thesis provides a study of modeling and optimization of Lithium-ion battery's thermal management for EVs as follow:

The first chapter is introducing the research importance and the multiple objective functions of the proposed BMS and the optimization scheme.

The capability and functionality of the COMSOL Multiphysics software to solve the equations using the Finite Elements Method (FEM) have been introduced in the second chapter.

A series of experimental studies have been performed to evaluate the battery performance and its heat distribution rate at various current rates in chapter 3.

In chapter 4, the electrochemical-thermal characteristics of a battery have been studied using a one-dimensional multiphysics model. The model has been extended to a three-dimensional layer structure of the pouch-type cell to fully understand the distribution of temperature and current density across the LIBs.

Chapter 5 discusses different prediction of the polarization and corresponding internal resistance of the lithium-ion cell to predict cell energy and power delivery. The introduced method presents the opportunity to obtain an optimal cell operation specifications.

Chapter 6 concludes this dissertation with a comprehensive review of the contributions to offers some ideas for the future works.

## 1.6 References

- [1] J.-M. Tarascon, M. Armand, Issues and challenges facing rechargeable lithium batteries *Nature*, 414 (2001) 359-367.
- [2] R. Heng, Z.M. Razlan, Review of the most recent literature on lithium-ion polymer battery for electric car, *Int. J. Emerg. Technol. Adv. Eng*, 5 (2015).
- [3] M.R. Khan, M.J. Swierczynski, S.K. Kær, Towards an Ultimate Battery Thermal Management System: A Review, *Batteries*, 3 (2017) 9.
- [4] E. Gümüŝsu, *Thermal Modeling of Lithium Ion Batteries*, Fen Bilimleri Enstitüsü, 2017.
- [5] D. Bernardi, E. Pawlikowski, J. Newman, A general energy balance for battery systems, *Journal of the electrochemical society*, 132 (1985) 5-12.
- [6] T.M. Bandhauer, S. Garimella, T.F. Fuller, A critical review of thermal issues in lithium-ion batteries, *Journal of the Electrochemical Society*, 158 (2011) R1-R25.
- [7] T.M. Bandhauer, S. Garimella, T.F. Fuller, Temperature-dependent electrochemical heat generation in a commercial lithium-ion battery, *Journal of Power Sources*, 247 (2014) 618-628.
- [8] T. Stuart, F. Fang, X. Wang, C. Ashtiani, A. Pesaran, A modular battery management system for HEVs, *SAE Technical Paper*, 2002.
- [9] Y. Chen, J.W. Evans, Heat Transfer Phenomena in Lithium/Polymer-Electrolyte Batteries for Electric Vehicle Application, *Journal of the Electrochemical Society*, 140 (1993) 1833-1838.
- [10] G.G. Botte, V.R. Subramanian, R.E. White, Mathematical modeling of secondary lithium batteries, *Electrochimica Acta*, 45 (2000) 2595-2609.
- [11] K. Kumaresan, G. Sikha, R.E. White, Thermal model for a Li-ion cell, *Journal of the Electrochemical Society*, 155 (2008) A164-A171.
- [12] G.-H. Kim, A. Pesaran, R. Spotnitz, A three-dimensional thermal abuse model for lithium-ion cells, *Journal of Power Sources*, 170 (2007) 476-489.
- [13] L. Saw, Y. Ye, A. Tay, Electrochemical–thermal analysis of 18650 lithium iron phosphate cell, *Energy conversion and management*, 75 (2013) 162-174.



- [14] N. Sato, Thermal behavior analysis of lithium-ion batteries for electric and hybrid vehicles, *Journal of power sources*, 99 (2001) 70-77.
- [15] H.-K. Kim, T.-Y. Seong, J.-H. Lim, W.I. Cho, Y.S. Yoon, Electrochemical and structural properties of radio frequency sputtered cobalt oxide electrodes for thin-film supercapacitors, *Journal of power sources*, 102 (2001) 167-171.
- [16] A. Bernardes, D.C.R. Espinosa, J.S. Tenório, Recycling of batteries: a review of current processes and technologies, *Journal of Power Sources*, 130 (2004) 291-298.
- [17] J. Chen, C. Yao, S. Sheu, Y. Chiou, H. Shih, The study of carbon half-cell voltage in lithium-ion secondary batteries, *Journal of power sources*, 68 (1997) 242-244.
- [18] V. Srinivasan, J. Newman, Discharge model for the lithium iron-phosphate electrode, *Journal of the Electrochemical Society*, 151 (2004) A1517-A1529.
- [19] L. Rao, J. Newman, Heat-generation rate and general energy balance for insertion battery systems, *Journal of the Electrochemical Society*, 144 (1997) 2697-2704.
- [20] S. Zhang, K. Xu, T. Jow, The low temperature performance of Li-ion batteries, *Journal of Power Sources*, 115 (2003) 137-140.
- [21] C.-K. Park, Z. Zhang, Z. Xu, A. Kakirde, K. Kang, C. Chai, G. Au, L. Cristo, Variables study for the fast charging lithium ion batteries, *Journal of power sources*, 165 (2007) 892-896.

# CHAPTER 2

## COMSOL OVERVIEW

### 2.1 Introduction

The **COMSOL Multiphysics 5.2a** has been used to solve the equations using the Finite Elements Method (FEM). The screenshot reported in Figure 2.1 is what you will see when you first start modeling in COMSOL Multiphysics using the **Model Builder**. The COMSOL Desktop® user interface provides a complete and integrated environment for physics modeling and simulation as well as application design, providing with the tools necessary to build a user-friendly interface for the models.

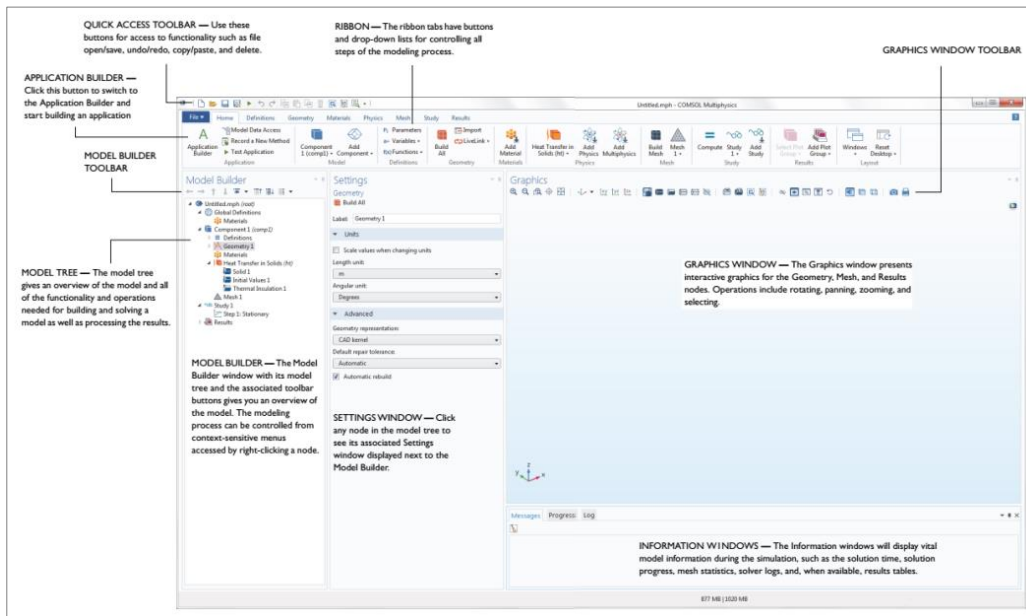



Figure 2.1. Screenshot from COMSOL desktop.

## 2.2 Materials

The **Materials** (  ) node under Global Definitions stores the material properties for all physics and all domains in a Component node. Any material involves many physical properties including values or functions (for temperature-dependent material properties, for example) to explain the material. The material properties were organized in material property groups, which appear as sub-nodes under the **Material** node in the **Model Builder**. The material library and the setting windows have been represented in Figure 2.2.

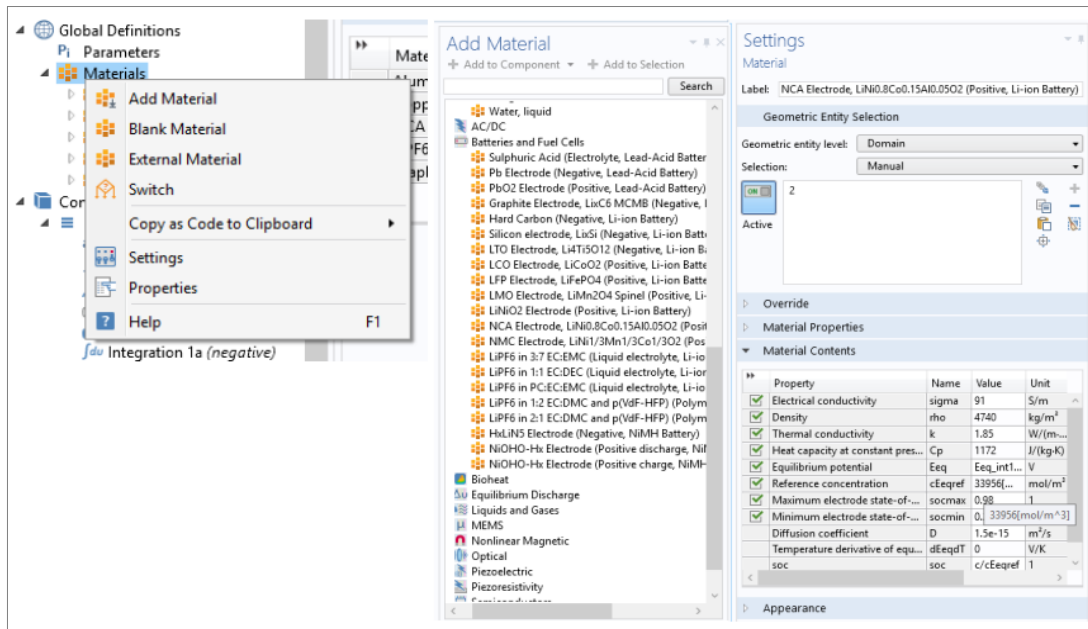


Figure 2.2. Add material, the batteries & fuel cells material library, and settings windows.


The materials were accessible from **the Batteries and Fuel Cells Material Library**, and mostly default settings have been selected. The Lithium-Ion Battery connecting accounts for:

- Electronic conduction in the electrodes.

- Ionic charge transport in the electrodes and electrolyte/separator.
- Material transport in the electrolyte, providing the foundation of the impacts of concentration on ionic conductivity and concentration overpotential.
- Material transport inside the spherical particles that form the electrodes.
- Butler-Volmer electrode kinetics using experimentally measured discharge curves for the equilibrium potential.

For the SOCs of the electrodes, both “Coulomb” and “at load” were defined in the **Lithium-Ion Battery** interface. The “Coulomb” in contrast to “at load” omits the impact of any polarization in the battery. An **Event** interface has also been used to restrict the operation of the battery within the upper and lower cut-off voltages.

### *2.3 The Geometry Node*

To define and create the geometry sequence a **Geometry** node (  ) utilized for the model component. The Geometry node also contains some general settings for the geometry such as the length and angular units as illustrated in Figure 2.3.

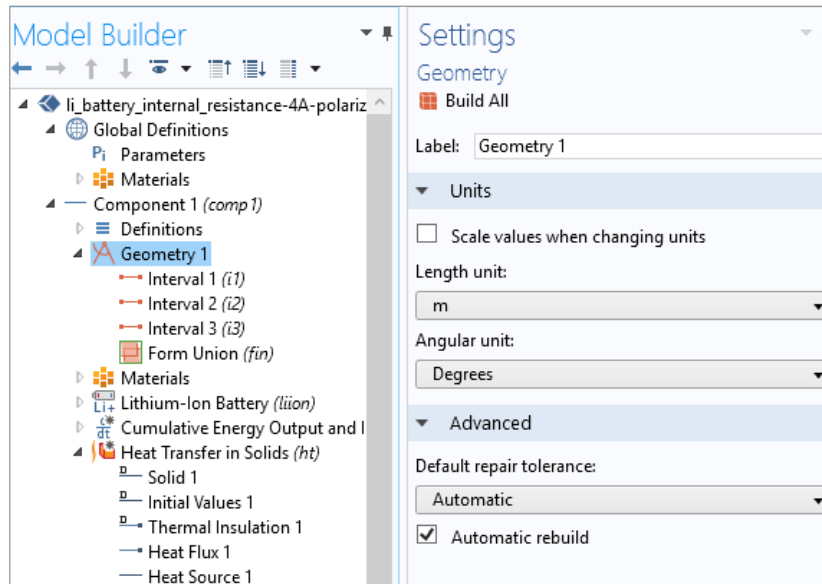




Figure 2.3. The geometry setting view.

## 2.4 The Lithium-ion battery interface

The **Lithium-Ion Battery (Li-Ion)** interface (  ), situated under the **Electrochemistry>Battery Interfaces branch** (  ) when adding a physics interface to compute the potential and current distributions in a lithium-ion battery. Multiple intercalating electrode materials can be used, and voltage losses due to solid-electrolyte-interface (SEI) layers are also included. The physics interface was based on the works of Newman et. al. Ohm's law was used to describe the charge transport in the electrodes, whereas concentrated electrolyte theory for a quiescent aprotic (1:2) electrolyte has been used to describe charge and mass transport in the electrolyte phase. An extra dimension was included in the porous electrode domains to describe the transport of solid lithium in the solid electrode phase using

Fick's law. Figure 2.4 shows the Lithium-ion battery node interface. Using the Initial Cell Charge Distribution global node can define the initial cell voltage or cell state-of-charge (SOC) of a battery cell. When used together with a Current Distribution Initialization study step, the node will solve for the intercalated concentrations in the Porous Electrode nodes to comply with the given initial conditions. The node also offers the possibility to balance the electrodes by calculating the electrode phase volume fractions. The node only has an effect on the original equations solved for when used in a Current Distribution Initialization study step. SOC and porosity variables will be defined for all research levels.

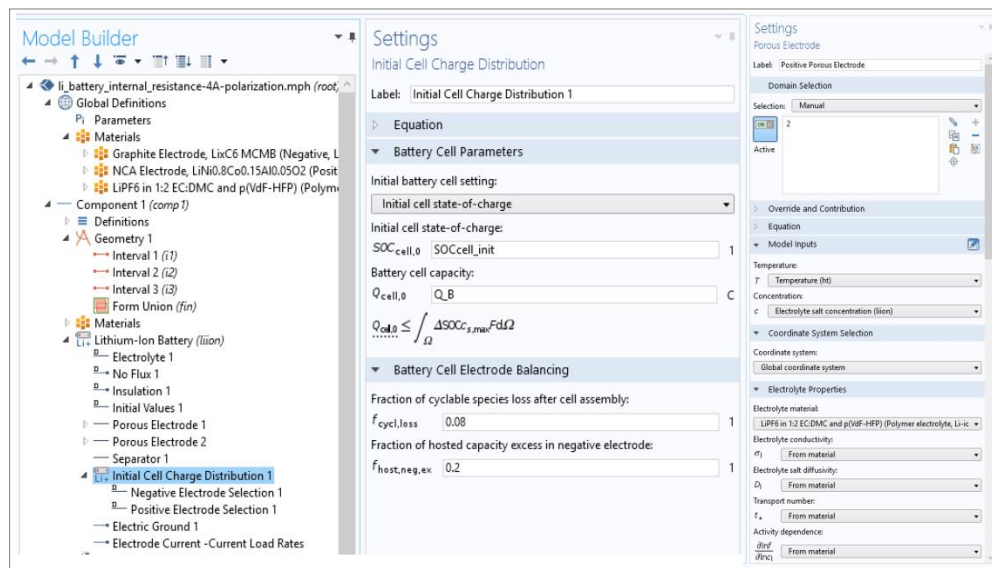


Figure 2.4. The Lithium-ion battery node interface.

## 2.5 The ODE and DAE Interfaces

The **Global ODEs and DAEs** (ordinary differential equations and differential-algebraic equation) interface ( $\frac{d}{dt}$ ), located under the Mathematics branch ( $\Delta u$ ) when adding

a physics interface, was used to add global space-independent equations that can represent additional states.

The **Global ODEs and DAEs** interface have a **Global Equations** node that is designed for implementing this type of external equation. Such equations are often tightly coupled to a model in a physical domain. The Global Equations node is also available for any of the physics interfaces as shown in Figure 2.5.

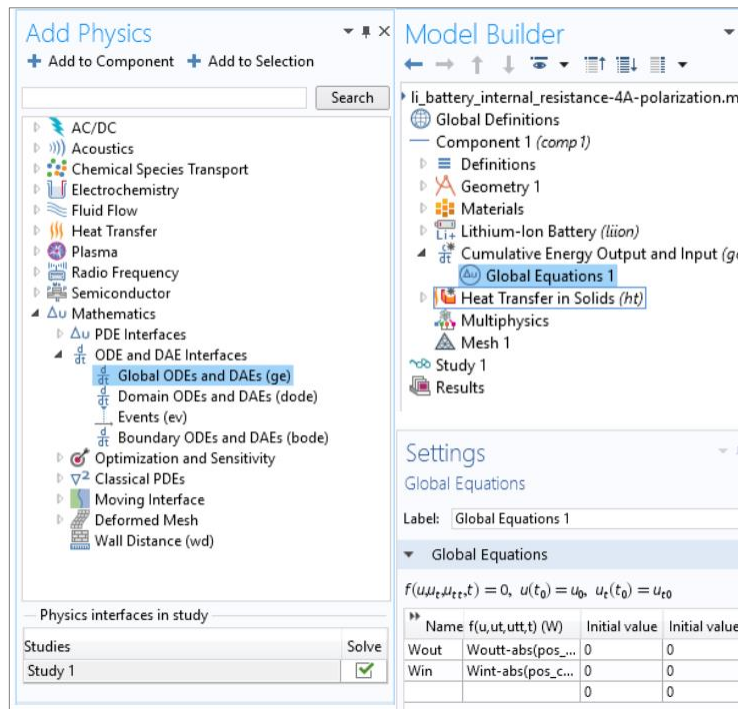


Figure 2.5. The ODE and DAE Interfaces windows.

## 2.6 The Heat Transfer in Solids Interface

The **Heat Transfer in Solids** (🔥) interface has been used to model heat transfer in solids by conduction, convection, and radiation. A Solid model is active by default on all domains. All functionality for including other domain types, such as a fluid domain, is also available as presented in Figure 2.6.

The temperature equation defined in solid domains corresponds to the differential form of the Fourier's law that may contain additional contributions like heat sources. When this version of the physics interface was added, these default nodes were added to the **Model Builder: Solid, Thermal Insulation** (the default boundary condition), and **Initial Values**. Then, from the **Physics toolbar**, add other nodes that implement, for example, boundary conditions and sources. To select physics features from the context menu can also right-click **Heat Transfer in Solids**.

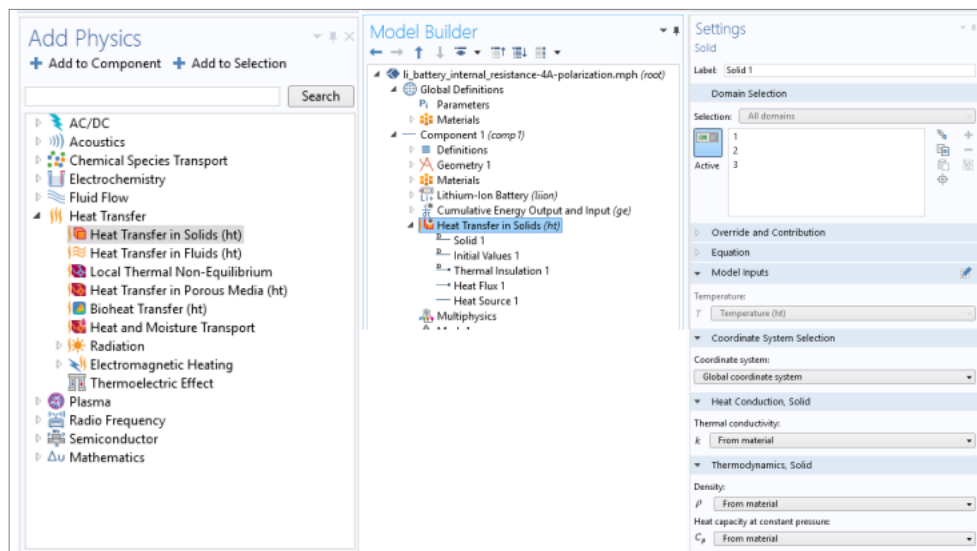


Figure 2.6. The Heat Transfer in Solids Interface.



## 2.7 Meshing

Through adding a new Component to the Model Builder, a meshing sequence is added by default in a **Mesh node** (▲). It is possible to add more meshing sequences to the Component by right-clicking the **Component** node and selecting **Mesh**. When a Component has more than one meshing sequence, they are collected under a **Meshes** node as shown in Figure 2.7. A mesh can be created by building a meshing sequence, which contains some meshing operations as nodes in the sequence. For the default physics-controlled meshes, the software sets up the meshing sequences automatically. Due to high nonlinearity of the governing equations, the performance and accuracy of the calculation strongly depend on the mesh and solver. A free quadrilateral mesh was used at the boundaries along with the swept method, and several mesh densities were tested to ensure the mesh independency of the solutions of this research model.

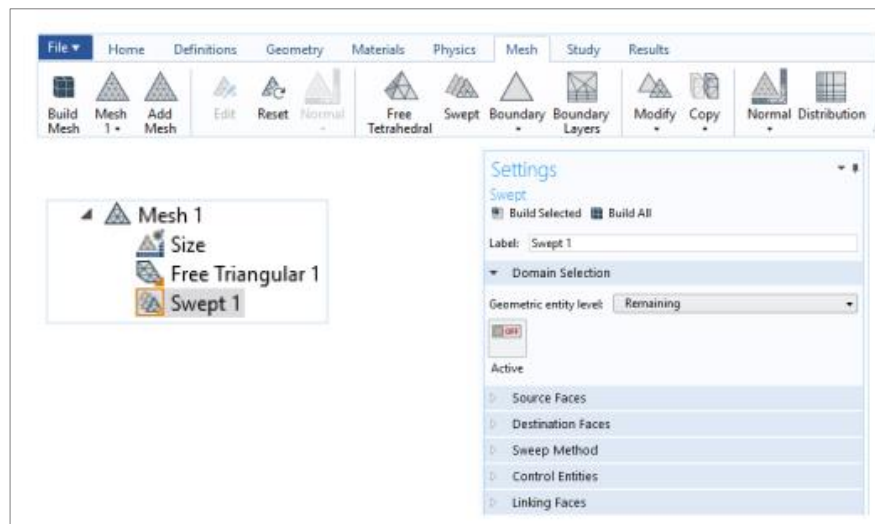




Figure 2.7. Adding, Editing, and Building Meshing Sequences.

## 2.8 Study

A **Study** node () holds all the nodes that define how to solve a model. These nodes are divided into three broad categories:

- Study steps, which determine overall settings suitable for a particular study type. The study steps added are based on the chosen study types.
- Solver Configurations, which contain the solvers and related configurations for dependent variables to solve for, intermediate storage of solutions, and specific solver settings.
- Job Configurations, which provide all jobs defined for a study (distributed parametric jobs, batch jobs, and cluster computing).

A **Parametric Sweep** () study has been used as illustrated in Figure 2.8 to find the solution to a sequence of stationary or time-dependent problems that arise when you vary some parameters of interest. The parametric sweep can include multiple independent parameters directly for a full multi-parameter sweep (solve for the first value of the first parameter combined with all values of the second parameter. Then the second value of the first parameter combined with all values of the second parameter, and so on, or could use a specified combination of parameter values). Also, could add more than one Parametric Sweep node to create nested parametric sweeps. The program then treats the parametric sweeps as a “nested for-loop” and indicates the nested structure using indentations of the Parametric Sweep nodes’ names. To save the memory and time, the equations coupled by utilizing the segregated approach. For each time step, the maximum relative tolerance for all variables has been considered 0.001. The process repeated at each node till generating the convergence plot. The

computations executed on a workstation of 64-bit Intel® Xeon® Processor 3.40E GHz including 32GB random access memory.

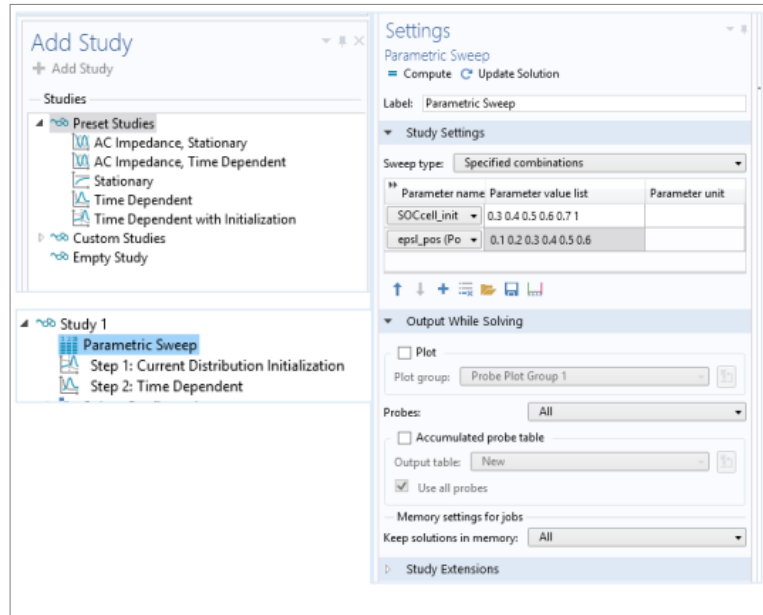


Figure 2.8. Study configuration.

## 2.9 References

- [1] Introduction to COMSOL Multiphysics 5.2a, © 1998–2016 COMSOL

## **CHAPTER 3**

### **HEAT RESPONSE OF PRISMATIC LI-ION CELLS**

*This work was presented and published in IEEE Transportation Electrification Conference and Expo (ITEC), 2014 IEEE, US, 24 July 2014.*

---

#### ***3.1 Summary***

The experimental studies of the charge-discharge behavior and heat generation rate of lithium ion cells at different C-rates are conducted in this paper. We are extending this process to monitor and control the thermal behavior of Li-ion batteries by using phase change material (PCM) as a passive thermal management method to absorb and conduct heat to and from lithium-ion battery modules.

#### ***3.2 Introduction***

Electrification of vehicles may have a significant role in reducing consumption of fossil fuels by up to 75% [1] and change the nature of automobile market. The performance of electric vehicles strongly depends on the fulfillment of the battery pack. In general, temperature affects several aspects of a battery performance including the operation of the electrochemical reactions inside a battery, rates of charging and discharging, energy density and power capability, cycle life and shelf life, battery safety and reliability, and battery cycle cost. The main concerns of the consumers are to an extent the service life, safety, and reliability of the

battery on board of an electric vehicle. It is noteworthy to mention that in addition to the battery chemistry, these concerns are strongly depended on the quality and efficiency of battery management system. A lithium-ion battery is a compact energy storage device containing high energy materials and may undergo thermal runaway and explode if overcharged, due to the decomposition of cell components (electrolyte and electrodes) that generate flammable and toxic gaseous species [2]. Also, heating the battery outside a normal range (10-45 °C) may accelerate the battery aging and severe capacity fading during charge-discharge cycles. In a consumer market, only a few accidents due to battery problem may derail the research and development efforts on hybrid and electric vehicle systems.

In this research effort, we address the thermal behavior of the lithium battery and predict the possibility of using only phase change materials as a passive thermal control for the entire battery pack. Further, this work may provide a guideline for the development of next generation of PCM formulation capable of managing different hybrid and electric vehicles. This work also may result in generating the specification of different PCM for batteries with the different form factor and different power to energy ratios of the various electric-based vehicles, such as mild hybrid, extended range plug-in hybrid, and fully electric vehicles.

The phase change materials are capable of absorbing/transferring heat from/into the battery pack and maintaining an optimal temperature for efficient operation of battery cells. The majority of current phase change materials are dealing with solid $\leftrightarrow$ liquid phase transformation. However, other combinations such as solid $\leftrightarrow$ solid in the combination of various solid $\leftrightarrow$ liquid formulations and the combination of multiple of PCMs are the subjects of next generation of PCM technology. The second phase of our research work guided with

simulation may provide a framework for the new formulation of PCM systems. The use of such a passive thermal control may significantly reduce the overall cost of the battery pack for electrified transportation.

Phase change composite material can be used to decrease cell-to-cell temperature uniformity for various driving cycles. The addition of current PCM material may add a significant thermal resistance barrier between the cell surfaces that prevent heat transfer from cell-to-cell [3]. However, the heat transfer from inside to outside the battery pack also may be reduced. In our future design, we will create PCM with a different formulation to serve as the thermal barrier and facilitate the heat rejection to the exterior of the battery for waste heat rejection.

While the thermal management of Li-ion batteries is essential to improve battery performance [4], it may significantly widen the safety margin of electrified vehicles.

### ***3.3 Geometry and operating conditions***

To investigation and design of a thermal management system for any battery thermal modeling is a vital tool. A Combination of thermal modeling and electrochemical modeling of the cell yield a complete analysis, capable predict the thermal and electrochemical effects of the cell. Newman and coworkers were started the first modeling of lithium-ion batteries [5,6].

Usually, the prismatic cells contain a jelly roll or a pile of electrodes as shown in Figure 3.1. They are with a rugged mechanical and high packing efficiency.

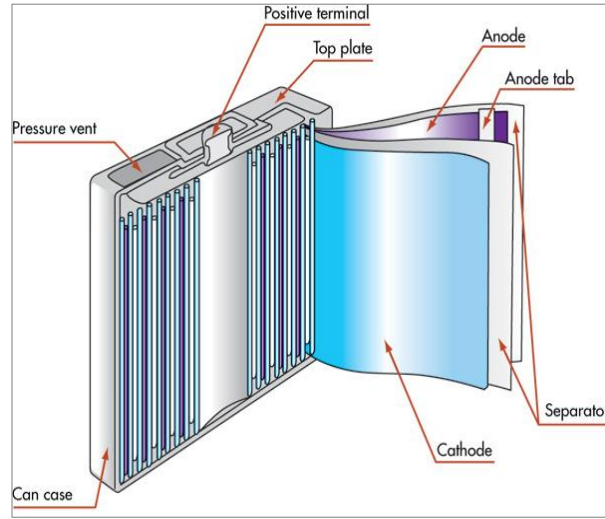
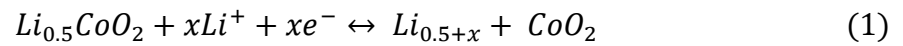


Figure 3.1. Multi-folded-layer structure of a prismatic cell [7].

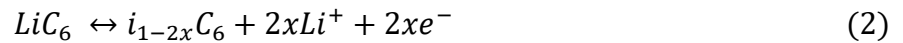
The 1,800 mAh prismatic Li-ion battery (GMB 654765) considered in this study. The common cathode/anode materials of a Li-ion battery are  $\text{LiCoO}_2/\text{C}$ . Table 3.1 presented the geometry details and properties of the GMB 654765.

The electrochemical reactions during the charge/discharge can be expressed as,

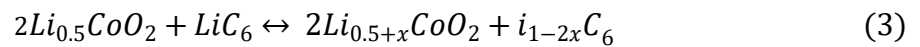
At positive electrode:



At negative electrode:



Overall reaction:



where through the discharge cycle the reversible reaction move from left to right and during the charge cycle the reverse reaction takes place [8].

The generated heat caused by entropy change can be defined from [9],

$$\dot{q}_{entropy} = -iT \frac{\partial V^0}{\partial T} = -T\Delta S \frac{i}{nF} \quad (4)$$

$$\Delta S = -\frac{\partial \Delta G}{\partial T} = -nF \frac{\partial V^0}{\partial T} \quad (5)$$

where the Gibbs energy change is:

$$\Delta G = -nFV^0 \quad (6)$$

According to the process of (3) during the charge/discharge means the battery generates heat that can be described as Equation (7) affected by the current flow across the cell [9].

$$\dot{q} = i(V^0 - V - T \frac{\partial V^0}{\partial T}) \quad (7)$$

By considering the battery as a unit, the rate of energy change equation would be in the following form:

$$mC_p \frac{\partial T}{\partial t} = \dot{q} - hA(T - T_a) \quad (8)$$

where  $m = \rho V$  is the battery mass,  $C_p$  is the battery heat capacity,  $h$  is the convection heat transfer coefficient that allows combining the effect of different cooling rates at different stages of heat treatment,  $A$  is the battery surface area and  $T_a$  is the ambient temperature. By substituting Equation (7) into Equation (8) the rate of energy change equation is:



$$mC_p \frac{\partial T}{\partial t} = i(V^0 - V - T \frac{\partial V^0}{\partial T}) - hA(T - T_a) \quad (9)$$

### 3.4 Experimental setup and results

We test 1,800 mAh prismatic Li-ion cells using commercial battery cycler (MACCOR) at different C-rates. These batteries will be utilized as the building block for construction of module and packs in our initial simulation models.

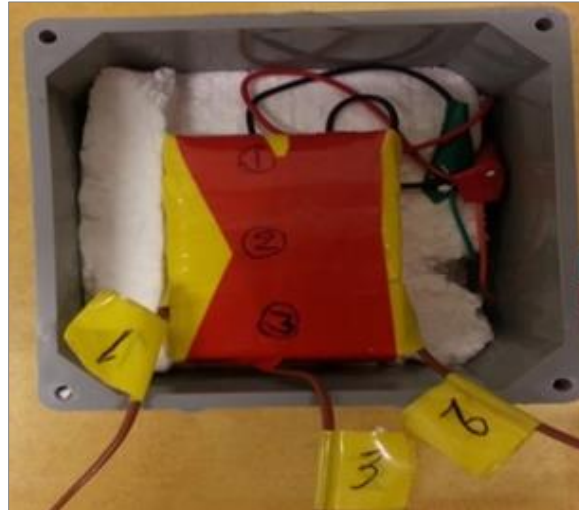


Figure 3.2. Two parallel Li-ion cells (GMB 654765).

We have tested two classes of flat prismatic lithium-ion cells at C/4, C/2, and C-rates for a single cell and battery containing two parallel cells. Also, the tests were performed at various temperatures for different C-rate. To measure and record the temperature behavior of the battery pack with two parallel cells several T-type thermocouples have been attached to the

various sections of the battery pack (#1 close to the tab, #2 in the center, #3 close to the bottom of the cell) as shown in Figure 3.2.

Table 3.1. Physical properties of materials [9].

	Thickness ( $\mu\text{m}$ )	Height (mm)	Density ( $\text{k.g.m}^{-3}$ )	Thermal conductivity $\text{W.(m K)}^{-1}$	Specific heat $\text{J.(kg K)}^{-1}$	Electrical conductivity ( $\times 10^6, \text{S.m}^{-1}$ )
<b><i>LiCoO<sub>2</sub></i></b>	92	53	2291.62	1.85	1.1728	0.0001
<b><i>LiC<sub>6</sub></i></b>	87	53	5031.67	5	0.7	0.0001
<b><i>Al</i></b>	10	55	2700	200	0.87	38
<b><i>Co</i></b>	10	57	9000	380	0.381	60
<b><i>Separator</i></b>	22	59	1200	1 0.7	1.0	–

Figure 3.3 shows the typical charge-discharge voltage profile for a battery pack at  $I=0.9$  Ah between 2.5-4.7 V.

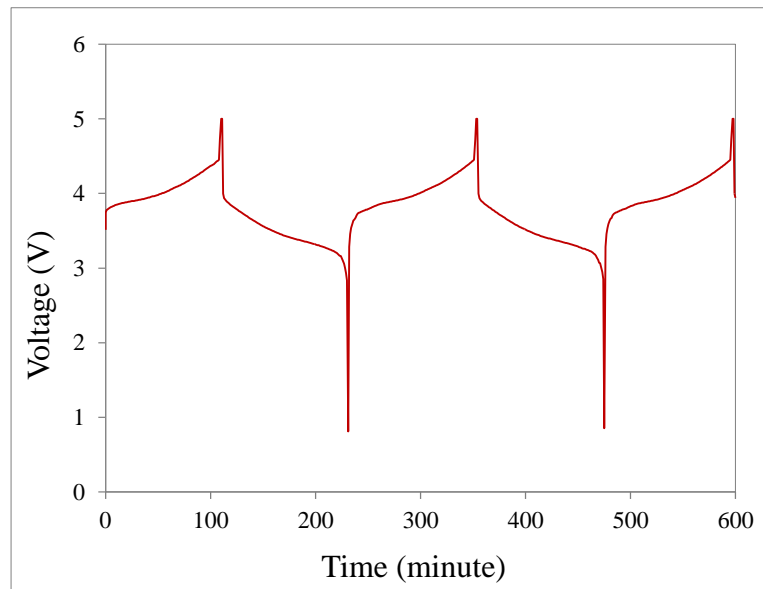


Figure 3.3. Charge and discharge voltage profile for two parallel cells (C/2-rate).

Figure 3.4 indicates the sensitivity of the setup even at this low rate ( $C/2$ ) and modulation of temperature in the cell.

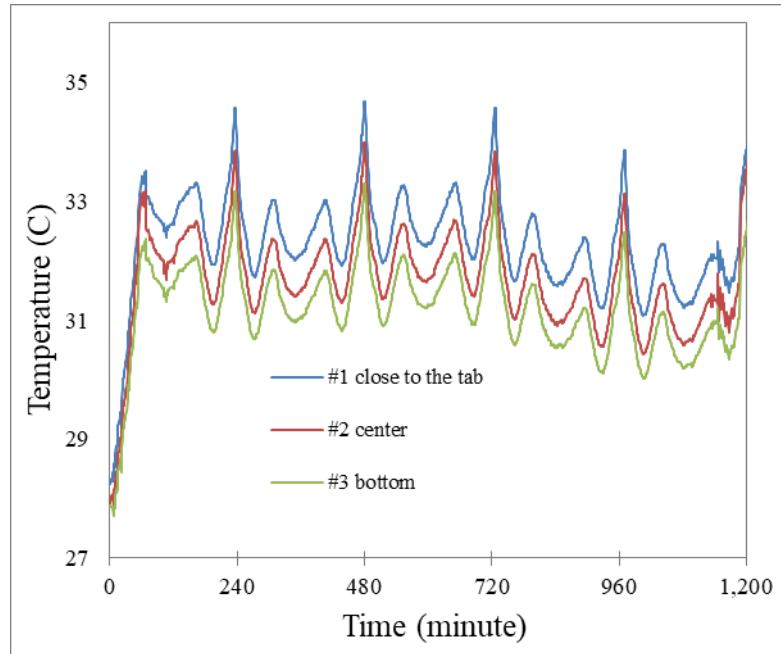


Figure 3.4. Temperature behavior of the battery pack with two parallel cells ( $C/2$  rate), graphs indicate thermal response of thermocouple at 1) close to the tab, 2) at the center, and 3) at the bottom of the cell.

The heat generation close to the tab is higher than the temperature from other sections of the cell as expected. This well-understood phenomenon is a great test for our set-up for future work, higher rates, and higher Ah cells. Figure 3.5 shows the thermal behavior of a single cell at a  $C/2$  rate of a charge and discharge cycle. This preliminary test has shown the heat generation inside the single cell, illustrated in Figure 3.6.

At this stage, we are confident on the performance and monitoring of the hardware for testing cells. A much higher resolution is expected when cells are being tested at higher rates, particularly for larger Ah cells.

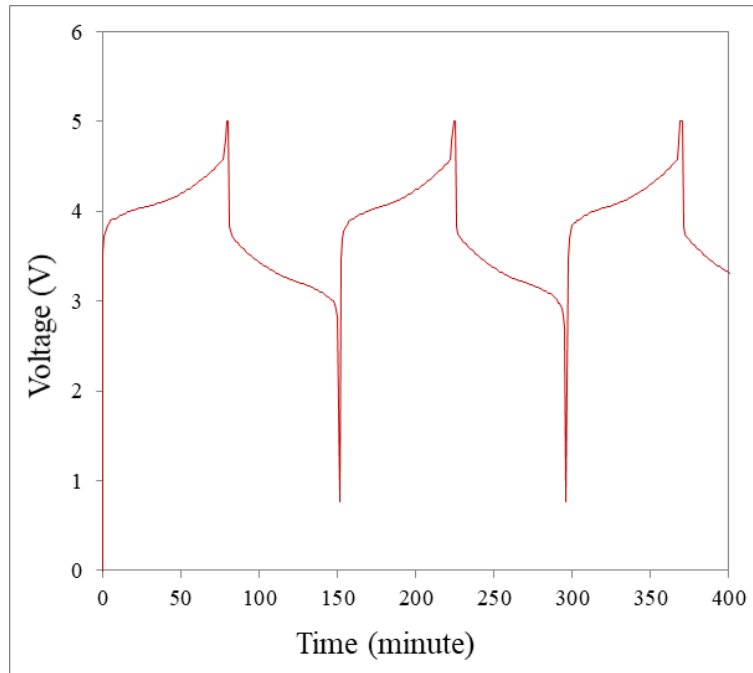


Figure 3.5. Charge and discharge voltage profile of a single cell (C/2-rate) during first three charge and discharge cycles.

Figure 3.6 illustrated a single cell at C-rate during charge the temperature rise close to the tab was 7 °C, and during the discharge, the maximum temperature rise was 12 °C. The heat dissipation in this condition is only by natural air convection via the spaces between the cells and the battery container. The temperature rise at the center and close to the bottom of the cell during charge/discharge respectively was around 6 °C, 7.5 °C, and 3 °C, 4 °C. The maximum temperature was found above the center of the battery in this package.

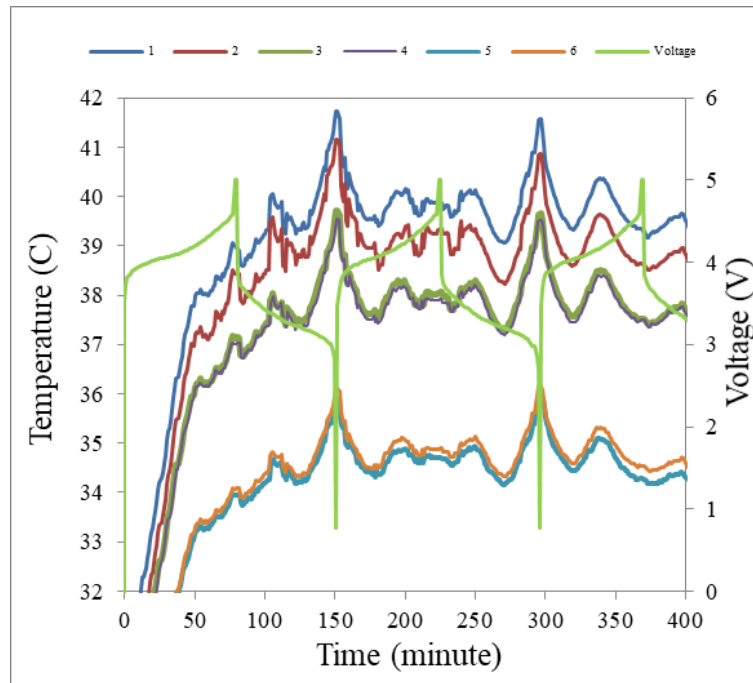


Figure 3.6. Temperature & voltage behavior of a single cell vs Time at C-rate.

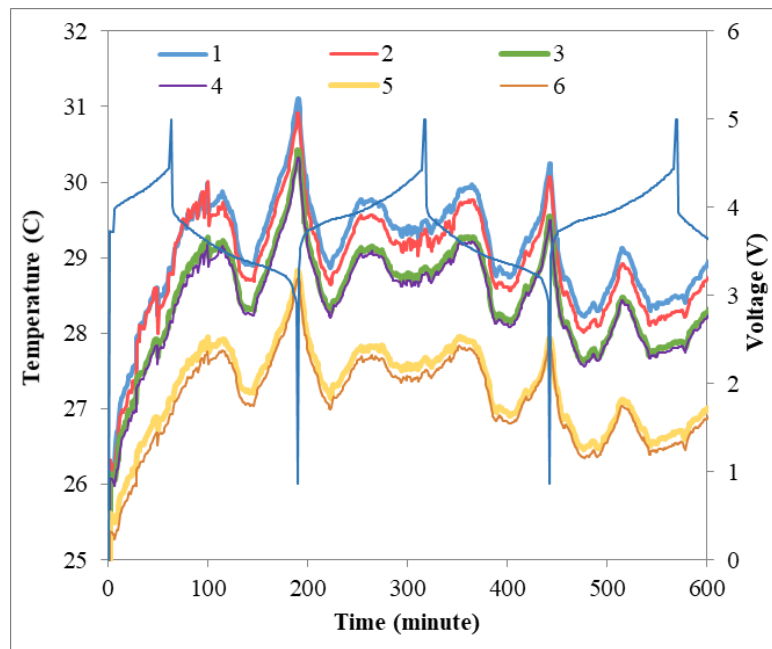


Figure 3.7. Temperature & Voltage vs Time at C/2 rate for a single cells.

Figure 3.7 presented the temperature behavior of a single cell at the C/2 rate. During the discharge time, the heat rise close to the tab of the cell was 6 °C, at the center 5.5 °C and close to the bottom it was around 4 °C.

Concerning Figure 3.8 the temperature rise at C-rate is more significant compared to C/2 and C/4 rates. Therefore, the higher current magnitudes contribute to higher the Joule heating.

### **3.5 Conclusion**

The thermal behavior of prismatic Li-ion batteries during charge/discharge cycles was experimentally investigated. Firstly, a module consists of two parallel cells at C and C/2 rates was examined. The temperature rises during the charge and discharge cycles were measured to be roughly 6 °C and 7 °C, respectively. The results indicated that accumulation of the temperature in regions close to the tab is higher than that in the center and close to the bottom of the module. Therefore, uniform temperature module, which is widely used in the literature, is not a realistic assumption. The thermal response of a single cell at C, C/2 and C/4 rates is considered in the second step. The results revealed that the highest temperature occurs at C-rate. The maximum temperature increment in the charge cycle was an about 7 °C while; it was 12 °C during the discharge cycle. The experimental data reported in the present study can be utilized for designing high-performance thermal management systems for Li-ion battery modules.

### 3.6 Reference

- [1] D. Claus, "Materials and processing for lithium-ion batteries," *J. of Miner. Metals Mater. Soc.*, vol. 60, pp. 43–48, 2008.
- [2] T. Stuart, F. Fang, X. P. Wang, C. Ashtiani, and A. Pesaran, "A modular battery management system for HEVs," *Future Car Congress*, doi: 10.4271/2002-01-1918, 2002.
- [3] T. M. Bandhauer, *Electrochemical-Thermal Modeling and Microscale Phase Change for Passive Internal Thermal Management of Lithium Ion Batteries*, A dissertation presented to the academic faculty, Georgia Institute of Technology, USA, December 2011.
- [4] S. Al-Hallaj, R. Kizilel, A. Lateef, R. Sabbah, M. Farid, and J. R. Selman, "Passive Thermal Management Using Phase Change Material (PCM) for EV and HEV Li-ion Batteries", 7-9 Sept. 2005, Print ISBN:0-7803-9280-9.
- [5] Doyle, Marc, Fuller, Thomas, Newman, John, "Modeling of galvanostatic charge and discharge of the lithium/ polymer/insertion cell", *J. Electrochem. Soc.*, 140 (6) (1993), pp. 1526–1533.
- [6] L. Rao, J. Newman," Heat-generation rate and general energy balance for insertion battery systems", Volume 144, Issue 8, August 1997, Pages 2697-2704.
- [7] Kim Yeow, Ho Teng, Marina Thelliez," Eugene Tan3D Thermal Analysis of Li-ion Battery Cells with Various Geometries and Cooling Conditions Using Abaqus", 2012 SIMULIA Community Conference.
- [8] Williford R, Viswanathan V, Zhang J-G. Effects of entropy changes in anodes and cathodes on the thermal behavior of lithium-ion batteries. *J Power Sources* 2009;189:101–7.
- [9] Dong Hyup Jeon , Seung Man Baek," Thermal modeling of cylindrical lithium ion battery during discharge cycle", *Energy Conversion and Management* 52 (2011) 2973–2981.

## CHAPTER 4

# ELECTROCHEMICAL–THERMAL MODEL OF POUCH-TYPE LITHIUM-ION BATTERIES

*This work has been published in Electrochemical–Thermal Behavior of a Prismatic Lithium-Ion Battery, MRS conference 2016 and Electrochimica Acta - Journal – Elsevier, 2017*

---

### 4.1 Summary

In this paper, a 3D (three-dimensional) layer structure of a pouch-type cell is modeled to understand the distribution of temperature and current density across the pouch type Lithium-Ion Battery (LIB). The electrochemical-thermal characteristics are studied, using 1D (one-dimensional) multiphysics model, and simulation results are validated with experimental results. Three-dimensional (3D) modeling of the battery gives the most efficient estimation of energy density, temperature response, overall heat generation and distribution inside the battery. One such 3D electro-thermal model was developed in this work, and the results obtained by the 3D model were validated by using experimental results obtained from LIBs. Temperature profiles of LIB obtained from 3D modeling indicated that the most heat is accumulated around the positive tab of the battery due to non-uniform current distribution and local internal resistance. The presented model can be used as a fast, yet accurate tool, to optimize the cell design for a particular application and for developing battery thermal management systems.



## **4.2 Introduction**

Electrification of vehicles may have a significant role in reducing consumption of gasoline to one-fourth of today's use. Lithium-ion batteries can provide a credible rechargeable storage technology for the electrification of the drivetrain and to provide permanent storage solutions to facilitate the efficiency of renewable energy sources [25].

Among the available battery technologies, LIB is expected to be the energy storage of choice for EVs and hybrid electric vehicles (HEVs) due to their high energy density and long lifecycle. On the other hand, LIB contains high energy materials and due to the decomposition of battery components, particularly that of the cathode and electrolytes, and increased reactivity of the anode when fully lithiated, may undergo thermal runaway if overcharged. These decomposition reactions may result in inflammable and toxic gasses [11]. Also, heating the battery outside a normal range (10-45 °C) may limit the energy and power of the battery, and accelerate the battery aging causing severe loss of capacity during charge-discharge cycles. While the thermal management of LIB is essential to improve battery performance [26], it may and significantly extend the safety margin of hybrid and electric vehicles.

In general, the temperature has a significant impact on the chemical and electrochemical reactions inside a battery, charging and discharging rates, energy density and power capabilities, safety and reliability, and cycle lifetime of lithium-ion batteries.

It is crucial to extend the service life, safety, and reliability of the battery on board of an electric vehicle, particularly when large size batteries are used. In addition to the battery

chemistry, these concerns are strongly dependent on the quality and efficiency of BMS that controls the battery voltage, current and temperature domains used during battery operation.

To predict the electrochemical process taking place within the LIB during charging and discharging operation, various thermal models have been proposed to explain the heat generation in the battery [13-17, 21, 27-35].

The size of the battery affects the amount of heat generated during charge and discharge processes. The cell temperature is also affected by the number and thickness of the electrode layers. Controlling the amount of heat generated is extremely important for high power devices, such as electric vehicle batteries, where excessive heat can cause damage and reduces battery's lifetime. One method to manage the battery temperature is to optimize the cell format and reduce the overall resistance of the layers in the battery. In this research, we studied the electrochemical-thermal (ECT) behavior of pouch type LIB, particularly for high energy cells. Two modeling techniques were used to estimate the ECT response. The first method, namely 1D modeling was used to understand the ECT reactions and to identify the source of heat generation inside the battery. The ECT is carried out using similar approaches used by well-known J. Newman method [22, 36, 37]. In Newman method, heat dissipation flux depends on the temperature difference between the initial state and the surface temperature, as well as on the heat transfer coefficients of the battery components. This method is the basis of most of the work presented in the literature.

For example in [32], charge balance equation has been used to estimate voltage response of the LIB during the galvanostatic discharge process. It was confirmed that ohmic heating in

electrodes contributes to only up to 18% of the total heat generation. In [30], distribution of potential and current in planar electrodes of pouch type LIB, as well as the discharge process, have been studied using Newman's energy balance equation in conjugation with polarization expression. It was observed that the reaction current remains uniform even when a depth of discharge (DOD) varies from 5% to 85%.

Most of the past studies are focused on the lithium iron phosphate cell ( $\text{LiFePO}_4$ ) [16, 21, 33], lithium manganese oxide ( $\text{LiMn}_2\text{O}_4$ ) [13, 27, 34, 35] or Lithium cobalt oxide ( $\text{LiCoO}_2$ ) [14, 15, 17, 18]. The discharge model for the lithium iron – phosphate electrode, has shown that the power capability of the cells is limited by the ohmic drops in the matrix phase, contact resistances between the current collector and the porous matrix, and transport limitations in the iron phosphate particles [14].

Lithium cobalt oxide is used in primary Sony cells to demonstrate the capability of layered oxide as potential intercalation cathode for lithium-ion cells. However, due to the high cost of lithium cobalt oxide, the layered nickel oxide based cathode has been introduced. However, due to the instability of  $\text{Ni}^{4+}$  that is formed during charging of the cell ( $\text{Ni}^{3+} \rightarrow \text{Ni}^{4+} + e^-$ ), some of the nickel ions migrate to the lithium sites between the metal oxide slabs that causes structural transformation and release of oxygen. This problem has been mitigated to some extent by keeping some of the cobalt ions that lead the formation of the layer structure, and an addition of aluminum that maintains strong Al-O bonding. Therefore the structural integrity of the substituted cathode is enhanced as compared to the pure lithium nickel oxide system, and the so-called NCA is used in many commercial cells.

Very few 3D thermal modeling studies have been carried out to investigate the operation of NCA electrode in LIB. Therefore, this work is focused on ECT behavior of the pouch LiNiCoAlO<sub>2</sub>/polymer LIBs.

Different multi-dimensional electrochemical and thermal coupled models are developed by many researchers to simulate ECT behavior of LIB. Knowledge of ECT coupling is essential for prediction of LIB characteristics [17].

Basu et al, [38] investigated a three-dimensional electrochemical, thermal model to determine the internal temperature distribution of the battery. Unfortunately, the electrochemistry of battery was not considered in this model. To effectively predict and design the ECT performance of the large-sized battery, the electrochemical reaction of the cell should be studied as a heat generation source. Guo and White [39] proposed a linear approximation method to decouple the electrochemical model from the heat equation. Since the proposed method was based on observations from one single electrode, the model inherently has low accuracy.

In this paper, 1D modeling provides an illustration of heat generation, the electric potential, total charge/discharge current, voltage loss, electrolyte phase concentration, local current density, and electrode particle lithium concentration. However, the 1D model cannot explain how heat is distributed inside the battery. A 3D model is required to understand heat and current distribution inside the battery. Moreover, to study the relationship between the cell unit and the battery, many studies have been carried out on single cell unit as one-dimensional (1D) electrochemical models and coupled with the three-dimensional (3D) thermal

models [9,25]. Electrochemical 3D battery model coupled with a 3D thermal model is the only possible method to estimate the effect of the electrical contact resistance between the cell multilayers, current collectors, and the tabs. The 3-D model also provides insight into the geometrical dimensions of the current collecting tabs and the heat dissipation on the battery surface. The 3D model proposed in this paper is an extension of the proposed 1D ECT model on multiple electrode plate pairs. The combination of thermal and electrochemical modeling used in this work provides a qualified analysis for predicting the thermal and electrochemical behavior of the cell. The proposed model's predictions are also validated by comparing them with experimental data.

It is vital to evaluate the model for the scale of heat generation and heat transfer inside the electrochemical cell to predict the thermal response of Li-ion batteries.

In this work, the results of 3D electro-thermal modeling have been validated using physical experiments carried out on LIBs. Temperature profiles of LIB obtained from 3D modeling illustrated that most heat is accumulated around the positive tab of the battery due to uneven distribution of current density and local internal resistance [40].

### ***4.3 Experimental Study***

#### ***4.3.1 Experimental setup***

In this study, all the experimental tests are performed on commercially available lithium-ion batteries (LiNiCoAlO<sub>2</sub>)/Graphite. In these experiments, pouch-type Li-ion PL7872196

battery, fabricated by Tenergy Corporation have been used. The battery has a capacity of 10 Ah. Other relevant parameters of the battery are provided in Tables 4.1-2.

Figure 4.1 displays the geometry of the pouch-type lithium ion batteries that includes 18 double coated cell sheets. All cells are connected in parallel and packed in a polymer laminate aluminum pouch case.

Table 4.1. Specifications of the commercial LiNiCoAlO<sub>2</sub>.

Item		Cell
Nominal capacity		10Ah
Nominal voltage		3.7V
Standard charge current		0.2C A
Max charge current		2CA
Charge cut-off voltage		4.2V±0.05V
Max discharge current		2C A
Discharge cut-off voltage		2.5V
Weight		235g
Dimension (mm)		6.7*53*197
Storage temperature	≤1month	-20 ~ 45°C
	≤3month	-20~ 35°C
	≤6month	0 ~ 25°C

All the electrode tabs of the same type are welded together to form the battery terminals. Each cell includes a layer of a positive current collector (CC), two positive electrodes (coated on both sides of the CC), and a separator containing an electrolyte, two negative electrodes (coated on both sides of the negative CC) and a negative current collector. The Li-ion cell is shaped to obtain the desired physical dimensions of the current collectors, electrodes, and

separator. X-ray diffraction analysis has been performed on the negative and the positive electrodes to estimate electrical characteristics and materials inside the battery. The battery uses nickel cobalt aluminum oxide with a stoichiometry close to Li  $[\text{Ni}_{0.85}\text{Co}_{0.10}\text{Al}_{0.05}]\text{O}_2$  known as (NCA) based cathode and mainly graphite ( $\text{Li}_x\text{C}_6$ ) based anode. The positive and negative current collectors are made from foils of aluminum (Al) and copper (Cu), respectively. The separator sheet that prevents physical or electronic contact between the anode and cathode is formed from polypropylene polyethylene copolymer that contains Lithium hexafluorophosphate (1M  $\text{LiPF}_6$ : and a mixture of ethylene carbonate (EC): dimethyl carbonate (DMC) containing additives) formulation. The active electrodes and separator layers are manufactured in the porous format that also includes the liquid electrolyte.

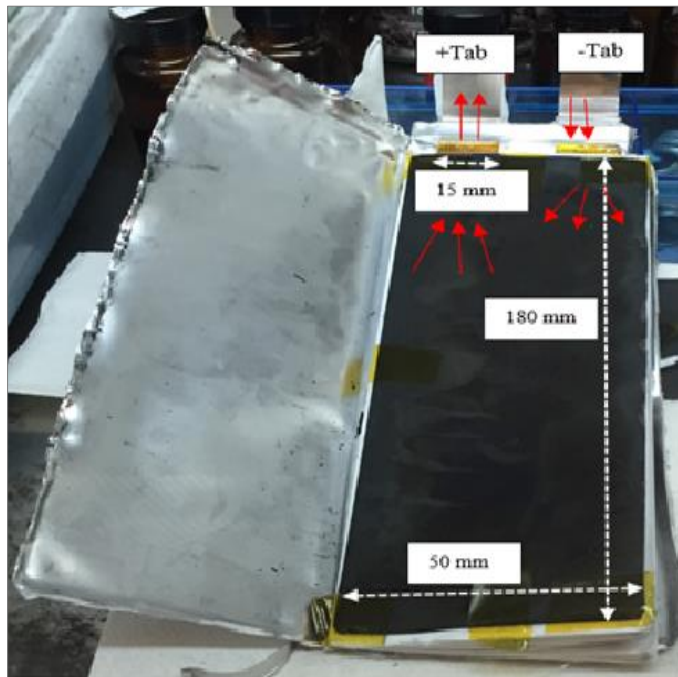


Figure 4.1. The stacked structure of the actual experimental battery with the pouch case.

The 10 Ah pouch Li-ion cell has been tested using commercial battery cycler (MACCOR model 4300 [28]) at various C-rates. To measure the time dependent temperature behavior through the constant current charge/discharge time, the battery is located in a small chamber with fixed temperature of 14 °C. In one set of experiments, we used four T-type thermocouples with the accuracy of  $\pm 0.5^{\circ}\text{C}$  such that they are attached to the battery surface.

In the other set of experiments, we used IR sensitive camera to map the heat on battery surface (results from IR camera are not included in this study). Thermocouples placed in different locations, one at the vicinity of the positive tab (T1), one at the proximity of the negative tab (T2), one at the center (T3) and one at the bottom of the battery (T4), as illustrated in Figure 4.2.

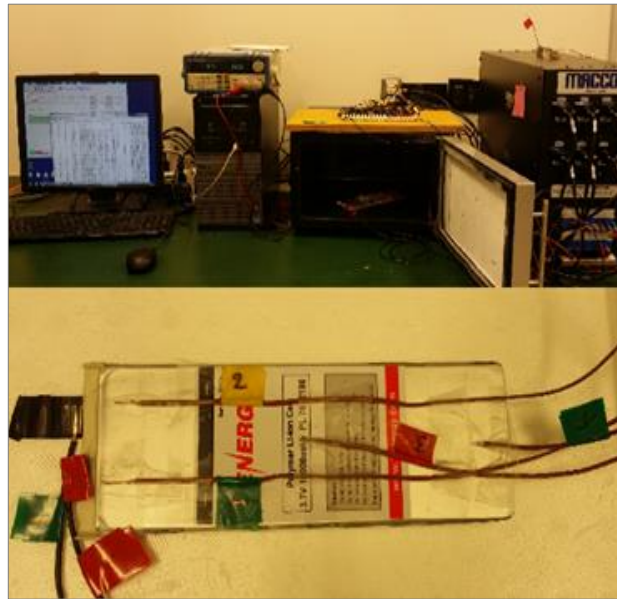


Figure 4.2. The experimental setup with the measuring T-type thermocouples and voltage sensors attached to the batteries surface and tabs, respectively.



Table 4.2. Model parameter in different regions.

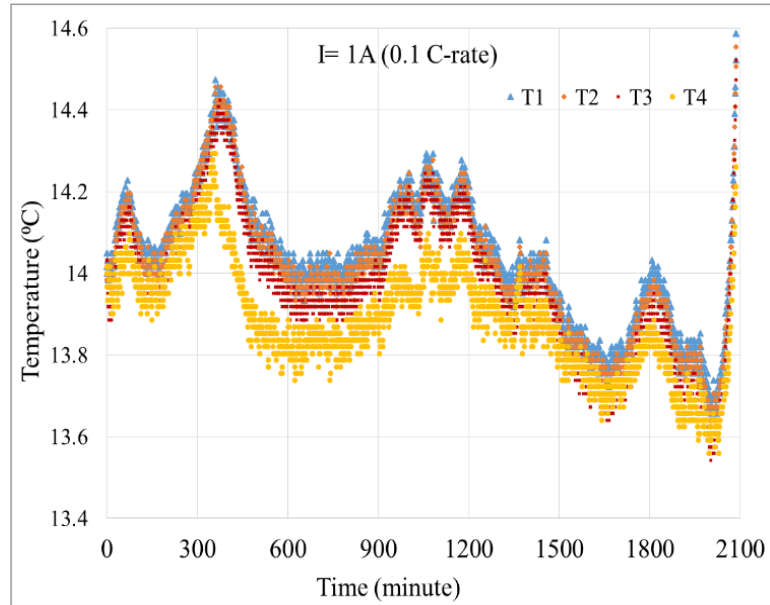
Parameters	Cu(CC)	Anode	Separator	Cathode	Al(CC)
Thickness, $L$ ( $\mu\text{m}$ )	10	60	40	75	20
Density [2, 3], $\rho$ ( $\text{kg m}^{-3}$ )	8900	2660	492	4770	2700
Specific heat capacity [2], $c_p$ ( $\text{J kg}^{-1} \text{K}^{-1}$ )	385	1437.4	1978	1172	903
Thermal conductivity [2], $K$ ( $\text{W m}^{-1} \text{K}^{-1}$ )	398	1.04	0.334	1.85	238
Electrode volume fraction, $\varepsilon$		0.3	0.4	0.28	
Maximum Li concentration in solid, $c_{s,max}$ ( $\text{mol m}^{-3}$ )		28688		20950	
Initial electrolyte concentration, $c_l$ ( $\text{mol m}^{-3}$ )		1000	1000	1000	
Solid phase electronic conductivity, $\sigma$ ( $\text{S m}^{-1}$ )	6.0E7	2.0	0	0.01	3.8E7
Bruggeman exponent [4]		1.5	1.5	1.5	
Anodic/Cathodic transfer coefficient, $\alpha_a, \alpha_c$		0.5		0.5	
Convective heat transfer coefficient, $h$ ( $\text{W m}^{-2} \text{K}^{-1}$ )[2, 5]			1e1.75		
Faraday's constant, $F$ ( $\text{C mol}^{-1}$ )			96487.0		

### 4.3.2 Experimental results

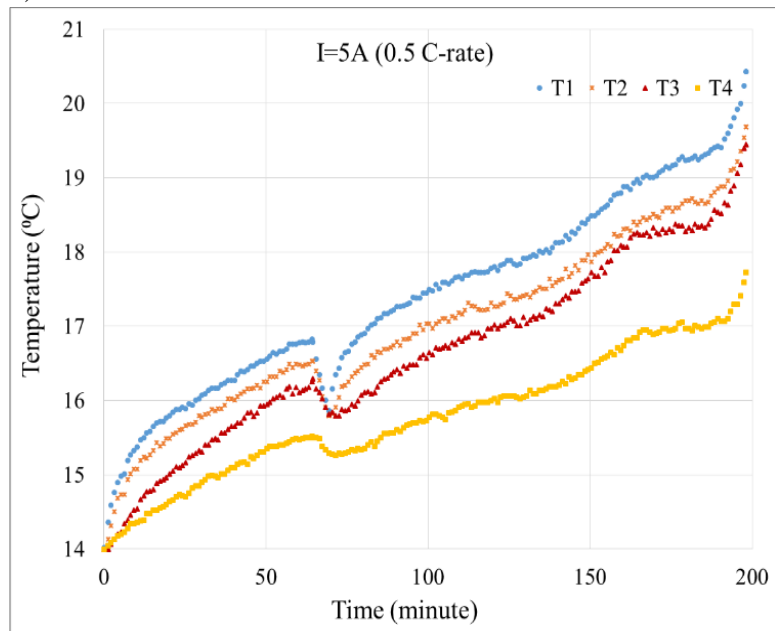
Figure 4.3.a-c provides the temperature variations of the battery surface with respect to time at 0.1, 0.5 and 0.8C-rates respectively. Figure 4.3.d shows the relative positions of thermocouples (T1-T4) on the battery surface. Results show that the surface temperature close to the positive tab for T1 increased about 0.6 °C, 6.4 °C and 10.9 °C above the initial temperature after one charge/discharge cycle at 0.1C, 0.5C, and 0.8C, respectively. Temperature from thermocouple T2 for the same C-rates was raised to about 0.55 °C, 5.7 °C, and 9.5 °C. Similarly, the obtained results from T3 at 0.1, 0.5 and 0.8C-rates were 0.52 °C, 5.4 °C, and 8.4 °C individually; for the T4 were 0.26 °C, 3.7 °C, and 5.7 °C respectively. The measured surface temperature via thermocouples at different locations confirmed that higher temperature is observed around the

positive tab as compared to other areas and that the lowest temperature is seen in the opposite direction at the bottom of the cell.

a)



b)



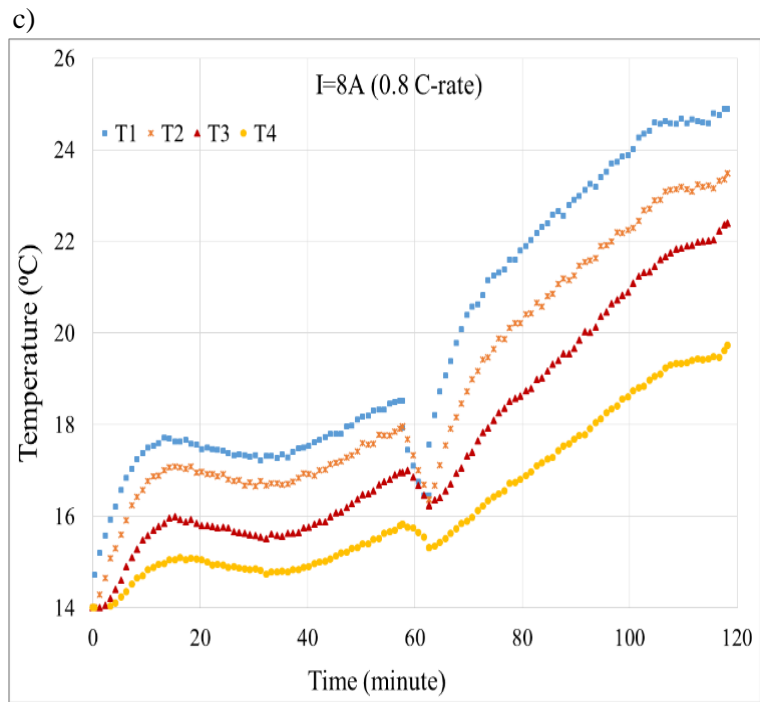


Figure 4.3. Surface temperature profiles at a) 0.1 C-rate, b) 0.5C-rate and c) 0.8C-rate. d) Temperature is measured closed to the positive tab (T1, blue lines), close to the negative tab (T2, orange lines), center (T3, red lines) and at the bottom of the battery (T4, yellow lines).

It can also be verified that there is a higher surface temperature at higher C-rate as expected. The internal heat generated due to the heat of reactions and Joule heating causes the variation of temperature profile with cycle time which will be discussed later.

The current and voltage profiles during charge and discharge with a short rest time (5 minutes) at 0.8 C-rate are shown in Figure 4.4. It is illustrated that at the beginning of the rest period the voltage dropped faster due to electrical IR loss. Later the voltage decreases more gradually due to the slower diffusion of ions in and from solid electrodes and in the liquid electrolyte. The voltage drops are primarily because of the IR and diffusion settling in the cell during the rest period.

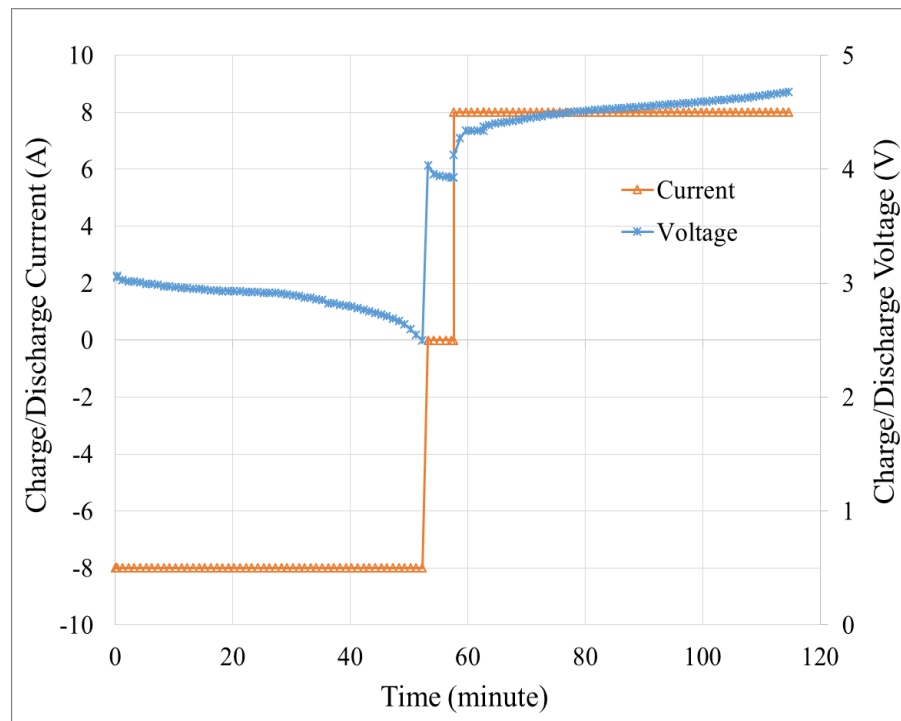


Figure 4.4. Current and voltage profiles versus time during charge and discharge containing a short rest period of 5 minutes at 0.8 C-rate.

Since the capacity of the battery is 10Ah voltage response of the battery during discharge processes at 0.1C, 0.5C and 0.8C discharge rates corresponding to 1A, 5A and 8A are measured. In the Figure 4.5 maximum capacity of 15.68 Ah at 0.1C discharge rate and the minimum capacity of 7.31 Ah at 0.8C discharge rate are reported within the voltage limits of 4.2 – 2.5 volts. The battery capacity is rated at 0.2C. As the usable capacity of the battery depends on the current discharge rate, consequently the higher the discharge current, the lower is the usable capacity within the upper and lower voltages, and this finding is in agreement with other similar findings in the literature [41].

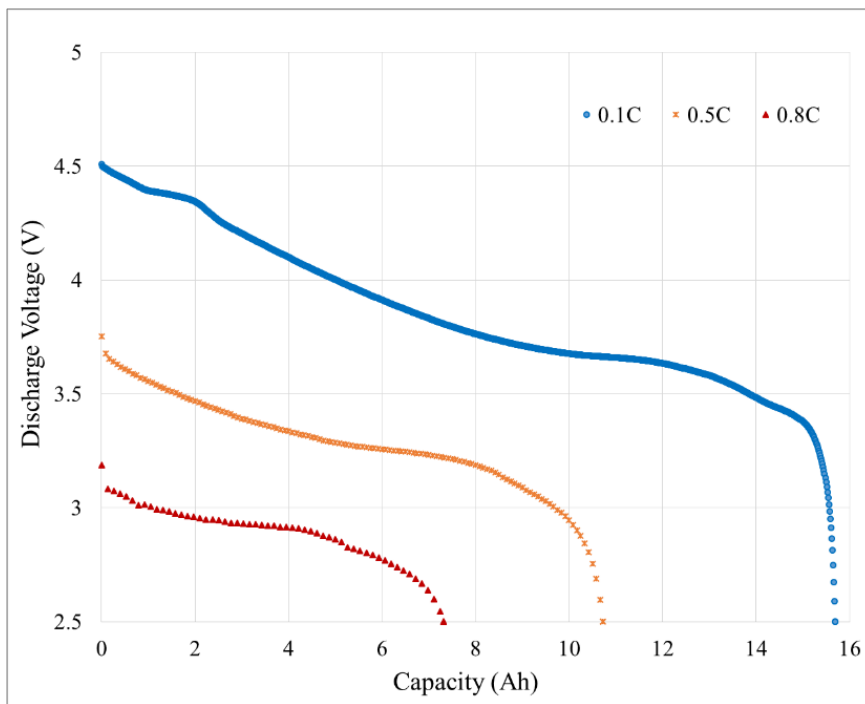


Figure 4.5. Experimental data on the variation of battery voltage versus capacity for different discharge conditions in C-rate.

#### ***4.4 Model development***

In this part of work, the model development and simulation case studies performed on COMSOL Multiphysics version 5.2a software are conducted to predict the LIB charge-discharge behavior and heat generation rate of cells at different C-rates.

To illustrate the electric potential, total charge/discharge current, voltage loss, electrolyte phase concentration, and local current density, electrode particle heat generation a cross section in one-dimensional electrochemical-thermal model is proposed. It implies that edge effects in the length and height of the battery are neglected.

First results are obtained from a 1D time-dependent electrochemical model after applying 8A to the positive current collector terminal boundary. The subsequent results are achieved by coupling a time- dependent thermal model with the electrochemical model.

To study the relationship between the cell units and the battery during the discharge process, 1D ECT coupled model has been extended to a 3D cell stacks model including multiple electrode pairs via coupling the lithium ion battery module and the heat transfer module.

It is assumed that the battery consists of 18 cell stacks on both 1D and 3D models. Unit cells are made by defining five different layers, and the material has been set for all cell components according to the battery under experiment. Moreover, the initial temperature of the battery is assumed to be equal to the ambient temperature, and it has been set to 14 °C during the discharge process according to the experimental test. Convective heat flux has been used to calculate the heat dissipation on the surface of the cell.

#### ***4.4.1 Electrical model***

The electrochemical model provides the relationship of current distribution inside the battery layers, and the local charge transfers current density, exchange current density and over potential. We used the general treatment that introduced by Newman for modeling the current–voltage relations inside the cell components [30].

The discharge process causes lithium ions inside solid  $\text{Li}_x\text{C}_6$  to migrate towards the electrode surface and into the electrolyte layer, and reside in the cathode material of the battery. During charge process, the ions move through the electrolyte from the positive to the negative electrode and attach to the carbon where they produce lithiated NCA,  $\text{LiNiCoAlO}_2$ .

Figure 4.6 gives a schematic illustration of a unit cell of the battery during charge/discharge process. It shows pores of polymer components, i.e., electrodes and separator are filled with an electrolyte liquid which allows movement of lithium ions between the electrodes. The arrows specify the direction and magnitude of the current flowing in the current collectors. The current from the external circuit flows into the cell distributed on the entire current collectors, through the tabs and then flows into all the local regions containing active materials distributed on the entire current collectors.

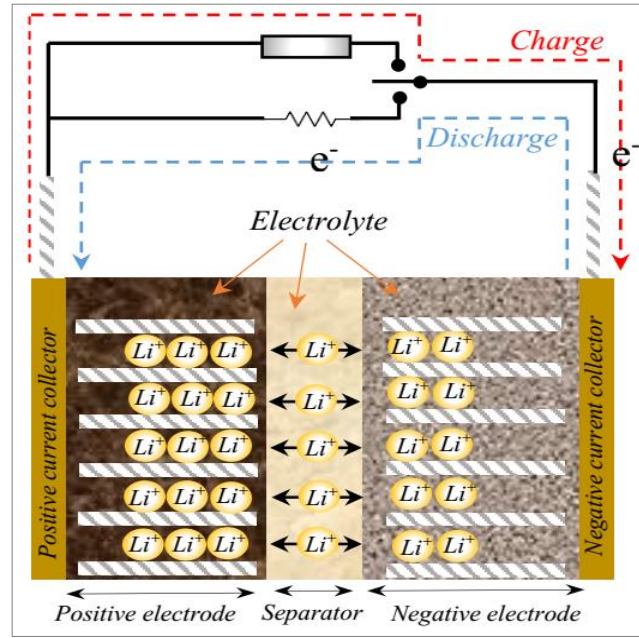
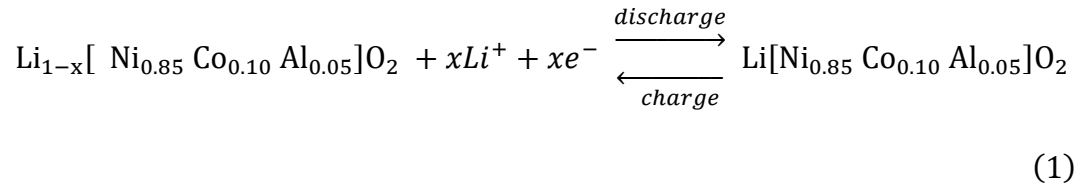
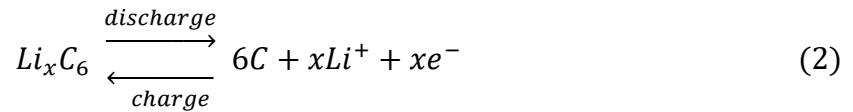


Figure 4.6. Schematic of a unit cell of the battery including positive and negative porous electrodes, a porous separator, and current collectors during charge and discharge process.

The electrochemical reactions during the charge/discharge can be expressed as in the cathode composite electrode [42] due to redox reactions on the transition metals, given by,



in the anode composite electrode [42],



The charge balance equation for electron transport in the solid phase  $i_s$  is formulated as:



$$i_s = -\sigma_s^{eff} \nabla \phi_s \quad (3)$$

To determine the effective conductivities of the solid phase  $\sigma_s^{eff}$ , the following equation is used,

$$\sigma_s^{eff} = \sigma_s \varepsilon_s^\gamma \quad (4)$$

where  $\sigma_s$  is electrical conductivity,  $\varepsilon_s$  is the electrode volume fraction, and  $\gamma$  is the Bruggeman coefficient that is set to 1.5 in this model,  $\phi_s$  is the solid phase potential.

The charge balance equation for lithium ion transport in the electrolyte phase is given below,

$$i_l = -\sigma_l^{eff} \nabla \phi_l + \frac{2RT\sigma_l^{eff}}{F} \left(1 + \frac{\partial \ln f_{\pm}}{\partial \ln c_l}\right) (1 - t_+) \nabla (\ln c_l) \quad (5)$$

where  $\sigma_l^{eff}$  defines the effective ionic conductivity of the electrolyte phase, the average molar activity coefficient is  $f_{\pm}$ ,  $t_+$  is the transference number for lithium ions, and  $c_l$  is the lithium ion concentration in the liquid electrolyte phase.  $R$  and  $T$  are universal gas constant and temperature of the electrolyte respectively [36, 43].

In the electrolyte, the current collector boundaries are ionically insulating for the ionic charge balance. On the negative electrode's current collector, a potential of 0V used for the electronic current balance. At the positive current collector, the current density is specified according to the C-rates.

The internal boundaries in front of the separator are electronically insulated for electronic current in adjacent layers. The local charge transfer current density  $i_{loc}$  in the electrode is defined by Butler-Volmer equation given below:

$$i_{loc} = i_0 \left\{ \exp\left(\frac{\alpha_a F}{RT} \eta\right) - \exp(\eta) \right\} \quad (6)$$

where  $i_0$  is the exchange current density from Equation (7),

$$i_0 = F(k_c)^{\alpha_a} (k_a)^{\alpha_c} (c_{s,max} - c_s)^{\alpha_a} (c_s)^{\alpha_c} \left(\frac{c_l}{c_{l,ref}}\right)^{\alpha_c} \quad (7)$$

In these equations  $\alpha_a$  and  $\alpha_c$  are the anodic and cathodic charge transfer coefficients,  $\eta$  is the local surface over potential,  $F$  is the Faraday's constant,  $k_c$  and  $k_a$  are cathodic and anodic rate constants respectively. The  $c_{s,max}$  is the maximum lithium concentration at the surface of the active electrodes, and  $c_{l,ref}$  is the electrolyte reference concentration on the surface of the active particles. The equation for the overpotential is :

$$\eta = \phi_s - \phi_l - E_{eq} \quad (8)$$

where  $E_{eq}$  is the open circuit potential,  $\phi_s$  is the solid phase potential, and  $\phi_l$  is the electrolyte phase potential. The local current obtained from the model is used to study the electrochemical behavior of the cell and get the Joule heating during charge-discharge processes.

#### 4.4.2 Thermal model

Heat is generated within the active battery material. The thermal model is developed to predict the temperature distribution inside the battery using energy balance equation.

The energy balance calculations that are affected by the reversible heat generated due to the reversible chemical reaction and the irreversible ohmic heat are necessary to obtain consistent prediction of heat generation inside the battery and the time-dependent temperature profiles [5].

Thus, it is essential to have a strong coupling between the electrochemical and thermal models of the battery.

The generated heat caused by reversible entropy change can be defined as [4]:

$$\Delta S = -\frac{\partial \Delta G}{\partial T} = -nF \frac{\partial V^\circ}{nT} \quad (9)$$

where  $\Delta G$  is the Gibbs free energy change and is given by,

$$\Delta G = -nFV^\circ \quad (10)$$

During the charge/discharge processes, the battery generates heat that can be described as,

$$\dot{q} = I(V^\circ - V) - IT \frac{\partial V^\circ}{\partial T} \quad (11)$$

By considering the battery as a unit, the energy equation would be in the following form [36, 43]:

$$\rho C_p \frac{\partial T}{\partial t} = k \nabla^2 T + \dot{q} - hA(T - T_a) \quad (12)$$

where  $\rho$  is density,  $C_p$  is the battery heat capacity,  $h$  is the convection heat transfer at the outer surface of the battery coefficient,  $A$  is the battery surface area, and  $T_a$  is the ambient temperature. Appropriate selection of  $h$  allows combining the effect of different cooling rates at different stages of heat rejection.

Since the electrode thickness in the  $z$ -direction (normal to electrode surface) is very small compared to their dimensions in  $x$ - and  $y$ -directions, the temperature will be uniform in  $z$ -direction [44]. Thus in the thermal model, the heat is assumed to be independent of the  $z$ -direction. Consequently, the thermal conductivities are anisotropic in the 3D thermal model has a higher value along the battery sheets than in the direction normal to the sheets. In the  $z$ -direction, the thermal conductivity  $K_{T,y}$ , is calculated from the formula [45].

$$K_{T,y} = \frac{\sum L_{i,y}}{\sum \frac{L_{i,y}}{K_{T,i,y}}} \quad (13)$$

The thermal conductivities in the  $x$ - and  $z$ - directions are calculated according to [45]

$$K_{T,x} = \frac{\sum L_{i,x} K_{T,i}}{\sum L_{i,x}} \quad (14)$$

$$K_{T,z} = \frac{\sum L_{i,z} K_{T,i}}{\sum L_{i,z}} \quad (15)$$

where  $L_i$  are the thicknesses of the layers of the cell, and  $K_{T,i}$  is the thermal conductivity of the materials constituting these layers. The density ( $\rho$ ) and heat capacity  $C_p$  of the active battery material is calculated according to [45],

$$\rho = \frac{\sum L_i \rho_i}{\sum L_i} \quad (16)$$

$$C_p = \frac{\sum L_i C_{p_i}}{\sum L_i} \quad (17)$$

In an improved simulation approach, the proposed method is extended to a 3D ECT model to accommodate the genuine non-homogeneous heat generation in the present model. In this approach, the 3D computational model consists of active battery materials and the positive and negative tabs. The performance of this model is demonstrated in the next section.

#### ***4.4.3 Simulation results***

Figure 4.7 represents the charge/discharge current and voltage performance of the model at 0.8C-rate after 60 minutes of discharge, 5 minutes of open-circuit (rest period) and 50 minutes charge at 8A, and finally an open-circuit condition. The voltage profile presented in Figure 4.7 shows that during both discharge and charge, the cell voltage experiences ohmic losses of around 63 mV and a concentration overpotential of approximately 22 mV. The current is set to 0A during the rest period. It means an immediate relaxation of the voltage is caused due to the relaxation of ohmic losses followed by a slower relaxation of the concentration overpotential.

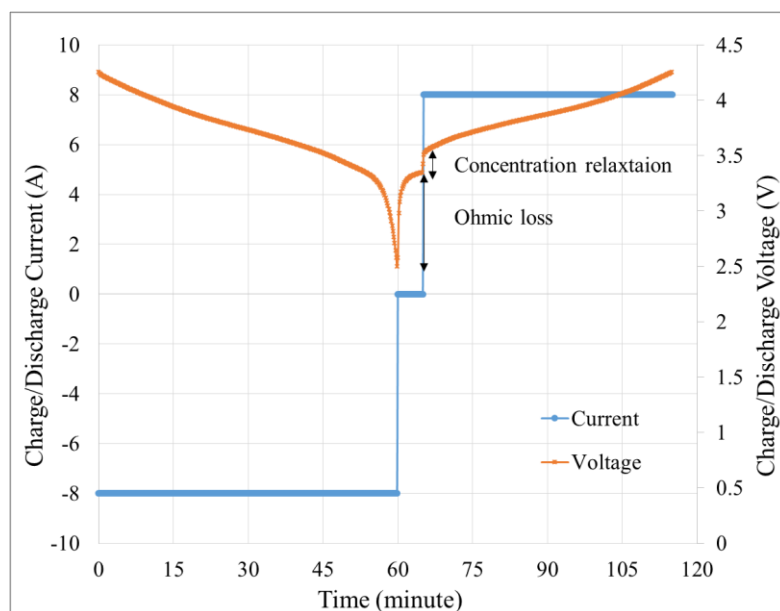


Figure 4.7. Charge/Discharge current and voltage at 0.8C as a function of time.

The cell voltage deviated from the open circuit voltage once the current flow through the cell because of the overpotential or electrochemical polarization.

The overpotential can be represented as the charge transfer or activation overpotential, the ohmic overpotential, and the concentration overpotential.

The reaction overpotential and electrolyte potential are two primary losses in the battery as shown in Figure 4.8.a. The electrolyte potential curves are assumed to be zero at the center of the separator since the variation between two curves and their gradients are concerned. This plot shows that the electrolyte potential at the end of discharge is increased. This increase suggests that a small concentration of polarized particles/ions cause the growth of ohmic heat generation during discharge. The polarization heat is equal to the overpotential multiplied by the current, and it is mainly due to the Joule heating inside the battery [29]. The influence of

the polarized ion concentration is indicated by considering the difference between the initial electrolyte potential and the potential at the end of discharge step.

Therefore, to investigate the reason for the steep voltage decrease, the electrolyte concentration profile at several stages during the charge and discharge cycle is observed in Figure 4.8.b. Because of the intercalation reaction in the cell, the lithium ion concentration in negative electrode at the beginning of charge and the end of charge are  $970 \text{ mol/m}^3$  and  $846 \text{ mol/m}^3$  respectively. These are lower than the lithium ion concentration in positive electrode at the beginning of charge ( $1004 \text{ mol/m}^3$ ) and the end of the charge ( $1007 \text{ mol/m}^3$ ) time. Observably, due to de-intercalation, the Li-ion concentration at the beginning and end of discharge process are higher in the negative electrode than the positive electrode [16].

The energy loss due to the polarization is dissipated as permanent heat through both charge and discharge cycles. The low effective diffusion coefficient in the electrolyte leads to a significant concentration polarization in the cell which causes a variation in ionic conductivity and concentration overpotential.

Figure 4.9 shows the local current density distribution within the battery at the different time during the discharge. The local current density is affected by the distribution of the lithium concentration at the surface of particles in the solid phase variations. By the variation of surface concentration, the equilibrium voltage also changes, resulting in variation of reaction overpotential as well as local current density that causes considerable overall voltage loss in the battery.

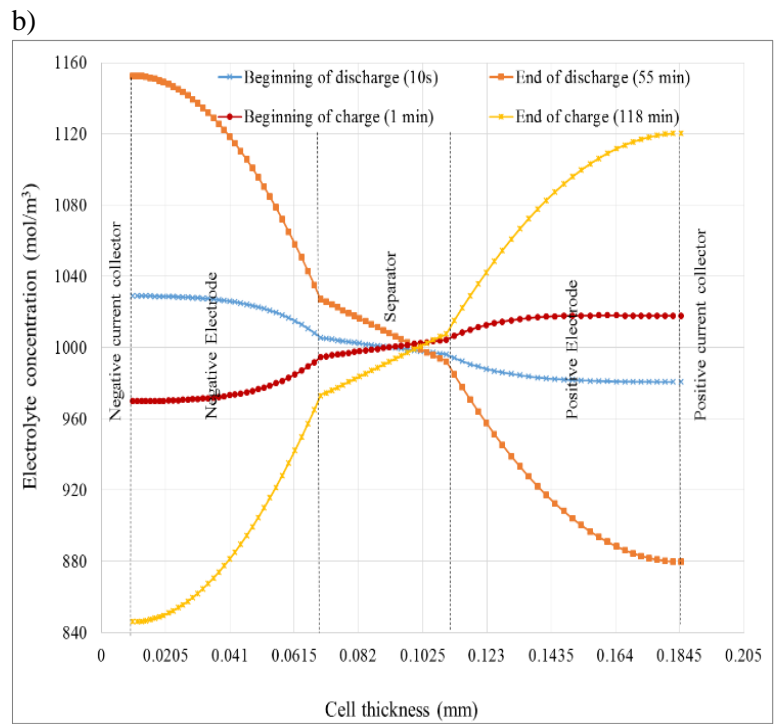
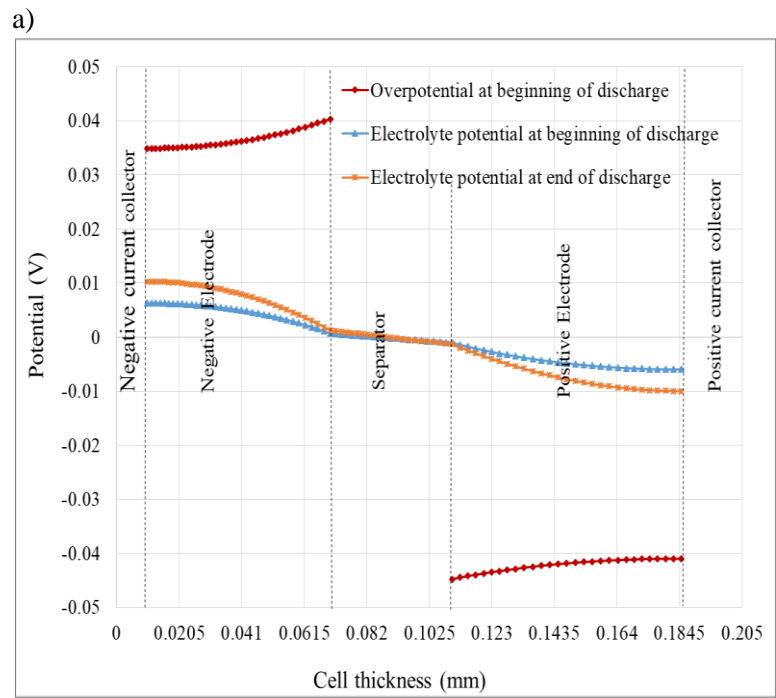


Figure 4.8. a) Comparison of over potential and electrolyte potential at the beginning and end of discharge. b) Electrolyte concentration outline at different times.



Lithium-ion concentration is a function of C-rate, which causes the ohmic heat generation in an electrolyte. So, the ohmic heat generation is caused by the gradient of the lithium ion concentration, causing an increase in internal ionic resistance [16].

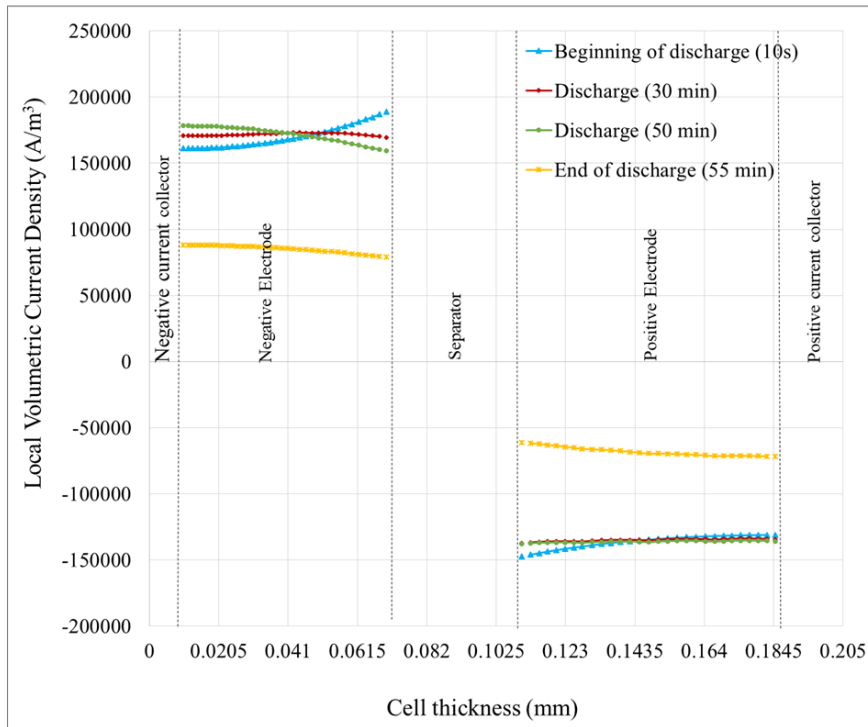


Figure 4.9. Local current density distribution within the battery during the discharge at various times.

The concentration distribution of lithium in the solid phase during the discharge is plotted in Figure 4.10. The negative electrode's concentration in the particle center at 3600 second varies from  $3565 \text{ mol/m}^3$  to approximately  $456 \text{ mol/m}^3$  at the surface with a consistent difference along the width of the cell.

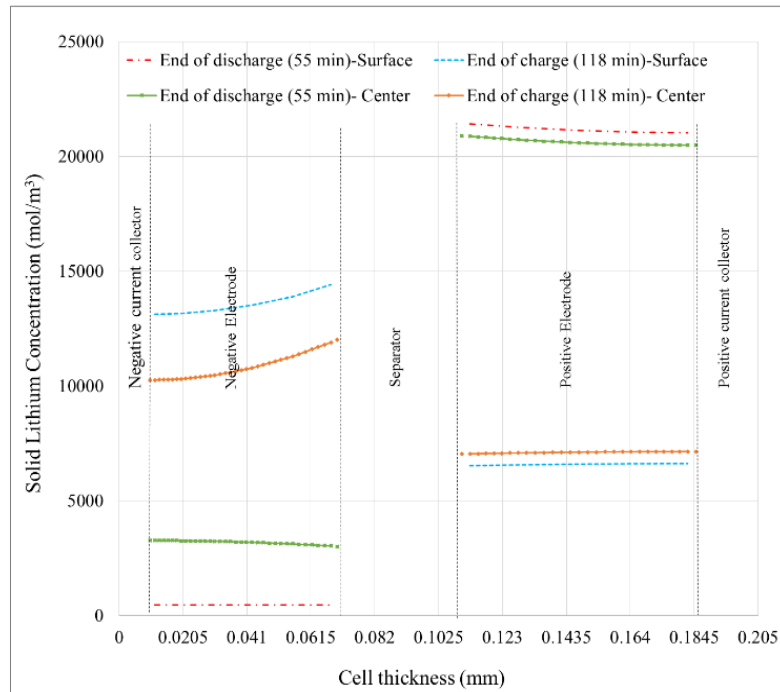


Figure 4.10. Concentration distribution of lithium in the solid particle.

The variation along the width at the positive electrode is around  $21406 \text{ mol/m}^3$  surface concentration at the electrolyte interface and  $21016 \text{ mol/m}^3$  at the positive current collector. This small variation can demonstrate a uniform current distribution due to the robust electrode conductivity.

The battery is assumed to be in a full charge state initially. The accuracy of the model was validated by comparing with experimental data. Figure 4.11.a shows the variation of battery open circuit voltage versus time during the discharge process with respect to time at 0.8 and 0.5 C-rates. The average calculated temperature during 0.8C, 0.5C constant current discharge processes has been measured experimentally to explain the spatial and temporal temperature behavior in the battery. To maintain the temperature rise within the allowed range

(less than 30 K), a small convective heat transfer coefficient,  $h = 5 \text{ Wm}^{-2}\text{K}^{-1}$ , is applied to the surfaces and boundaries of the battery [12, 46, 47]. Temperature rise within the battery model after 0.5C discharge is 3.6 °C and after 0.8C is 6.2 °C. Figure 4.11.b compares the measured surface average temperature profiles of the battery during discharge at 0.5C and 0.8C with the ones obtained from the numerical model, at varying discharging times, to validate the results of the proposed numerical simulation model. Overall, the numerical simulation results are in excellent agreement with the data obtained from the experiments.

To analyze and compare the temporal behavior of the heat generation in the negative electrode, separator, and positive electrode, ohmic heat, and entropic heat are plotted in Figure 4.12.a. These are calculated from the collected data at the end of discharge time (55 minutes). It is observed that both reversible and irreversible heat generations are more significant in regions close to the separator due to higher current density and reaction rate in these areas. Figure 4.12.b shows the total heat generation at the beginning and end of discharge and charge processes. During the discharge process, the internal resistance of cathode varies from its minimum value to its maximum. Therefore, the lowest heat generation in cathode side is observed at the beginning of discharge. At the end of discharge, the resistance of cathode is maximum which leads to high heat generation. However, it should be mentioned that the temperature gradient throughout the cell surface is negligible because of the small Biot number (Bi) described as follows:

$$Bi = \frac{hl}{K} = \frac{10 \times 0.00182}{30} = 6.1 \times 10^{-4} \ll 1 \quad (18)$$

where  $h$  is convection heat transfer coefficient,  $l$  is the ratio of cell volume to surface area, and  $k$  is the cell thermal conductivity. The change in entropy generation, due to the different charge and discharge reactions, causes the difference in heating rate between charge and discharge. Our proposed one-dimensional electrochemical simulation can accurately predict the electrochemical performance of any size LIB at various C-rates. The heat generation is non-homogeneous in a real battery due to current density distribution and local internal resistance [26, 36]. Consequently, the geometric design of electrodes and current collectors are important parameters to design a thermally stable LIB especially at high C-rates [36].

#### ***4.4.4 3D electrochemical –thermal model***

A LIB consists of many cell units that have great influence of ECT on battery's performance and safety. The 3D electrochemical –thermal model developed in this work is an extension of the proposed 1D model over the volume to predict, analyze and optimize the more complex time-dependent interactions in the batteries.

To optimize the design of a thermal management system of LIBs for larger scale applications, the perception of the 3D distribution of potential, current, reaction rate, temperature, heat generation, and tab effects are critical. This model used the variation of voltage as a function of current to solve the 3D current distribution in the battery that increased the computational efficiency and convergence stability of a fully resolved 3D system of non-linear differential equations.

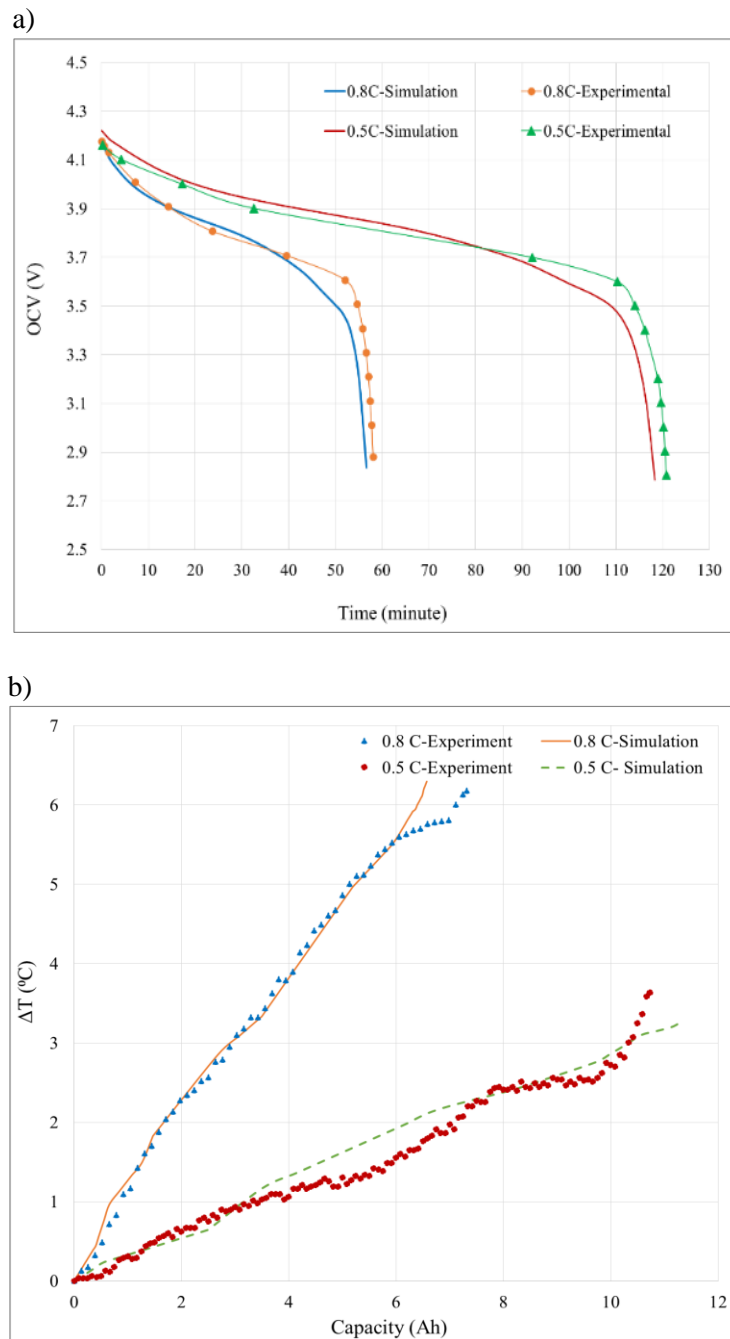


Figure 4.11. Comparison of simulation results to experimental during the discharge constant current at 0.5 and 0.8 C-rates. a) Variation of battery open circuit voltage versus time. b) Average surface temperature profiles of the battery. Symbols correspond to measured values and lines represent the calculated values.

Figure 4.13.a illustrates the schematic of a single cell unit assembly consisting of current collecting tabs, two positive porous electrodes, separator and two negative porous electrodes. The computational domain of a 3D battery composed of 18 double layers cells is shown on Figure 4.13.b.

The current density distribution at the end of discharge (55 minutes) within the battery is plotted in Figure 14. The red streamlines in Figure 4.14.a. are shown the direction of the current which is flowing from the negative tab toward the positive tab. The electrode current density magnitude in the battery is indicated by the contours in Figure 4.14.b. It is observed that by increasing the distance from the negative tab, the magnitude of the current density has been decreased. The local current density ( $i_{loc}$ ) calculated by equation (6), which is very small close to the edges and bottom of the battery, deliver the charges in the electrochemical reaction from the negative electrode to the positive electrode.

The potential difference between the negative current collector and positive current collector of the battery is defined as its working voltage. Figure 4.15 displays the distribution of the electric potential within the positive current collector during the discharge at 0.8C from the various DOD. The DOD is assumed from a full charge battery (4.2V). It can be observed that the value of the potential at the discharge time of 10s is 4.2V, it is 3.5V and 2.5V at the discharge time of 30 min and 55 min, respectively.

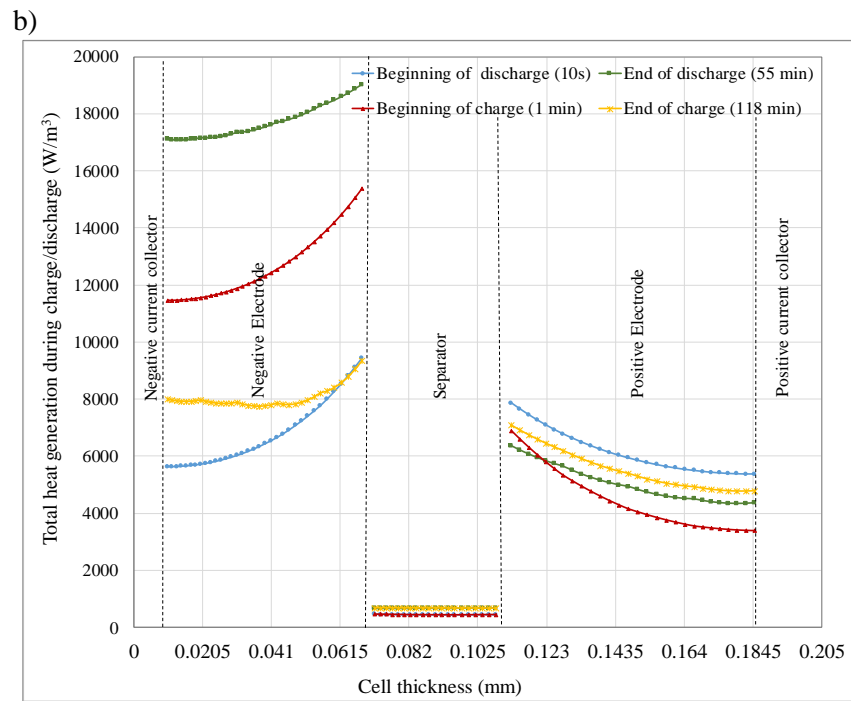
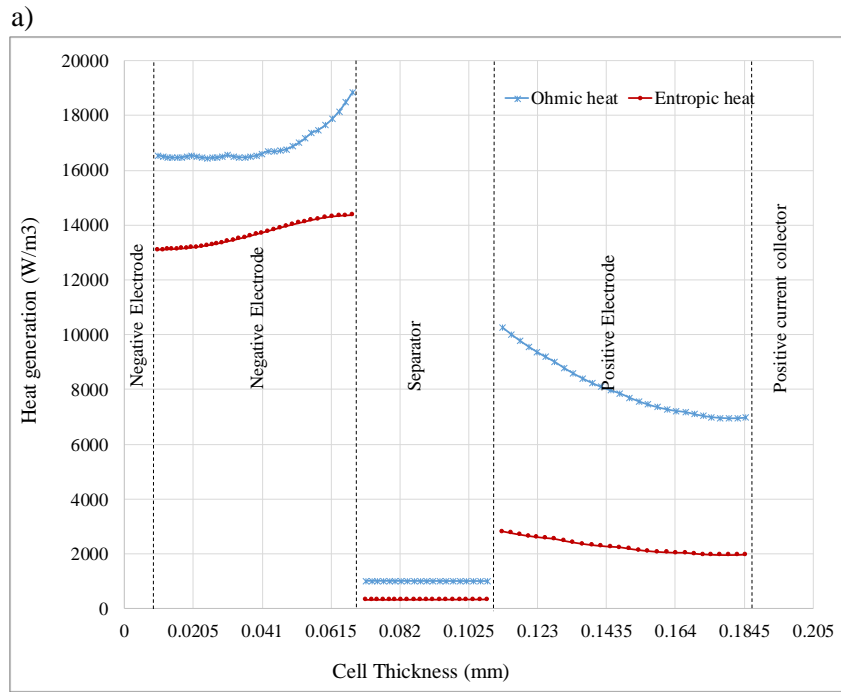


Figure 4.12. a) Temporal evaluation of ohmic heat and entropic heat at the end of discharge process. b) The total heat generated within the battery during charge/discharge process.

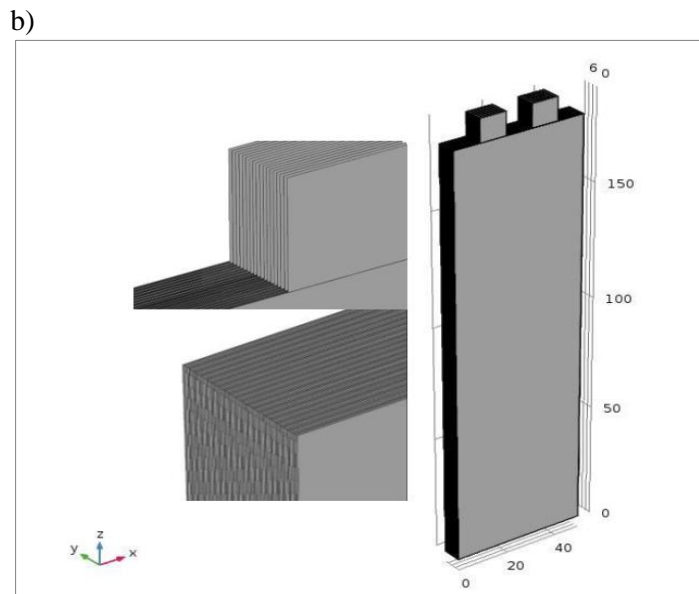
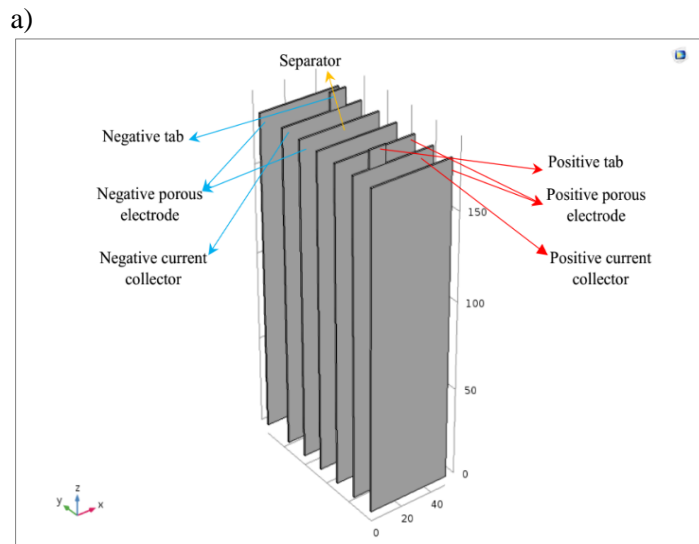


Figure 4.13. a) Schematic of a single cell unit assembly. b) Geometry of the computational domain (electrode-separator stack) of a pouch-type 3D LIB consisting of 18 double layers cells.



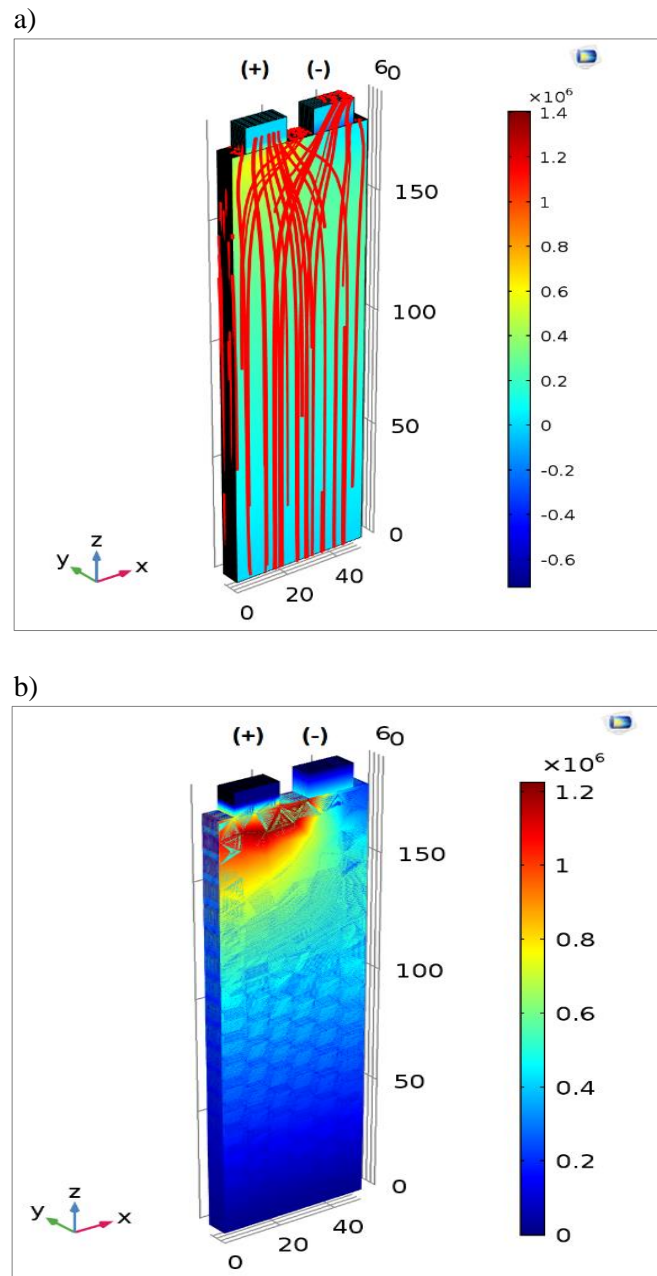


Figure 4.14. a) The electrode current density vector within the battery (red streamlines) is shown the current enter into the negative tab and exit to positive tab during the discharge process ( $t=55$  min). b) The electrode current density magnitude within the battery is shown using contours.

In Figure 4.16, the calculated and measured temperature response of the battery at 0.8C during the discharge process is shown. Plots (a)-(c) show the surface temperature distribution of the 3D model after 1 minutes, 30 minutes and 55 minutes respectively.

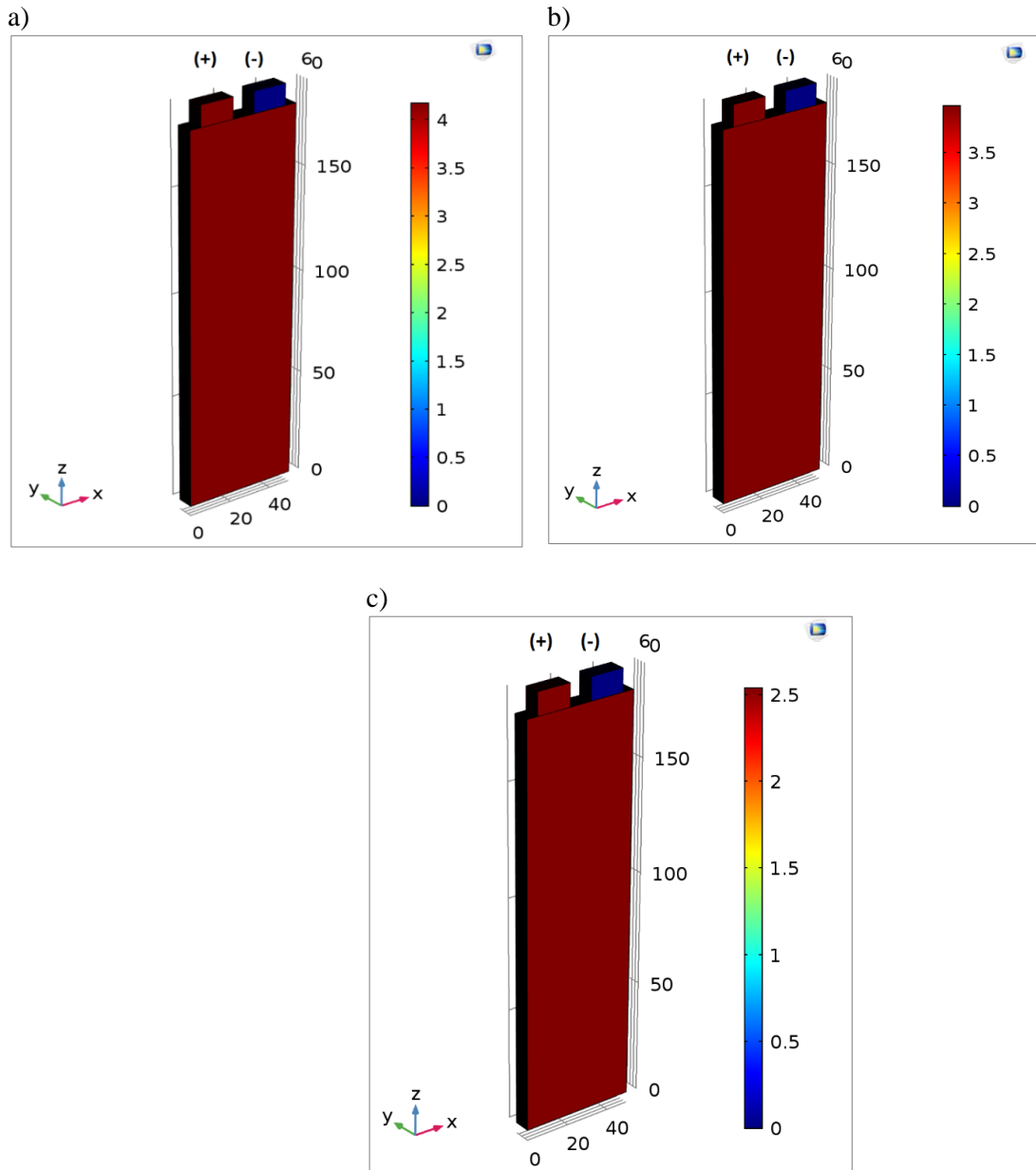
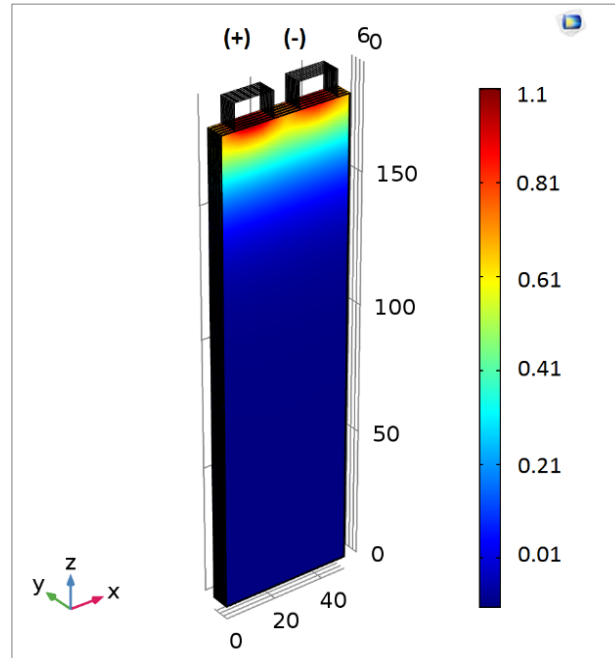


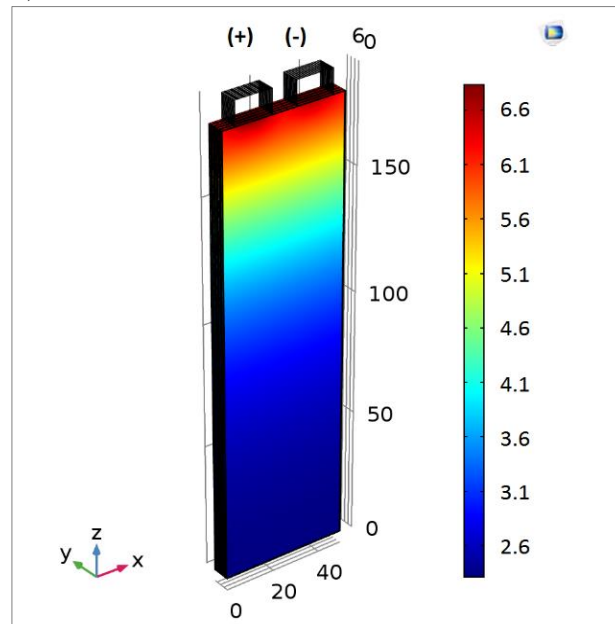
Figure 4.15. Electric potential distribution on the positive current collector during the discharge process at 0.8C: a) after 10 seconds, b) after 30 minutes, and c) after 55 minutes.

The maximum temperature difference is observed around the positive tab because the heat generation is much faster all over the tab.

a)



b)



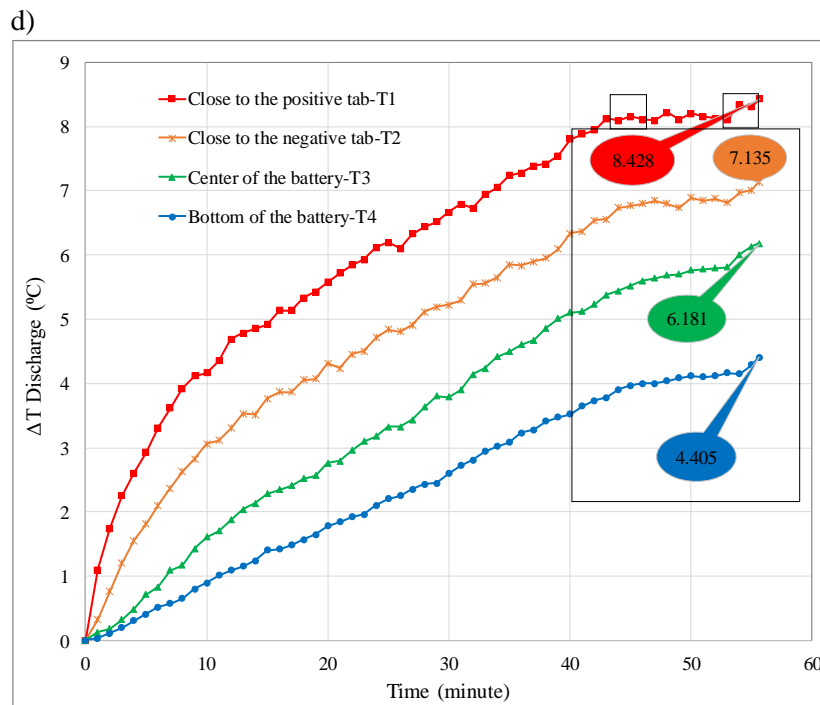
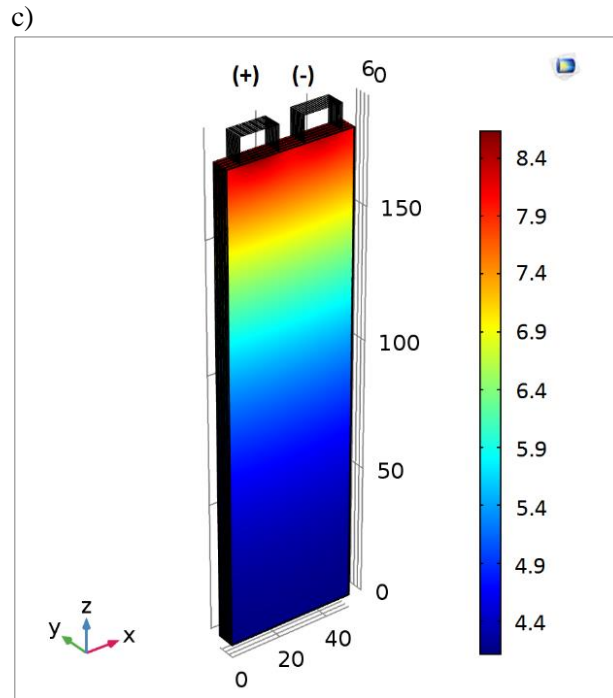


Figure 4.16. Surface temperature distribution from based battery model during the discharge at 0.8C constant current. a) After 1 minute. b) After 30 minutes. c) After 55 minutes. d) From four different locations (close to the positive tab, close to the negative tab, center of the battery and bottom of the battery) are shown to validate the time dependent temperature results obtained from the 3D model.

Moreover, since the positive current collector is the main heat source in the tabs region, the temperature decreased from the positive tab in the direction of the negative tab. Plot (d) correspond the measured surface temperature profile against time from four different locations using T1-T2 thermocouples to validate the time-dependent temperature results obtained from the 3D model.

As displayed in the plot (c) the maximum temperature difference at the end of discharge, between the hottest and coldest spot are 8.4 °C and 4.4 °C, respectively.

It is shown that the temperature is higher in the region close to the tabs than the center and the bottom of the battery.

This comparison shows favorable agreement between numerical simulation and experimental data. It can be further explained by the plot of current density around the positive tab illustrated in Figure 4.14 that is greater than the current density on the negative side.

Furthermore, to demonstrate the accuracy of our calculations, predictions for the OCV and average temperature response of the proposed 3D model are compared to voltage and temperature response of the experimented battery during a 0.8C-rate discharge in Figure 4.17 (a)-(b) respectively. The current distribution produces potential gradient on both electrodes, consequently affecting the heat generation rates and temperature distribution within the battery. Therefore, adding the positive and negative tabs to the 3D battery model can influence the current distribution on the current collectors.

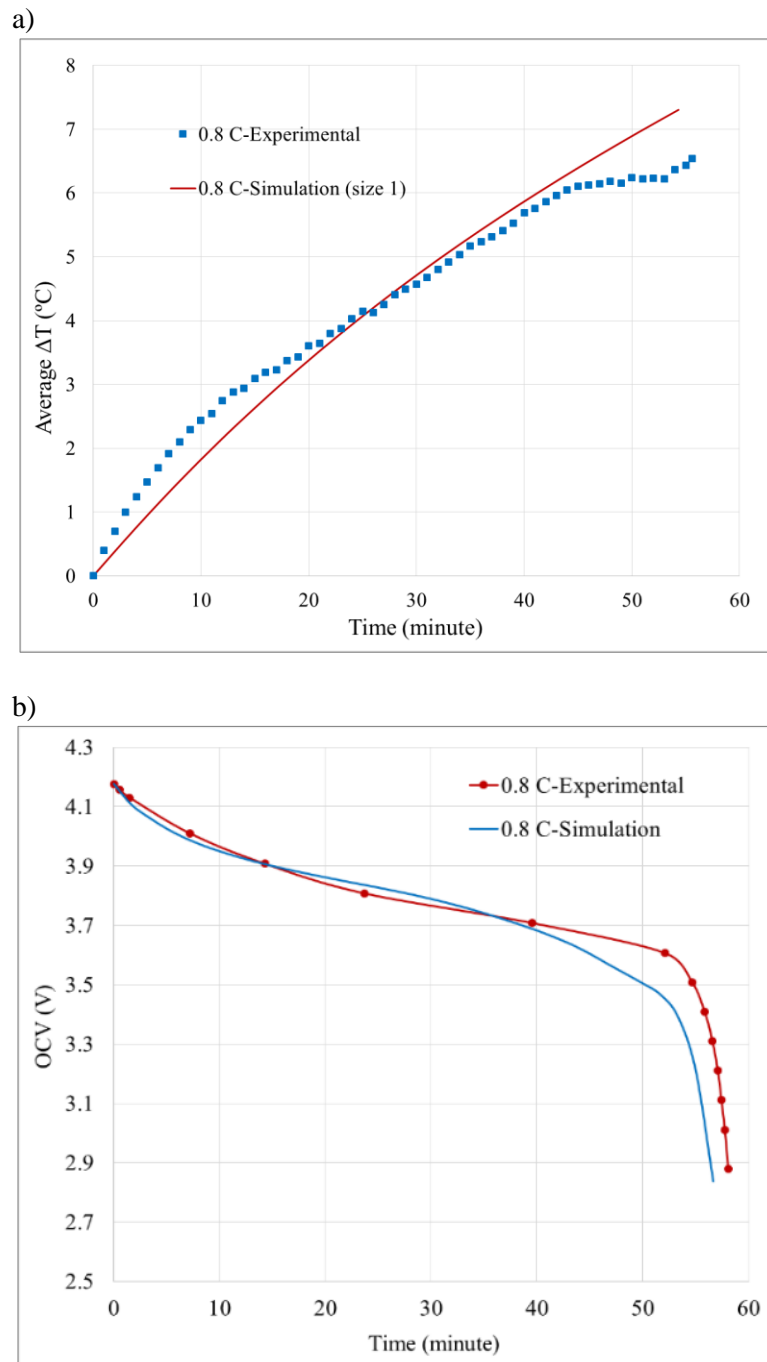


Figure 4.17. 3D model performance validation: a) calculated average surface temperature profile of the battery at 0.8C constant current is compared to experimental temperature measurement, b) calculated OCV voltage response of the battery during constant-current discharge process at 0.8C rate validated by experimental OCV measurement.

#### ***4.5 Conclusion***

The electrochemical and thermal behavior of pouch-type Li-ion batteries during charge/discharge cycles was investigated experimentally as well as numerically. Initially, a 10 Ah LiNiCoAlO<sub>2</sub> Li-ion cell at 0.1, 0.5 and 0.8 C-rates was experimentally examined. The temperature rise during the charge and discharge cycles were accurately measured using four T-type thermocouple sensors attached to the surface of the battery at various locations. The results indicated that accumulation of the temperature in regions close to the tab is higher than those in the center and close to the bottom of the battery. Furthermore, the magnitude of the heat is greater on the positive tab with respect to the negative tab.

A 1D electrochemical-thermal coupling model was developed to predict and optimize the electrochemical-thermal behavior of the considered LIB. Later the proposed numerical was extended to a 3D electrochemical-thermal model to investigate the current distribution and heat generation within the battery during the discharge process.

The variation of cell potential, current density and temperature distribution of the simulated cell during the discharge was presented. The performance of the proposed systems has been verified with experimental results. The effect of electrical contact resistance between the current collectors and terminals of the cell has been studied by adding positive and negative tabs. The placement of tabs has a significant effect on the heat generation rate and distribution of the current density and electric potential inside the battery. The 3D model provides an efficient method to observe the detailed information of the ECT performance and temporal estimation of the LIBs over a wide range of temperature and C-rates, which are difficult to

obtain by the experimental method. To achieve the high-accuracy results quickly and at relatively lower computational costs than with default mesh settings, the swept meshing method applied to create the geometry. The analysis method established in this paper have the potential to be used to reduce the maximum temperature and maintain the temperature uniformity of the cells, especially in battery pack designs for EVs. The results revealed that the effect of tab placement should be considered in the design of LIBs. The model can be extended to investigate the effect of electrical contact resistance between the terminals and the tabs of the cell, current distribution and heat dissipation of a battery module or pack, which is important in EV and HEV battery design.

#### ***4.6 Acknowledgments***

This work was supported by the battery research laboratory at the University of Windsor. The authors would like to acknowledge CMC Microsystems for the provision of products and services that facilitated this research including CAD tools and design methodology.

#### ***4.7 Reference***

- [1] C. Daniel, Materials and processing for lithium-ion batteries, *Jom*, 2008, pp. 43-48.
- [2] T. Stuart, F. Fang, X. Wang, C. Ashtiani, A. Pesaran, A modular battery management system for HEVs, *SAE Technical Paper*, 2002.
- [3] S. Al-Hallaj, R. Kizilel, A. Lateef, R. Sabbah, M. Farid, J.R. Selman, Passive thermal management using phase change material (PCM) for EV and HEV Li-ion batteries, *Vehicle Power and Propulsion*, 2005 IEEE Conference, 2005, pp. 376-380.



- [4] S. Chen, C. Wan, Y. Wang, Thermal analysis of lithium-ion batteries, *Journal of Power Sources*, 140 (2005) 111-124.
- [5] G.G. Botte, V.R. Subramanian, R.E. White, Mathematical modeling of secondary lithium batteries, *Electrochimica Acta*, 45 (2000) 2595-2609.
- [6] D.H. Jeon, S.M. Baek, Thermal modeling of cylindrical lithium ion battery during discharge cycle, *Energy Conversion and Management*, 52 (2011) 2973-2981.
- [7] G.-H. Kim, A. Pesaran, R. Spotnitz, A three-dimensional thermal abuse model for lithium-ion cells, *Journal of Power Sources*, 170 (2007) 476-489.
- [8] K. Kumaresan, G. Sikha, R.E. White, Thermal model for a Li-ion cell, *Journal of the Electrochemical Society*, 155 (2008) A164-A171.
- [9] R. Zhao, J. Liu, J. Gu, The effects of electrode thickness on the electrochemical and thermal characteristics of lithium ion battery, *Applied Energy*, 139 (2015) 220-229.
- [10] L. Saw, Y. Ye, A. Tay, Electrochemical–thermal analysis of 18650 lithium iron phosphate cell, *Energy Conversion and Management*, 75 (2013) 162-174.
- [11] P. Taheri, A. Mansouri, M. Yazdanpour, M. Bahrami, Theoretical analysis of potential and current distributions in planar electrodes of lithium-ion batteries, *Electrochimica Acta*, 133 (2014) 197-208.
- [12] P. Taheri, A. Mansouri, M. Yazdanpour, M. Bahrami, Potential and Current Distributions in Planar Electrodes of Lithium-Ion Batteries, *Meeting Abstracts, Electrochemical Society*, 2014, pp. 397-397.
- [13] M. Yazdanpour, P. Taheri, A. Mansouri, M. Bahrami, A distributed analytical electro-thermal model for pouch-type lithium-ion batteries, *Journal of The Electrochemical Society*, 161 (2014) A1953-A1963.
- [14] V. Srinivasan, J. Newman, Discharge model for the lithium iron-phosphate electrode, *Journal of the Electrochemical Society*, 151 (2004) A1517-A1529.
- [15] S. Du, M. Jia, Y. Cheng, Y. Tang, H. Zhang, L. Ai, K. Zhang, Y. Lai, Study on the thermal behaviors of power lithium iron phosphate (LFP) aluminum-laminated battery with different tab configurations, *International Journal of Thermal Sciences*, 89 (2015) 327-336.
- [16] K. Somasundaram, E. Birgersson, A.S. Mujumdar, Thermal–electrochemical model for passive thermal management of a spiral-wound lithium-ion battery, *Journal of Power Sources*, 203 (2012) 84-96.

- [17] W. Gu, C.-Y. Wang, Thermal and electrochemical coupled modeling of a lithium-ion cell, *Proc.-Electrochem. Soc.*, 99 (2000) 748-762.
- [18] N. Sato, Thermal behavior analysis of lithium-ion batteries for electric and hybrid vehicles, *Journal of Power Sources*, 99 (2001) 70-77.
- [19] L. Rao, J. Newman, Heat-Generation Rate and General Energy Balance for Insertion Battery Systems, *Journal of the Electrochemical Society*, 144 (1997) 2697-2704.
- [20] M. Doyle, T.F. Fuller, J. Newman, Modeling of galvanostatic charge and discharge of the lithium/polymer/insertion cell, *Journal of the Electrochemical Society*, 140 (1993) 1526-1533.
- [21] M. Doyle, J. Newman, A.S. Gozdz, C.N. Schmutz, J.M. Tarascon, Comparison of modeling predictions with experimental data from plastic lithium ion cells, *Journal of the Electrochemical Society*, 143 (1996) 1890-1903.
- [22] H.-K. Kim, T.-Y. Seong, J.-H. Lim, W.I. Cho, Y.S. Yoon, Electrochemical and structural properties of radio frequency sputtered cobalt oxide electrodes for thin-film supercapacitors, *Journal of power sources*, 102 (2001) 167-171.
- [23] M. Joulié, R. Laucournet, E. Billy, Hydrometallurgical process for the recovery of high value metals from spent lithium nickel cobalt aluminum oxide based lithium-ion batteries, *Journal of Power Sources*, 247 (2014) 551-555.
- [24] S. Basu, R.S. Patil, S. Ramachandran, K.S. Hariharan, S.M. Kolake, T. Song, D. Oh, T. Yeo, S. Doo, Non-isothermal electrochemical model for lithium-ion cells with composite cathodes, *Journal of Power Sources*, 283 (2015) 132-150.
- [25] S. Basu, K.S. Hariharan, S.M. Kolake, T. Song, D.K. Sohn, T. Yeo, Coupled electrochemical thermal modelling of a novel Li-ion battery pack thermal management system, *Applied Energy*, 181 (2016) 1-13.
- [26] M. Guo, R.E. White, A distributed thermal model for a Li-ion electrode plate pair, *Journal of Power Sources*, 221 (2013) 334-344.
- [27] U.S. Kim, C.B. Shin, C.-S. Kim, Modeling for the scale-up of a lithium-ion polymer battery, *Journal of Power Sources*, 189 (2009) 841-846.
- [28] Nyman, M. Behm, G. Lindbergh, Electrochemical characterisation and modelling of the mass transport phenomena in LiPF<sub>6</sub>-EC-EMC electrolyte, *Electrochimica Acta*, 53 (2008) 6356-6365.

- [29] S. Mischie, L. Toma, Behavior of the Lead Acid Battery after the Rest Period, WSEAS Trans. on Power Systems, 3 (2008) 111-117.
- [30] F. Jiang, P. Peng, Y. Sun, Thermal analyses of LiFePO<sub>4</sub>/graphite battery discharge processes, Journal of Power Sources, 243 (2013) 181-194.
- [31] K.E. Thomas-Alyea, J. Newman, Electrochemical Systems, John Wiley & Sons, Inc., Hoboken, NJ, 2004.
- [32] W. Fang, O.J. Kwon, C.Y. Wang, Electrochemical–thermal modeling of automotive Li-ion batteries and experimental validation using a three-electrode cell, International journal of energy research, 34 (2010) 107-115.
- [33] D.R. Baker, M.W. Verbrugge, Temperature and Current Distribution in Thin-Film Batteries, Journal of the Electrochemical Society, 146 (1999) 2413-2424.
- [34] S.-C. Chen, Y.-Y. Wang, C.-C. Wan, Thermal analysis of spirally wound lithium batteries, Journal of the Electrochemical Society, 153 (2006) A637-A648.
- [35] M. Yazdanpour, P. Taheri, M. Bahrami, A computationally-effective thermal model for spirally wound nickel-metal hydride batteries, Journal of The Electrochemical Society, 161 (2014) A109-A117.
- [36] Y. Chen, J.W. Evans, Heat Transfer Phenomena in Lithium/Polymer-Electrolyte Batteries for Electric Vehicle Application, Journal of the Electrochemical Society, 140 (1993) 1833-1838.
- [37] P. Taheri, M. Bahrami, Temperature rise in prismatic polymer lithium-ion batteries: An analytic approach, SAE International Journal of Passenger Cars-Electronic and Electrical Systems, 5 (2012) 164-176.
- [38] G. Guo, B. Long, B. Cheng, S. Zhou, P. Xu, B. Cao, Three-dimensional thermal finite element modeling of lithium-ion battery in thermal abuse application, Journal of Power Sources, 195 (2010) 2393-2398.
- [39] W.F. Howard, R.M. Spotnitz, Theoretical evaluation of high-energy lithium metal phosphate cathode materials in Li-ion batteries, Journal of Power Sources, 165 (2007) 887-891.
- [40] D. Bernardi, E. Pawlikowski, J. Newman, A general energy balance for battery systems, Journal of the electrochemical society, 132 (1985) 5-12.

## CHAPTER 5

# MODELING AND EXPERIMENTAL ANALYSIS OF LITHIUM-ION BATTERY KEY PARAMETERS

*This work has been submitted to Electrochimica Acta - Journal – Elsevier, 2017*

---

### 5.1 Summary

An experimentally validated modeling technique has been developed to analyze the polarization, and corresponding internal resistance of an NCA/Graphite based lithium-ion cell. The model constitutes a theoretical basis for the discussion regarding the cell capacity, energy efficiency, internal resistance, rate capability, heat distribution, specific energy and power capability of a lithium-ion cell. Simulations using the actual parameters have demonstrated that the battery in its existing design is ohmically limited for high power applications. Some of the defined properties studied in this work may have a significant role in the design of battery management system for EVs and HEVs. The simulation results have shown the dependency of cell capacity, internal cell resistance, and the cell SOC on the temperature of operation. Therefore, it is essential to have a precise knowledge of the cell operating behavior in a wide range of SOC and temperature to predict cell energy and power delivery. The presented method provides the opportunity to find optimal cell operation requirements and parameters for cell design.

## 5.2 Introduction

The lithium-ion battery has been considered for powering high-end electronics applications in industries such as portable phones, camcorders, computers, medical devices, and for electrification of vehicles and back-ups for solar and wind energy sources. The LIBs used in the EVs and HEVs lose capacity and power with aging. LIBs are expected to supersede the nickel/metal-hydrate battery packs utilized in some of the existing hybrid electric vehicles due to their higher energy storage and power densities and lower self-discharge [48-50]. LIBs have a high energy and power density in comparison with other commercial secondary batteries such as nickel-metal hybrid and lead-acid batteries. The EV and HEV battery performances usually investigated in term of the power capability and the energy efficiency through applying high discharge and charge current that causes a significant increase in battery temperature.

In general, temperature affects several aspects of a battery performance including electrochemical reactions inside a battery, rates of charging and discharging, energy density and power capability, cycle life and shelf life, battery safety and reliability, and battery cycle cost. The main concerns of consumers are to extend the service life, safety, and reliability of the battery on board of an electric vehicle. Essentially, the heat generation in cells caused by exothermic reactions and exothermic heat generated by entropy change and chemical reactions [51]. Therefore, the key parameters to define the performance of lithium ion batteries are capacity, internal resistance, power capability, battery temperature, and self-discharge. The specific energy of a battery is determined via its capacity ( $Ah$ ) and voltage ( $V$ ) per unit weight ( $Wh/kg$ ), while the internal resistance restricts the specific power and available energy that is limited by the specified cell cut-off voltages.

In a system with the battery as the only power and energy source such as EVs and when cell operates in charge depleting mode in HEVs, the high power capability that requires high drain current is critical. Therefore, it is vital to improve the LIBs power capability, safety and lifetime at higher currents and temperatures [52-54].

The internal battery resistance analysis represents the battery voltage drop under the current load, hence the capability of the battery to obtain a reliable power strongly associated with the internal resistance. The LIBs require functioning within a specified voltage range for safety purposes and extended cycle life. The dynamic nature of the internal cell resistance is an essential parameter to measure performance, SOC, and state of health (SOH) of the battery.

The overall internal resistance of a battery is a function of ohmic resistances and polarization resistances. The ohmic resistance caused by electrode materials resistance, electrolytes resistance, separators resistance and contact resistances. The internal resistance is rising from an applied electric current through an ohmic resistance within the electrode or the electrolyte. Its effect on cell performance is important during the discharging process when the current flows from the anode to the cathode, and mass transport through the electrolyte [23]. The battery conditions such as SOC, the temperature, the current rate and eventually the previous cell history affect the cell resistance. The resistance caused by the kinetics of the electrochemical charge transfer at the electrode/electrolyte interface and resistance due to the mass transport across electrolyte and electrode materials are considered as the kinetic polarization resistance. Therefore, the internal cell resistance that contains the kinetic and ohmic polarization is in defining battery power. Therefore, the proper analysis of internal resistance is necessary for establishing battery management system.

The polarization refers to the deviation of electrode potential from its equilibrium states and depends on current density at the electrode/electrolyte interface. The electrode polarization may occur at the anode and cathode causing anodic and cathodic polarizations. In addition to the general ohmic polarization, there are two types of polarization: the kinetic or activation polarization, and the diffusional or mass transport polarization. Accordingly, to understand the battery performance, many analysis have been made from the perspective of electrochemical reaction mechanism and charging control algorithm. Regarding the influence of lowering the charging time of LIBs for their commercial purpose of fast charging for high power applications, cell component variables were studied to check their effects on charging time [24]. Between the variables in the study, cathode thickness held the greatest impact on the charging time of Lithium-ion cells. However, the lithium metal deposition on the anode has increased the self-discharge rate and reduced the safety aspects of lithium-ion cells. Jiuchun Jiang [55], proposed a polarization based charging boundary curve to improve charging speed and reduce polarization of the battery at the same time. The results indicated that the appropriate charging current values should consider the temperature rise, battery service life, and charge efficiency. Nyman [48] presented a method that described the physical and chemical processes to investigate how the polarization changed in a battery cell, and showed that the limits vary depending on how the cell is utilized. Though, using a thicker electrode thickness decreased the cell performance particularly for the high power application. The battery performance and cell polarization improved at the higher ionic conductivity of the electrolyte which effects on the mass transport within the electrolyte.

A battery is a complex system, and its behavior strongly depends on the nonlinear and time-dependent capacitive and ohmic performances of the cell components. Very few modeling studies have been carried out to investigate and optimize the performance of  $\text{LiNi}_{0.85}\text{Co}_{0.10}\text{Al}_{0.05}\text{O}_2$  (NCA) based electrode through studying the dynamic polarization and time-dependent internal resistance of the LIBs.

This work provided quantification of the electrodes polarization (voltage loss) and associated internal cell resistance. The results can be used to minimize the internal cell resistance and provide a high power capability.

The primary aim is to extensively investigate the temperature dependent charge/discharge rates, internal resistance values, and effect of these parameters on battery performance. The secondary aim is to improve the battery power capability by optimizing the polarization voltage drop induced by a discharge pulse current.

### ***5.3 Experimental***

In this work, we present a systematic study base on a prismatic LP6745135-10C-type lithium-ion battery NCA cathode and graphite anode with a total capacity of 4 Ah. The battery specs are listed in Table 5.1.

Figure 5.1 shows the geometry of the cell that is constructed from 40 unit cells, making 20 double sid coated plates connected in parallel and packed in a polymer laminated aluminum pouch case.



Table 5.1. Characteristics of the LP6745135-10C-type LIB.

Item	Cell
Nominal capacity	4Ah
Nominal voltage	3.7V
Standard charge current	0.2C
Max charge current	1C
Charge cut-off voltage	4.2V±0.05V
Max discharge current	10C
Discharge cut-off voltage	2.7V
Weight	91g
Dimension (mm)	6*42*127

The current from the external circuit flows into the cell tab, then flows into all the local regions of the battery generating reactions at the negative and the positive electrodes and lithium-ion migration through the electrolyte. All the electrode tabs of the same type are welded together to form the battery terminals. Each unit cell includes a layer of the positive current collector, positive electrode, a separator containing electrolyte, negative electrode and a negative current collector.

The simplified schematic layout of Lithium-ion cell is shaped to obtain the desired physical dimensions of the current collectors, electrodes, and separator, shown in Figure 5.1.b. Figure 5.2 displays the X-ray Diffraction (XRD) analysis of anode (-) and cathode (+) to indicate the materials used in the cell. The positive (+) and the negative (-) current collectors are made from aluminum foil and copper foil, respectively.

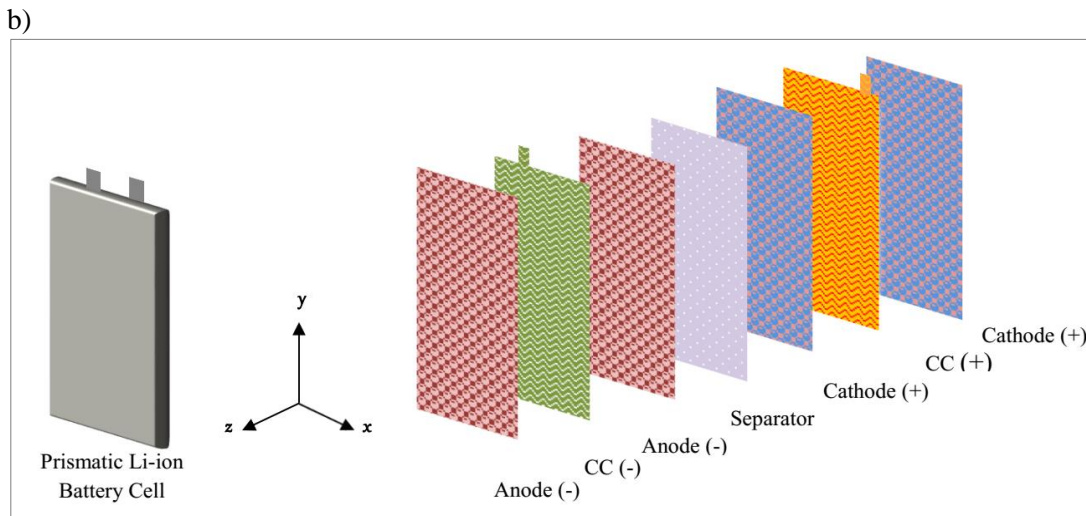


Figure 5.1. a) The stacked structure of the original experimental battery with the pouch case. The cell is constructed from 40 double side coated plates making 20 cells connected in Parallel. b) Simplified schematic layout of a prismatic cell.

The separator sheet which prevents physical or electronic contact between the anode and the cathode is a porous polypropylene polyethylene copolymer that contains liquid electrolyte formulated from 1M Lithium hexafluorophosphate (1M  $\text{LiPF}_6$ ) in a 50:50 mixture of ethylene carbonate and dimethyl carbonate (EC: DMC).

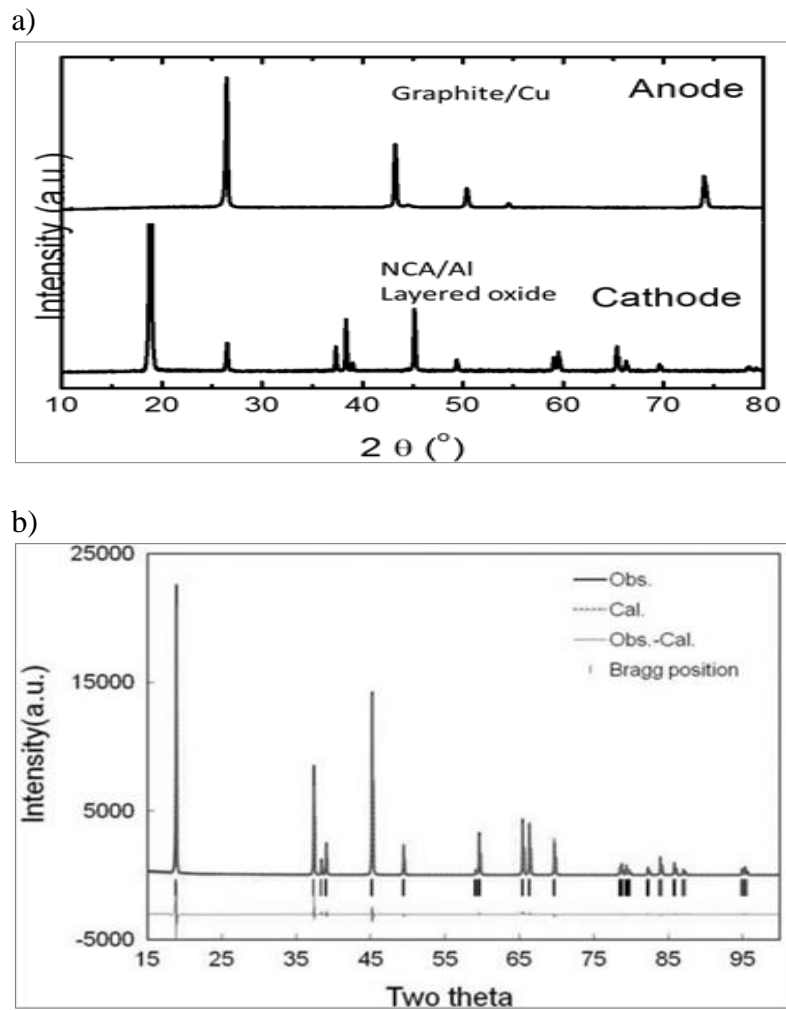


Figure 5.2. a) XRD analysis of anode and the cathode. b) XRD Reference for layered oxide cathode.

The commercial battery cycler (MACCOR) was used to measure voltage and capacity at various C-rates (applied constant currents). The cell temperature maintained within  $25 \pm 0.5^\circ\text{C}$  during the measurements using a temperature test chamber.

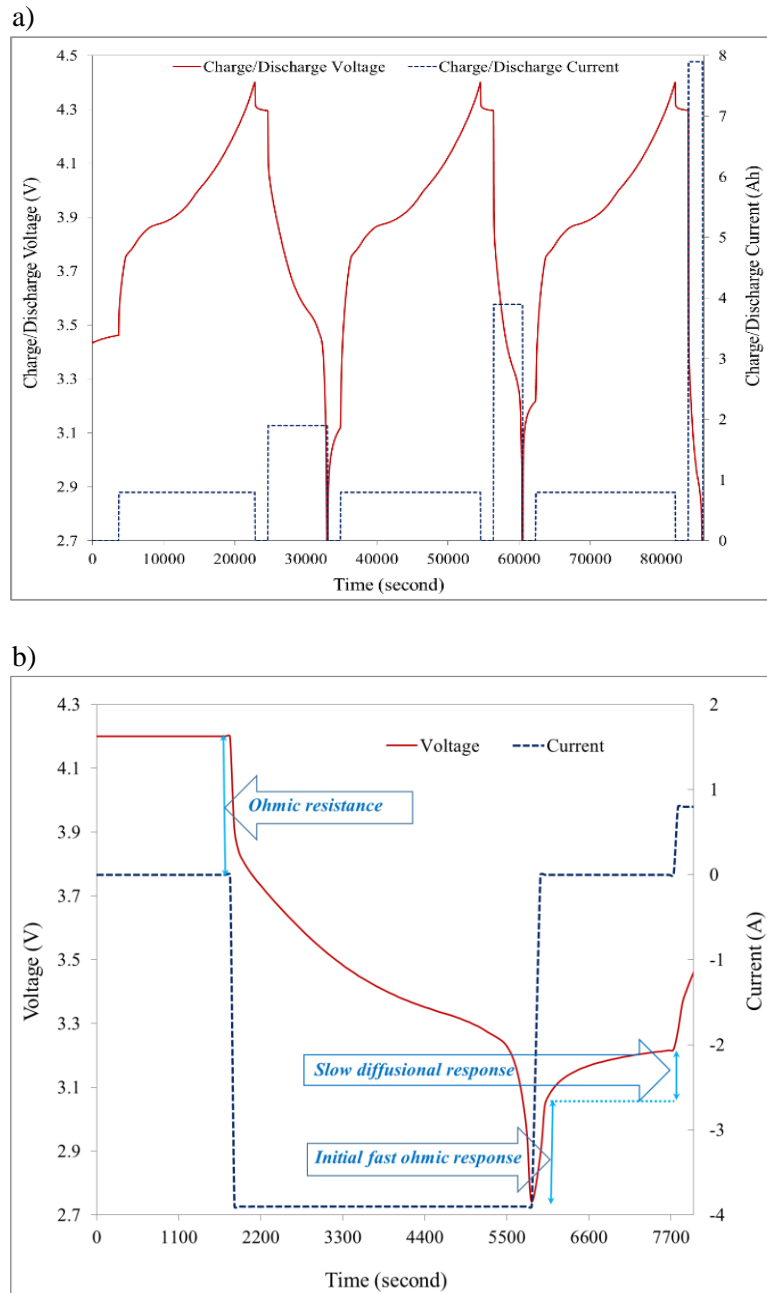


Figure 5.3. a) Current and voltage profiles versus time during charge and discharge containing a rest period of 30 minute at different C-rates. b) Characteristics of the cell voltage variation during discharge period and rest period.

To obtain cell performance as a function of temperature, and validate the results with numerical analysis, thermal images of the battery have been recorded using Infrared Camera Incorporation (ICI) P9000). Infrared (IR) images can provide real-time thermal images by converting the captured IR radiation from cell to surface temperature.

IR photography is a more accurate and flexible technique than installing many thermocouples on the battery surface for evaluating the thermal behavior of the battery. The cell has been charged at  $0.2C = 0.8Ah$  rate to reach the full charge state, and after a 30 minutes rest period the battery was discharged. All measurement at various rates were carried out from its fully charged state to the specified fully discharge state (60% SOC). The battery current and voltage profiles during charge and discharge process are shown in Figure 5.3.a. It is illustrated in Figure 5.3.b that at the beginning of the discharge period the voltage dropped faster due to electrical ohmic resistance. Later the voltage decreases more gradually due to slower diffusion of ions in the solid electrodes and liquid electrolyte. Additionally, the cell voltage variation during the rest period, marked with the initial fast ohmic response and slow diffusional response in Figure 5.3.b.

#### ***5.4 Model description***

The well-established pseudo- one dimensional forms the basis of the electrochemical model in this work. The geometry of the cell under investigation is given in Figure 5.4.a. The battery internal resistance can be evaluated accurately by applying a pulse current and measuring voltage changes. Figure 5.4.b shows the simplified electrical equivalent circuit

model of vehicle power battery [56]. The model describes the following battery's dynamic, open circuit voltage,  $V_{oc}$ , the battery internal ohmic resistance,  $R_{int}$ , and an RC-equivalent circuit with a capacitor,  $C_p$ , and a resistor,  $R_p$ , in the parallel connection that contributes to the cell capacitive and charge transfer resistance.

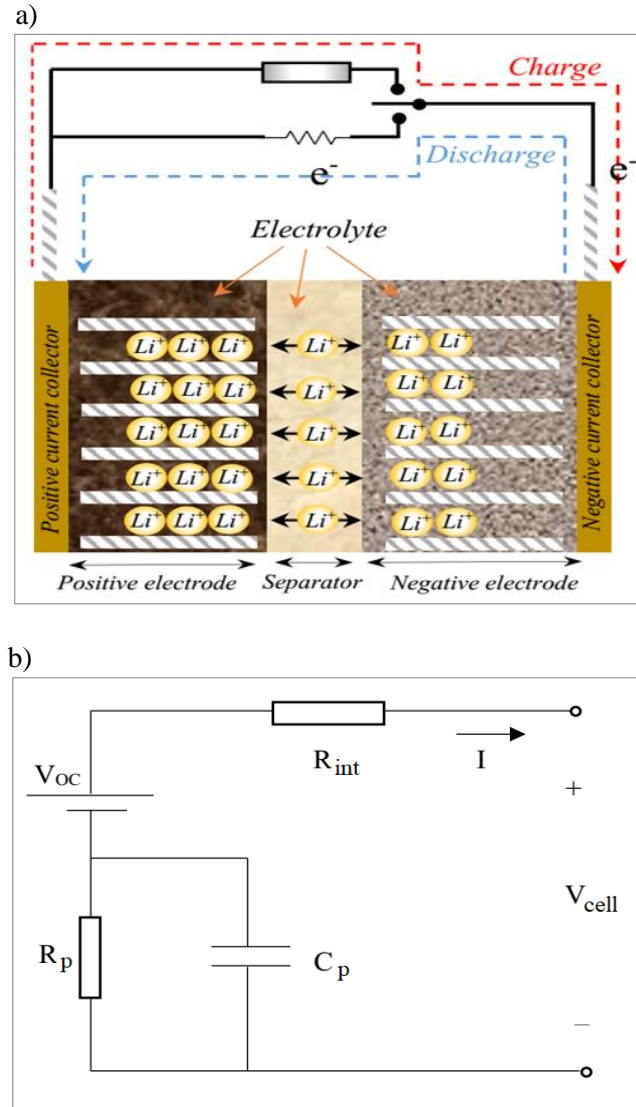


Figure 5.4. a) Schematic of a unit cell of the battery including positive and negative porous electrodes, a porous separator, and current collectors during charge and discharge process. b) The electrical equivalent circuit of a cell including open-circuit-voltage, cell ohmic resistance  $R_{int}$  and  $R_p$  and  $C_p$  of the RC-circuit.

The electrodes and separator layers are made in porous formats and contain a liquid electrolyte, to improve active materials utilization in the battery. The NCA, which is a promising cathode material with high energy and power densities, as well as good cycle has been used and artificial graphite is used as the negative electrode.

The battery design optimization is complex and requires significant time and experimental operation for a particular application. To speed up this process and provide predictive electrode performance, computer simulations are beneficial. Optimization of the LIB interface considers many physical battery properties like the thickness of electrodes and separator, porosity of electrodes and separator, active materials particle size, ionic conductivity and stability of electrolyte material, cut-off voltages during charge and discharge, and the applicable SOC window. The more features that can be controlled accurately, the more reliable available energy and power outputs, thermal behavior, cycle life, and battery safety can be estimated.

There are many types of battery cells, including energy cell and power cell. The energy cells provide more energy because of more active materials, denser and thicker electrode coating and usually with longer cell aspect ratio. The power cells may require thinner and more porous electrodes leading to a faster utilization of electrodes active materials. Therefore, to obtain maximum available energy and power outputs (known as P/E ratio), it is important to consider materials and design aspects of the electrodes. It allows using accurate modeling to optimize battery for high power-demanding applications such as electric vehicle [57]. In this work, the rate capability of the battery investigated in terms of polarization or internal cell resistance.

We have used an approach to include the SEI layer resistance effect in the simulations to get good agreement with the experimental data and optimize the cell performance. Then, to compensate the impact of various polarizations in the model, the optimization procedure has been considered to vary the design adjustable parameters. The variable parameters (particle size, porosity, and different stages of SOC) correlated to a process set to large or small values. The strategy is based on dividing the polarization rise due to activation of the electrochemical reaction, mass transport of species, and different film contact resistances.

### ***5.5 Mathematical modeling***

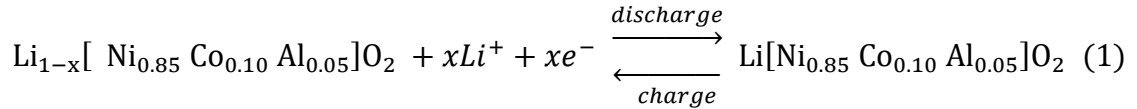
The battery performance during discharge affected by different design properties such as electrolyte volume fractions (porosity) and electrode material particle sizes, thermodynamic properties such as equilibrium potentials and lithium concentrations, transport properties such as lithium diffusivities in electrode materials and electrolyte, and kinetic properties such as intercalation reaction rate constants. The general model includes electronic current conduction in the electrodes, ionic charge transport in the pores of the electrodes and separator, material transport in the electrolyte to include the effects of lithium-ion concentration on ionic conductivity and concentration overpotential. Fick's Law governs the material transport within the spherical intercalating particles that form the electrodes, and the Butler-Volmer equation directs the charge transport in the electrode for the electrode kinetics.



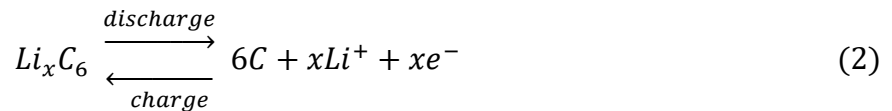
The charge and mass transport equations are used to describe the spatial and time-dependent variation of the potential and the lithium-ion concentration in the solid electrodes and the liquid electrolyte phases.

In this work, it is presumed that the lithium ion migrates through a film that prevents the transport of ions on the surface of the active particle in the porous electrodes to react electrochemically with the active material that causes an increase in resistance. This extra layer resembles the existence of the SEI layer on the electrodes. The consequence of insufficient contact between the electronically conducting diluent phase and the active material phase also increases overall cell internal resistance. Both of these effects are modeled as a single film resistance ( $R_{film}$ ) [48, 53, 58].

The electrochemical reactions during the discharge/charge in the cathode composite electrode [42] due to redox reactions on the transition metal sites can be expressed as,



and the discharge/charge reaction in the composite anode is given by, [42],



### 5.5.1 Electrochemical Kinetic at the interface

The local charge transfer current density,  $i_{loc}$ , in the electrode is defined by the Butler-Volmer kinetic expression given below [37]:

$$i_{loc} = i_0 \left( \exp\left(\frac{\alpha_a F \eta}{RT}\right) - \exp\left(\frac{-\alpha_c F \eta}{RT}\right) \right) \quad (3)$$

The exchange current density  $i_0$  and the magnitude of electrode potential polarization  $\eta$  that denotes the voltage loss during discharge of the cell at various rates are given as [37],

$$i_0 = F(k_c)^{\alpha_a}(k_a)^{\alpha_c}(c_{s,max} - c_s)^{\alpha_a}(c_s)^{\alpha_{ac}} \left(\frac{c_l}{c_{l,ref}}\right)^{\alpha_a} \quad (4)$$

$$\eta = \phi_s - \phi_l - \Delta\phi_{s, film} - V_{oc} \quad (5)$$

where  $\alpha_a$  and  $\alpha_c$  are the anodic and cathodic charge transfer coefficients,  $F$  is the Faraday's constant,  $k_c$  and  $k_a$  are cathodic and anodic rate constants respectively,  $c_{s,max}$  is the maximum lithium concentration at the in the solid phase,  $c_s$  is the concentration of lithium in the active material particle,  $c_l$  is the lithium ion concentration in the liquid electrolyte phase,  $c_{l,ref}$  is the electrolyte reference concentration on the surface of the active particles before application of current load,  $\phi_s$  is the solid phase potential,  $\phi_l$  is the electrolyte phase potential.

### 5.5.2 Charge conservation

The charge conservation in the positive and negative electrodes expressed as:

$$\nabla i_s + \nabla i_l = 0 \quad (6)$$

$$\nabla i_s = -i_{v,total} \quad (7)$$

$$\nabla i_l = i_{v,total} \quad (8)$$

where  $i_s$  denotes the electrical current density in the solid phase, and  $i_l$  refers the ionic current density in the electrolyte phase. The total electrode reaction current density,  $i_{v,total}$ , is a summation of the electrode reaction current density  $i_{v,m}$  and double layer current source,  $i_{v,dl}$ , given by the following equations:

$$i_{v,total} = \sum_m i_{v,m} + i_{v,dl} \quad (9)$$

$$i_{v,m} = a_v i_{loc} \quad (10)$$

$$i_{v,dl} = a_{v,dl} i_{dl} \quad (11)$$

where  $a_v$  is the active specific surface,  $a_v = \frac{3\varepsilon_s}{r_p}$ ;  $\varepsilon_s$  is the electrode volume fraction, and  $r_p$  is the particle size,  $i_{dl}$  is the double layer current density,  $i_{dl} = i\omega(\phi_s - \phi_l - \Delta\phi_{s,filim})C_{dl}$ ;  $\omega$  is the frequency,  $\Delta\phi_{s,filim}$  is the solid phase film potential,  $\Delta\phi_{s,filim} = R_{filim}i_{total}$ ;  $C_{dl}$  is the electrical double layer capacitance, and  $a_{v,dl}$  is the double layer area

where the total interface current density  $i_{total}$  is the summation of ,

$$i_{total} = \sum_m i_{loc,m} + i_{dl} \quad (12)$$

### 5.5.3 Electron transport in the solid phase and lithium ion transport in the electrolyte phase

The total interface current transferred between the solid electrode particles and the electrolyte solution for the anode and the cathode is given by the sum of the local charge transfer current and electrical double layer current. The transport of electrons in the solid phase is defined by equation (13). The transport of lithium ions in the liquid phase is expressed in equation (14).

$$i_s = -\sigma_s^{eff} \nabla \phi_s \quad (13)$$

$$i_l = -\sigma_l^{eff} \nabla \phi_l + \frac{2RT\sigma_l^{eff}}{F} \left(1 + \frac{\partial \ln f_{\pm}}{\partial \ln c_l}\right) (1 - t_+) \nabla (\ln c_l) \quad (14)$$

where  $\sigma_s^{eff}$  is the effective conductivities of the solid phase,  $\sigma_s^{eff} = \sigma_s \varepsilon_s^\gamma$ ,  $\sigma_s$  is electrical conductivity, and the Bruggeman coefficient  $\gamma$  is set to 1.5 to calculate the tortuosity effect in the pores electrodes and separator. The  $\sigma_l^{eff}$  defines the effective ionic conductivity of the electrolyte phase,  $\sigma_l^{eff} = \varepsilon_l^\gamma \sigma_l$ ;  $\sigma_l$  is the electrolyte conductivity, the average molar activity coefficient is  $f_{\pm}$ ,  $t_+$  is the transference number of lithium ions.  $R$  and  $T$  are universal gas constant and temperature of the electrolyte respectively [36, 43].

### 5.5.4 Mass conservation

The lithium species conservation in the spherical active material particle in solid electrode phase is described as:

$$\frac{\partial c_s}{\partial t} + \frac{1}{r_p^2} \frac{\partial}{\partial r_p} \left( -r^2 D_s \frac{\partial c_s}{\partial r_p} \right) = 0 \quad (15)$$

where  $D_s$  represent the diffusion coefficient of lithium in the solid phase and  $t$  is the time. The mass conservation in the electrolyte phase can be formulated by the Fick's second law:

$$N_l = -D_{l,eff} \nabla c_l + \frac{i_l t_+}{F} \quad (16)$$

where  $N_l$  the molar is the flux of lithium ions, and  $-D_{l,eff}$  is the effective diffusion coefficient of lithium ions in the electrolyte.

### 5.5.5 Energy balance

In this model, the heat generation due to the electrochemical reaction is combined with the energy equation as a source term. The summation of the produced heat in every two electrodes, separator, and current collectors is the total heat generation in the battery. The three heat sources are the reaction heat generation  $Q_{rea}$ , polarization heat generation  $Q_{pol}$ , and ohmic heat generation  $Q_{ohm}$ . Thus, it is essential to have a strong coupling between the electrochemical and thermal models of the battery. The energy balance in the lithium ion battery is given by [36, 43]:

$$\rho C_p \frac{\partial T}{\partial t} + \nabla \cdot (-k \nabla T) = Q_{rea} + Q_{pol} + Q_{ohm} \quad (17)$$

where  $\rho$ ,  $C_p$  and  $k$  are the local density, heat capacity at constant pressure and thermal conductivity of the battery material, respectively.

The reaction heat generation caused by reversible entropy change can be defined as [36, 43]:

$$Q_{rea} = a_v i_{loc} T \frac{\nabla V_{oc}}{\partial T} \quad (18)$$

The irreversible electrochemical reaction dissipates as polarization heat and is described by the following equation:

$$Q_{pol} = a_v i_{loc} \eta \quad (19)$$

The heat generation induced by ohmic effect is constituted of electrical heat generation in the solid phase and ionic heat generation in the electrolyte phase as:

$$Q_{ohm} = -i_s \nabla \phi_s - i_l \nabla \phi_l \quad (20)$$

It is crucial to develop electrode materials with higher capacity and rate capability, to produce high power LIBs.

Essentially when discharging the battery under a constant current, the specific energy ( $E$ ) is a measure of work per unit weight, and specific power  $P$  is the rate at which the work is done. In other words, power tells us how quickly can access the energy. The specific energy and power can be calculated as:

$$E = \frac{1}{M} \int_0^t (i_{total} \cdot V_{cell}) dt \quad (21)$$

$$P = \frac{E}{t_d} \quad (22)$$

where the mass  $M$  of the cell is in unit of kg .The energy efficiency  $\eta_e$  of the battery under charging-discharging is calculated as the ratio of energy output  $W_{out}$  over energy input  $W_{in}$  [59]:

$$\eta_e = \frac{W_{out}}{W_{in}} = \frac{\int_{t_{out,1}}^{t_{out,2}} (i_{total} \cdot V_{cell}) dt}{\int_{t_{in,1}}^{t_{in,2}} (i_{total} \cdot V_{cell}) dt} \quad (23)$$

The energy efficiency of the battery during the charge/discharge processes should be significantly less than 100% due to the various polarizations.

### 5.5.6 Estimation of Battery State of Charge (SOC)

The accuracy of the Coulomb counting method is influenced by the temperature, battery history, discharge current, and cycle life [60]. To estimate the SOC of the battery the Coulomb counting method is usually used that integrates the measured discharging current of the battery over time. The SOC estimation using the Coulomb counting is based on the average concentration of the lithium ion in the particle that excludes the impact of the polarizations, and the concentration gradient from the surface to the bulk of sample is also ignored.

Accordingly, the SOC by the Coulomb counting based on average concentration and the SOC at load condition in each electrode are calculated by the following equations respectively:

$$SOC_c = \frac{\int_{\Omega_{electrode}} c_{s,avg} d\Omega}{\int_{\Omega_{electrode}} c_{s,max} d\Omega} \quad (24)$$

$$SOC_l = \frac{\int_{\Omega_{electrode}} c_{s,surf} d\Omega}{\int_{\Omega_{electrode}} c_{s,max} d\Omega} \quad (25)$$

where  $c_{s,avg}$  is the average species concentration in electrodes, and  $c_{s,surf}$  is the surface species concentration.

Moreover, the SOC of the cell can be defined by either Coulomb counting method or a method that can include the effect of current load as follows,

$$SOC_{cell} = \frac{\int_{\Omega_{neg}} c_{s,avg,cycl} F \varepsilon_s d\Omega}{\int_{\Omega_{neg}} c_{s,avg,cycl} F \varepsilon_s d\Omega + \int_{\Omega_{pos}} c_{s,avg,cycl} F \varepsilon_s d\Omega} \quad (26)$$

where  $c_{s,avg,cycl}$  is the inserted average cyclable lithium concentration in the electrode particles which is defined as:

$$c_{s,avg,cycl} = c_{s,avg,electrode} - SOC_{min} c_{s,max} \quad (27)$$

The Cell SOC, at load, is computed as:

$$SOC_{cell,l} = \frac{\int_{\Omega_{neg}} c_{s,surf,cycl} F \varepsilon_s d\Omega}{\int_{\Omega_{neg}} c_{s,surf,cycl} F \varepsilon_s d\Omega + \int_{\Omega_{pos}} c_{s,surf,cycl} F \varepsilon_s d\Omega} \quad (28)$$

where  $c_{s,surf,cycl}$  is the inserted cyclable lithium concentration at the surface of the electrode particles which is defined as:

$$c_{s,surf,cycl} = c_{s,surf} - SOC_{min} c_{s,max} \quad (29)$$

Additionally, the cell voltage ( $V_{cell}$ ) is obtained from the local potential in the solid phase and the electrolyte phase, and the potential of each electrode ( $V$ ) under load is expressed as,

$$V_{cell} = \phi_s|_{cc\ pos} \quad (30)$$

$$V = \phi_s|_{cc} - \phi_L|_{sep} \quad (31)$$

where the  $cc$  means the current collector boundary and  $sep$  indicates the separator boundary.



The total polarization ( $\Delta V$ ) is calculated as the difference between the cell voltage under load and open-circuit cell voltage obtained from Coulomb counting method. The SOC are furthermore used to compute the Coulomb or at load open-circuit potential of each electrode and the corresponding open-circuit cell voltages.

$$\Delta V = V_{cell} - V_{oc} (SOC) \quad (32)$$

The internal battery resistance can be measured using any one of the three available methods; conductance, impedance, or resistance measurements. The internal resistance  $R_{int}$  is calculated from Ohm's law as follows,

$$R_{int} = \frac{-\Delta V(SOC)}{i_{total}} \Big|_{t=end\ of\ discharge} \quad (33)$$

## 5.6 Numerical method

The COMSOL Multiphysics 5.2 has been used to solve the equations using the Finite Elements Method (FEM). The model parameters are provided in Table 5.2.

The materials are accessible from the Batteries and Fuel Cells Material Library, and mostly default settings are selected. The Lithium-Ion Battery module is connecting accounts for electronic conduction in the electrodes, ionic charge transport in the electrodes and electrolyte/separator, material transport in the electrolyte. It is providing the foundation of the impacts of concentration on ionic conductivity and concentration overpotential, material transport inside the spherical particles that form the electrodes, and Butler-Volmer electrode

kinetics using experimentally measured equilibrium potential. The Ohm's law was utilized to explain the charge transport in the electrodes, while concentrated electrolyte theory applied for a quiescent aprotic (1:2) electrolyte to express charge and mass transport in the electrolyte phase. An extra dimension involved in the porous electrode domains to explain the transport of solid lithium in the solid electrode phase using Fick's law. The Initial Cell Charge Distribution global node used to define the initial cell voltage or cell SOC of a battery cell.

Table 5.2. Model parameter in different regions.

Parameters	Cu (CC)	Anode	Separator	Cathode	Al (CC)
Thickness, $L$ ( $\mu m$ )	16	48	26	46	23
Density, $\rho$ ( $kg.m^{-3}$ )	8900	2660	492	4770	2700
Specific heat capacity, $c_p$ ( $J.kg^{-1}.K^{-1}$ )	385	1437.4	1978	1172	903
Thermal conductivity, $K$ ( $W.m^{-1}.K^{-1}$ )	398	1.04	0.334	1.85	238
Electrolyte volume fraction in solid, $\epsilon_s$		0.3		0.2	
Electrolyte volume fraction in electrolyte, $\epsilon_l$			0.4		
Maximum Li concentration in solid, $c_{s,max}$ ( $mol.m^{-3}$ )		28688.7		20950	
Initial electrolyte concentration, $cl$ ( $mol.m^{-3}$ )		1000	1000	1000	
Solid phase electronic conductivity, $\sigma$ ( $S.m^{-1}$ )	6.0E7	2.0	0	0.01	3.8E7
Bruggeman exponent		1.5	1.5	1.5	
Anodic/Cathodic transfer coefficient, $a_a, a_c$		0.5		0.5	
Convective heat transfer coefficient, $h$ ( $W.m^{-2}.K^{-1}$ )			1e1.75		
Faraday's constant, $F$ ( $C.mol^{-1}$ )			96487		

To determine the SOC of the electrodes, both Coulomb and at load described in the Lithium-Ion Battery interface. The coulomb in contrast to at load excludes the impact of any polarization in the battery. An Event interface was also utilized to define the operation of the cell within the upper and lower cut-off voltages. The Heat Transfer in solids interfaces were used to model heat transfer in solids by conduction, convection, and radiation. A study node

containing a Parametric Sweep study, a current initialization step and the time-dependent step were applied to hold all the nodes which describe how to solve the model. The parametric sweep could find the solution to a sequence of the stationary or time-dependent problem that arises when you vary some parameters of interest include multiple independent parameters directly for a full multi-parameter sweep. At each time step, two segregated steps considered, the temperature distribution achieved by holding the electrochemical variables constant, and then the results of temperatures at each mesh node utilized to renew the local electrochemical and thermal parameters in the solver. The local parameters of each mesh node used to solve the governing equations. The process repeated at each node till reaching the convergence. The computations executed on a workstation of 64-bit Intel® Xeon® Processor 3.40E GHz including 32GB random access memory.

### ***5.7 Results and discussion***

A capacity test with different currents under a constant temperature of 25 °C is conducted at various low and high C-rates (0.2C, 0.5C, 1C, 2C, 3C, and 4C). The cell is fully discharged at constant current rates of 0.2C, 0.5C, 1C, 2C, 3C and 4C until the voltage reaches the bottom cut-off voltage of 2.7 V. The available capacity of the cell is the number of ampere-hours that can be drawn from the battery that is a function of the current and temperature. Therefore, current and temperature values must be specified in the capacity definition. In Figure 5.5.a the cell voltage (V) is presented as a function of capacity (Ah) for discharge at different rates.

The thin solid lines are displaying the simulation results, and the thicker connected markers are showing the experimental data. The measured data shows the maximum capacity of 4.16 Ah at 0.2C discharge rate and the minimum capacity of 3.13 Ah reported at 4C discharge rate within the voltage limits of 4.2 – 2.7 volts. As the usable capacity of the battery depends on the current discharge rate, consequently the higher the discharge current, the lower is the usable capacity that agrees with the literature [41]. It is evident that the performance is limited by the polarization of the battery cell due to nonuniform current and concentration distributions in the porous electrodes. Simulations indicate that the battery in its present design is power limited.

In the development of the model to fit the experimental data satisfactory, the influence of several parameters was verified and compared to the experimental results to show the importance of each parameter.

For example, the value of diffusion coefficient of lithium in carbon considered as a first variable to be a function of initial temperature and the time dependent heat generation or a constant value in the cell at different rates. In this case, the simulated cell voltage, seen in Figure 5.5.a showed no significant effect of the variable diffusion coefficient value on the polarization of the cell for the lithium diffusion in the negative electrode. It is revealed that the cell is not limited to the diffusion of lithium in the negative plate. In the case of constant value diffusion coefficient at higher rates, the cut-of voltage occurred before the time that diffusion limitation manifested as reported in the literature [37] too.

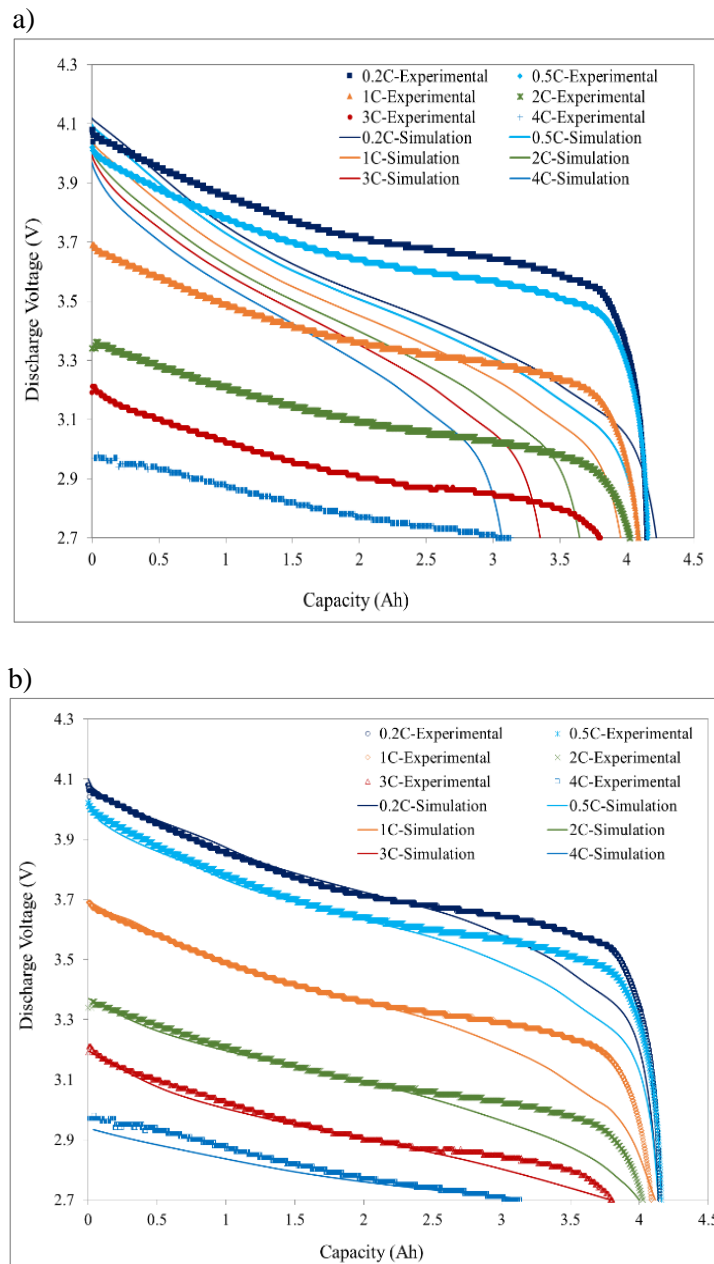


Figure 5.5. Comparison of simulation and experimental measured Cell voltage at various rates. The thin solid lines are displaying the simulation results, and the thicker connected markers are showing the experimental data; a) without film resistance, and b) with film resistance.

Next, we have evaluated the impact of lithium concentration of active material on the local charge transfer current density, by modifying the electrodes expression type from lithium

insertion to the concentration dependent kinetic transport properties. The reduced species expression  $C_R$  and oxidized species expression  $C_O$  has been added to the Butler-Volmer equation (3) as follow:

$$i_{loc} = i_0 C_R \left( \exp\left(\frac{\alpha_a F \eta}{RT}\right) - C_O \exp\left(\frac{-\alpha_c F \eta}{RT}\right) \right) \quad (34)$$

The simulation showed limited but not significant concentration-dependent effect on the polarization of the cell due to local concentration change in the pore of electrodes. Thus lithium insertion was described with the constant transport properties in the model. Therefore, an additional internal resistance in the cells, beyond that initially predicted by the model, could be described using either a contact resistance between cell layers or a film resistance of the electrode particles. An adjustable parameter must be applied in simulation to achieve a good agreement with the measured data. We found the best fit for the experimental results includes adding a film resistance of  $1000 \text{ } \Omega \cdot \text{cm}^2$  on the negative electrode surface. The simulation results using an additional film resistance presented in Figure 5.5.b displays the capacity utilization decreases considerably with increased load that is agreed well with the experimental data. There exists small deviation close to the end of the discharge process, which might be owing to the rise of the internal resistance at the end of the discharging period. This analysis showed the effect of SEI layers formed on electrodes in rate limitation of the cell performances.

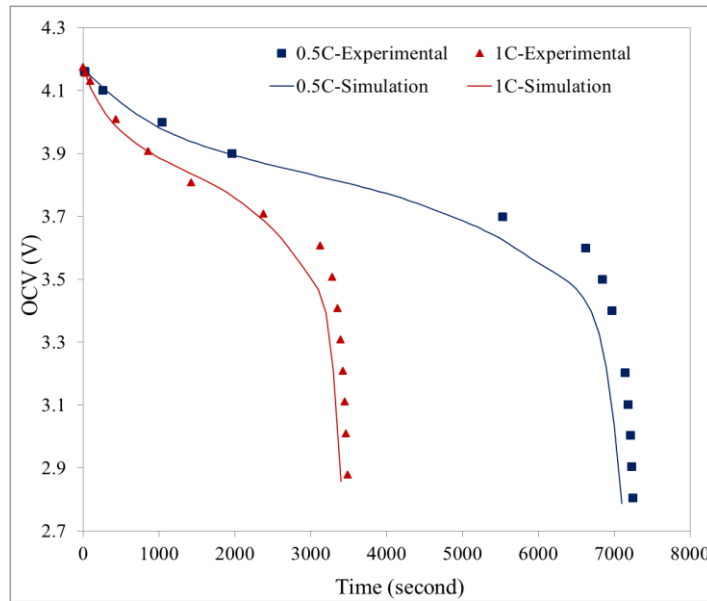


Figure 5.6. Comparison of measured OCV against time with simulation results at 0.5C and 1C rates during the discharge process.

The potential difference between the positive electrode and the negative electrode of a battery cell is its OCV when no external electric current flows and the electrode potentials are at equilibrium. The battery potential is governed by the OCV that develops as part of an electrochemical reaction, the overvoltage caused by lithium concentration polarization and charge transfer polarization, and the voltage drop caused by internal ohmic resistance. The OCV of LIBs has a significant effect in battery models that are used in BMS for automotive application. It varies non-linearly during the discharge period. The OCV comparison of simulation results at 0.5C and 1C rates with the experimental data are given in Figure 5.6. The part of the polarization that arises due to a particular process is calculated directly from the potential and concentration profiles in the cell. The sum of all contributions from different cell components is therefore equal to the total polarization of the cell reported in Figure 5.7.a. An

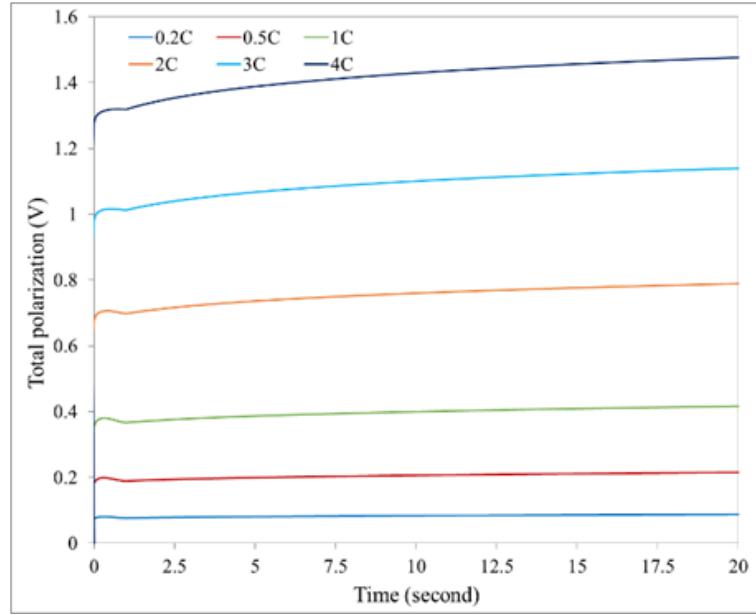
apparent increase in the polarization observed with raising the load. Subsequently, the internal resistance is the determining factor for power, energy efficiency and heat generation in LIBs. Therefore, the knowledge of this value is essential for designing the battery and thermal management systems for automotive applications. The calculated internal resistance of the cell against the capacity at different current rates presented in Figure 5.7.b. In fact, the temperature is a critical factor to be taken into account for internal resistance calculation, since the resistance of the electrolyte component is highly sensitive to the temperature variation. Hence we took special attentions on the temperature measurement to investigate the temporal temperature performance of the cell at variable current rates. The heat generation factors are decomposed into three elements, namely, reaction heat value, polarization heat value, and Joule heat value, which varies according to the variations in current and temperature [17].

Figure 5.7.c shows the average measured and simulated temperature rise on the cell surface at different discharge rates in respect to the battery capacity. To maintain the temperature rise within the desired operating temperature range (less than 45°C) [61], a small convective heat transfer coefficient,  $h=5 \text{ Wm}^{-2}\text{K}^{-1}$ , was applied to the surfaces and boundaries of the battery. It observed that the average temperature of the cell grew slowly with the SOC and sharply toward the end of the discharging period at each rate. The reason is a significant polarization close to the end of the discharge process.

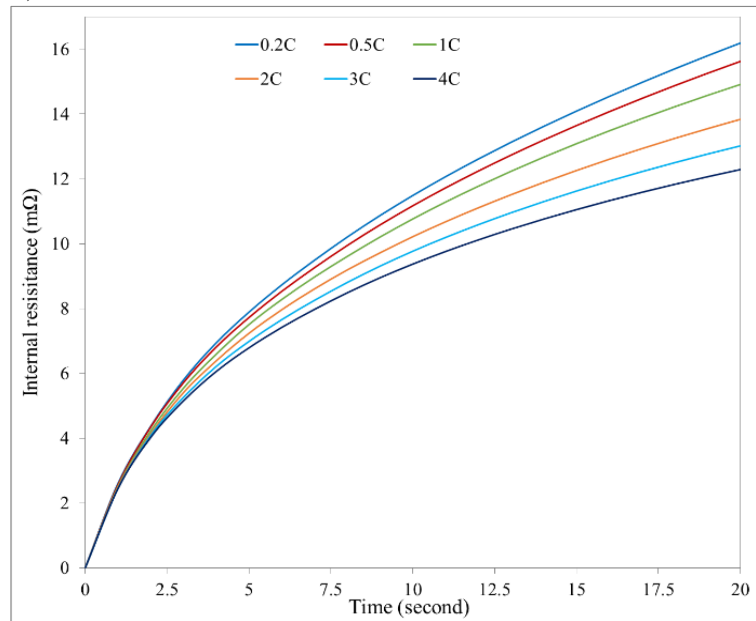
As expected, a significant heat generation occurred at 4C-rate as the temperature has a clear correlation with the discharge current and the total polarization. The voltage drop is not constant and changes during a discharge pulse. In the first moment after applying the current pulse, the voltage drops immediately over the pure ohmic resistance of the battery.



a)



b)



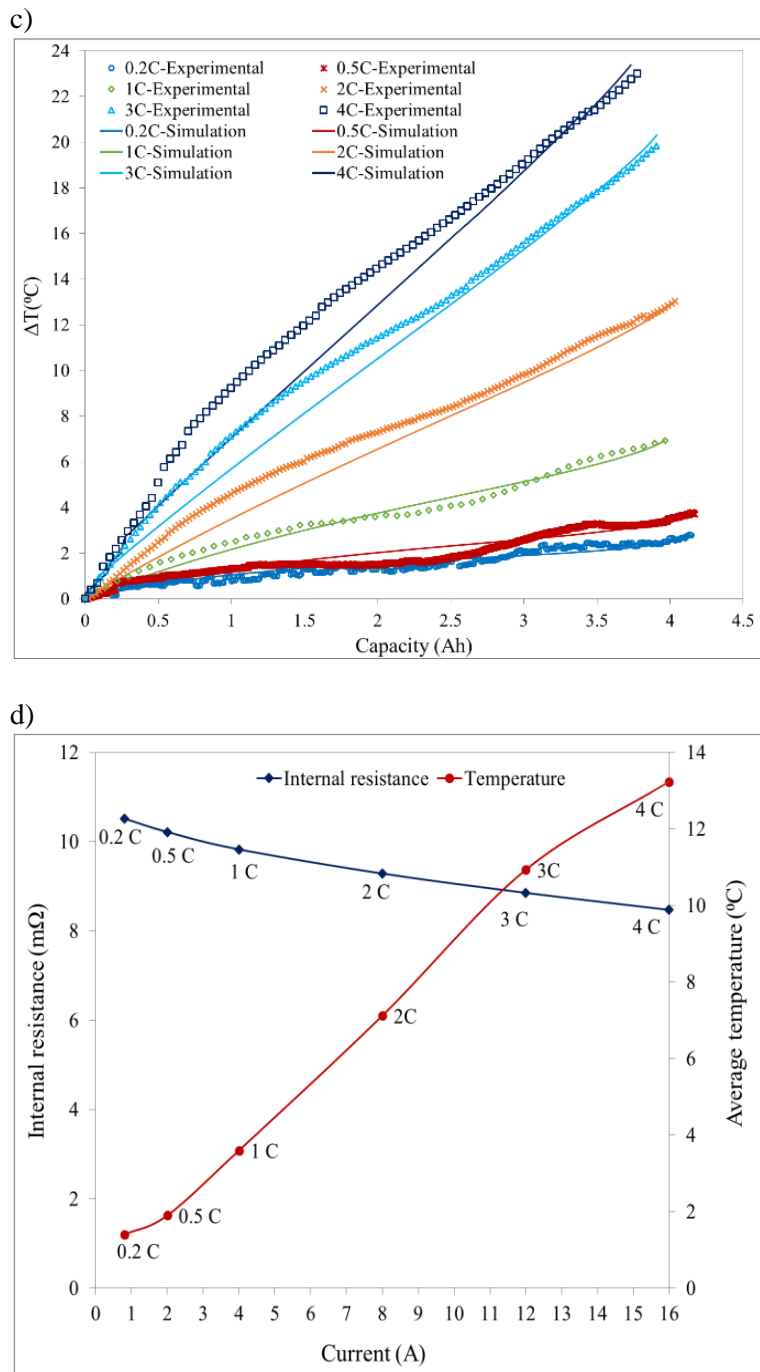
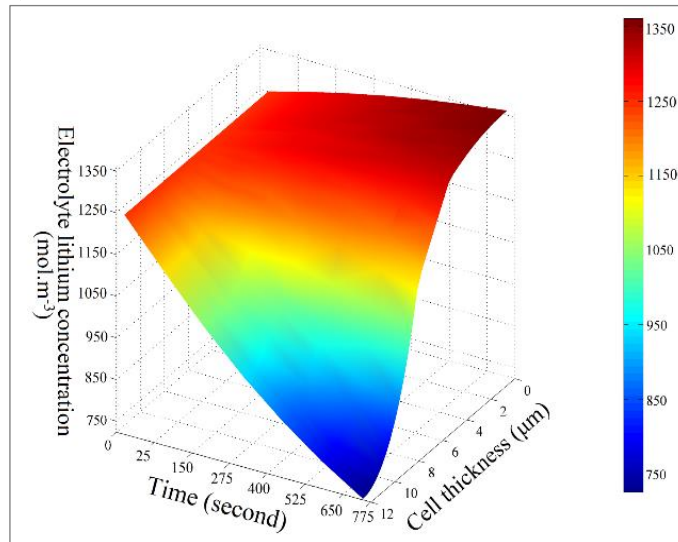


Figure 5.7. a) Estimated total polarization (voltage difference) against time at different current rates. b) Calculated changing the trend of internal resistance at various current rates. c) Comparison of the experimental and simulated average cell temperature during different discharge rates. d) Effect of current rate on internal resistance and mean temperature evolution.

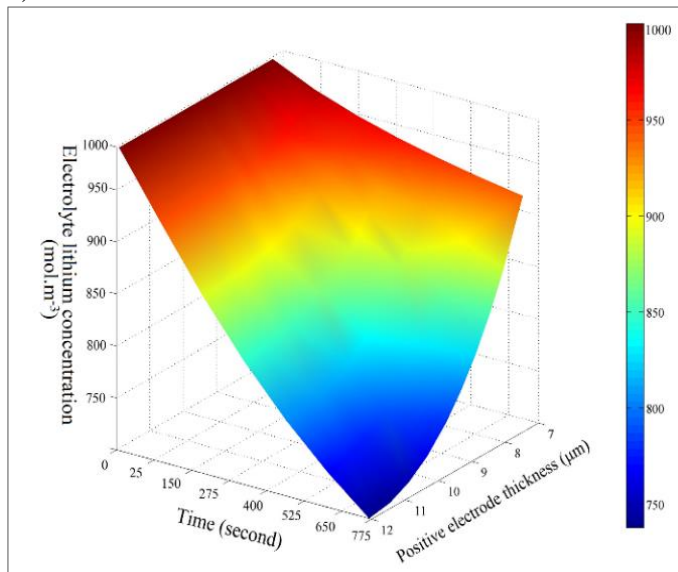
Accordingly, increasing the internal resistance causes lower battery discharge voltage, short discharge time, and have a direct impact on the battery power and energy characteristics. The heat flow initiated from the electrodes towards the internal battery structure due to the generated heat at the electrode–collector interface which can lead to a considerable temperature rise in the cell. Consequently, increasing the temperature rises the mass transport of solid and liquid phases which result in lower ohmic and mass transfer loss in the cell. The numerical simulation results are in excellent consistency with the data obtained from the experiments. However, there is some deviation in measured temperature curves at the middle of the discharges at high C-rates. It may be affected by the thermal resistance of the additives applied in the commercial batteries, including the resistance within the casing and the plastic shrink wrap, which is not considered in this research. Figure 5.7.d plotted the variation of internal resistance as a function of both temperature and current value through the discharging process. It is observed the internal resistance increased at the lower temperature and decreased at the higher temperature in the plug-in hybrid battery during winter and summer season [50].

The lower electrode kinetic reactions considerably increased the internal resistance of the cell at low temperatures resulting in a poor performance [23]. Therefore, the internal resistance results from the flow of the current in the resistive electrolyte and the potential of the anode and cathode are varied if the resistivity of the electrolyte is high. Thus, increasing current and temperature increase the total polarization value and reduce the internal resistance value of the cell.

a)



b)



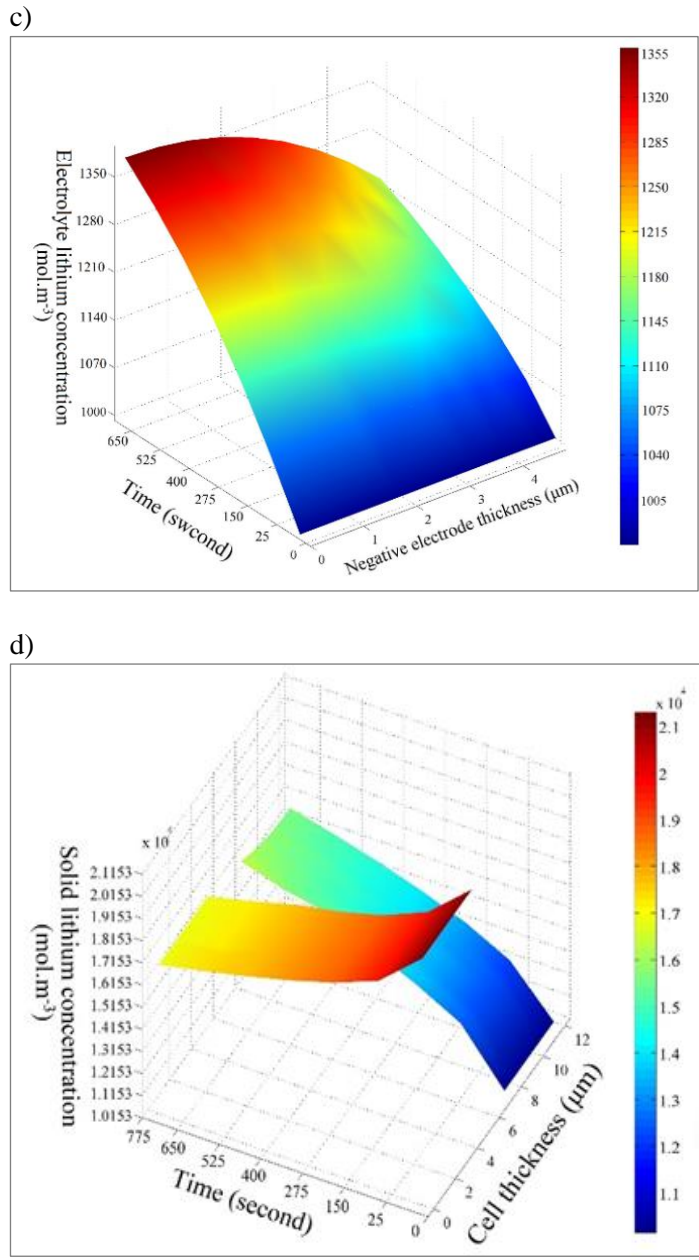


Figure 5.8. Electrolyte lithium concentration profile at 4C discharge rate: a) across the cell, b) at the positive electrode, c) at the negative electrode. c) Solid lithium concentration across the cell at 4C discharge rate.

One unique strength of this model is its capability to predict the lithium concentration distribution in all cell components during the battery operation. Lithium-ion concentration

profile in cell components is also a function of C-rate, which creates the ohmic heat generation in an electrolyte. Therefore, the ohmic heat generation is induced by the gradient of the lithium ion concentration, resulting in growth in internal ionic resistance [16]. The impact of the polarized ion concentration identified by considering the difference between the initial electrolyte potential and the potential at the end of discharge step. Hence, Figure 5.8.a. depicted the distribution of electrolyte concentration at 4C, for further investigating of the steep voltage decrease at the beginning of the discharge. Observably, due to de-intercalation, the Li-ion concentration at the beginning and end of discharge process are higher in the negative electrode than the positive electrode as presented in Figure 5.8.b-c. Furthermore, the surface concentration changes cause the variation of the equilibrium voltage which forms a lower reaction overpotential and a reduction in the local current density. It results in a significant polarization in the battery at higher discharge rates. The lithium concentration distribution in solid particles of the entire cell during the discharge plotted into Figure 5.8.d. The variation along the width of the cell occurs due to the non-uniform current distribution, which is induced mainly by the weak electrolyte conductivity (due to low porosity) but further via the concentration polarization.

It is necessary to investigate the required power and energy density of the cell to satisfy the requirement of BMS for EVs.

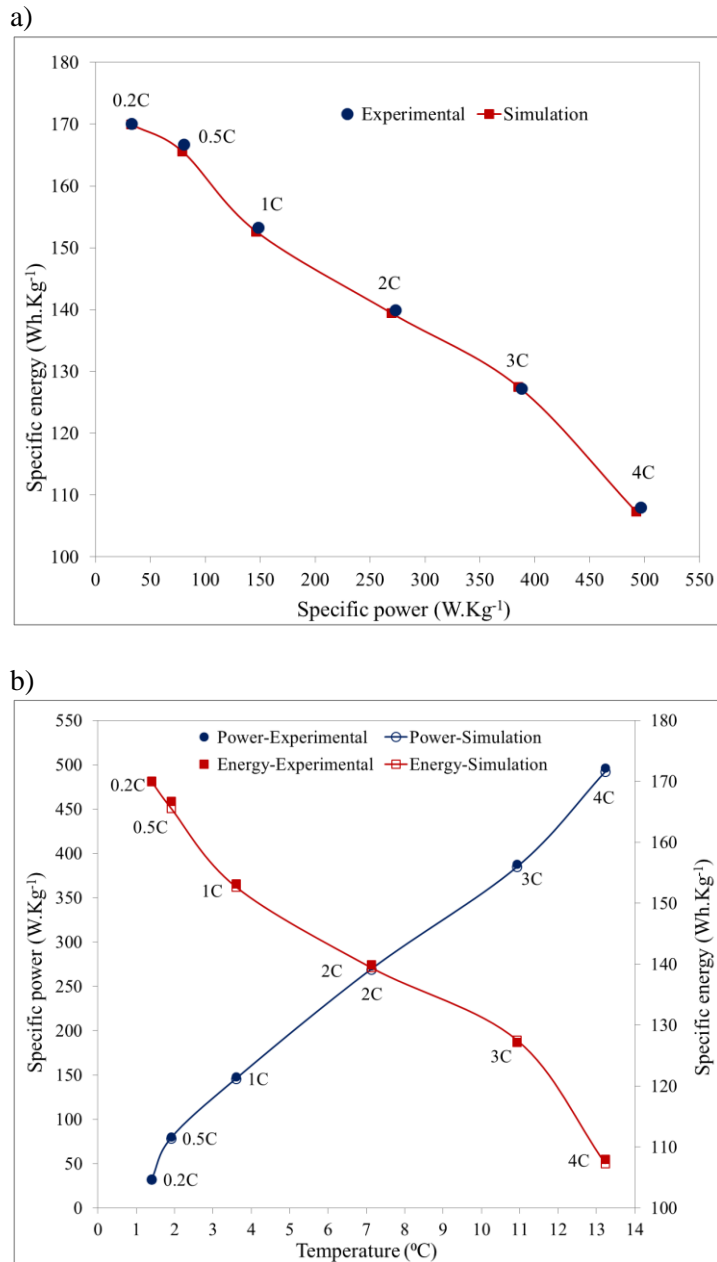


Figure 5.9. Comparison of the measured and simulation data at various rates. Markers are measured data, and solid lines are simulation results. a) Ragone plot. b) Effect of current rate on decreasing energy and rising power.

The energy loss that is mostly thermal loss during the discharge process leads to the variety of discharging time, which results in the variation of discharging capacity. Figure 9.a

shows the comparison of simulated and measured Ragone plot for the different discharge rates, plotted in  $W/kg$  and  $Wh/kg$  of the total weight of the cell (including package). The maximum specific energy of  $170 W/kg$  is detected at the lower rate (0.2C) while the maximum specific power of  $496.3 Wh/kg$  is observed at the higher rate (4C).

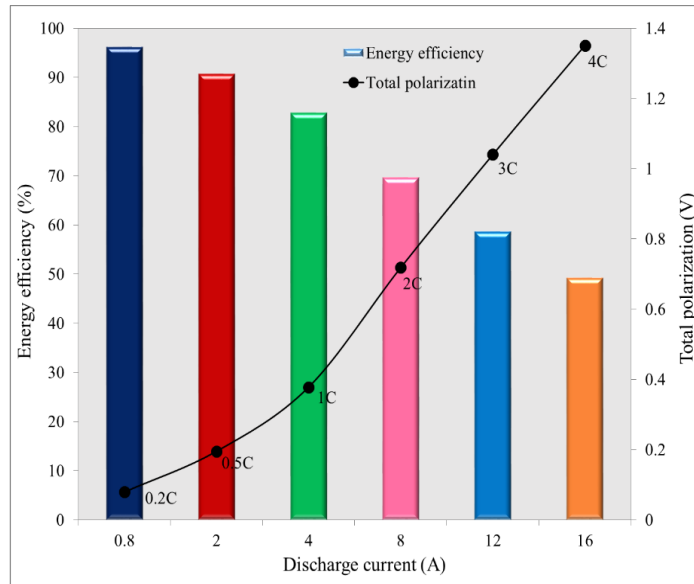


Figure 5.10. Influence of various current value on total polarization and energy efficiency evolutions.

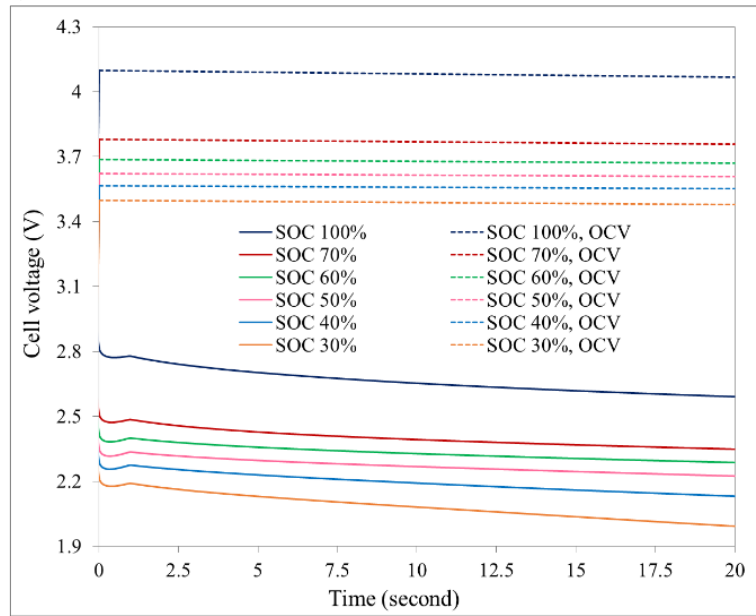
It must be noted that the specific power calculated as the averaged power of the cell at various discharge rates. To explain the dependence of battery performance on the temperature, Figure 5.9.b give the variation of power and energy at different temperatures. It is visible that the specific energy decreased at the higher temperature.

Furthermore, the evolutions of the total polarization and energy efficiency of the cell against the various current value illustrated in Figure 5.10. It shows greater polarization at a higher current value while the energy efficiency is decreasing with the growing of current. The

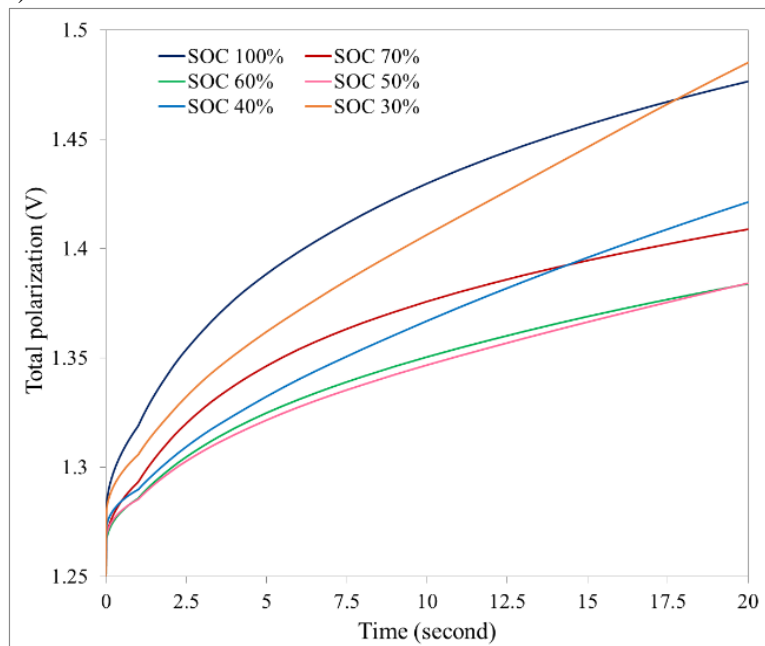


polarization affected the high rate capability batteries even at high current load. The results motivated us to use the computer simulation to analyze the different configuration in an attempt to minimize the voltage drop caused by the internal resistance leading to a larger heat generation at the higher rate. In the model development, it is essential to define the adjustable and fixed parameters when carrying out the optimization process. We assumed a 20 second discharge pulse (16 A) is required to calculate the polarization and internal resistance of the cell at 4C-rate. Then we wish to optimize the cell performance at 4C through varying the initial SOC of the cell, the porosity ( $\epsilon_{psl}$ ) and the particle size ( $r_p$ ) of the positive active electrode material. Also, the model has calculated the energy efficiency of the pulse as a ratio of output energy to input energy. The other parameters provided in Table 5.2 or elsewhere in the study were considered to be fixed, including the temperature, film resistance, material properties, volume fractions, lithium concentration, electrodes and separator thicknesses. Thus, four cases are compared including the original cell design after 20 seconds discharge pulse application. The optimization method exists to vary the adjustable parameters and create a plot for each model to recognize an optimum configuration of the cell. The process is time-consuming even with the computer program, as three design parameters are changing simultaneously. Therefore, to facilitate the optimization process, an analytic charge/discharge model of the ohmically dominated lithium-ion cell have been developed and the optimization solver set up by adding the ordinary differential equations node to the study. This model assumes a variable value diffusion coefficient of lithium in the carbon electrode that is a temperature dependent value that gives the desired gradual loss of capacity, especially at higher discharge rates [37].

a)



b)



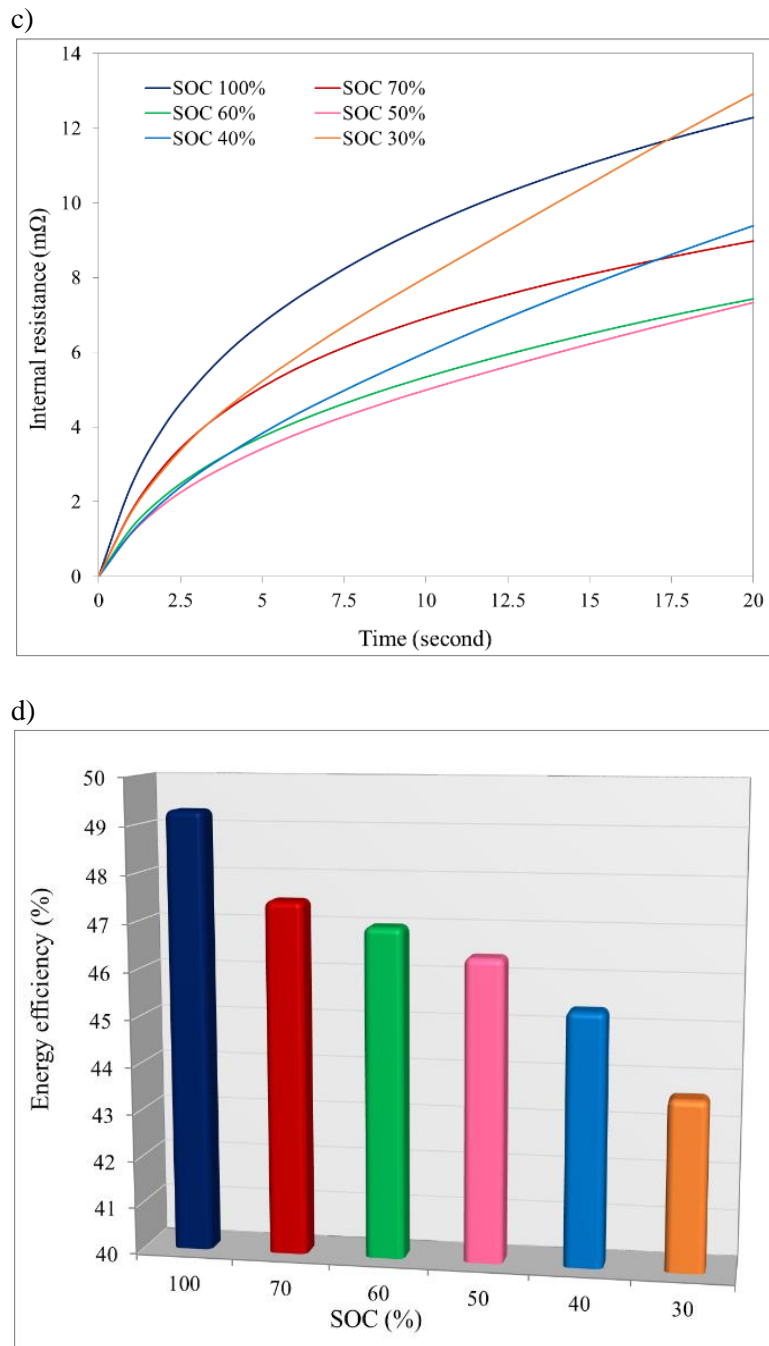


Figure 5.11. Effect of various initial SOC at 4C rate on: a) Discharge voltage and open circuit voltage characteristics, b) Total polarization, c) Internal resistance, and d) Energy efficiency.

In this case, polarization associated with the lithium metal negative electrode and ohmic drop in the separator should be similar. Since the solid-state diffusion limitations are quickly

dominated by the ohmic drop in the solution, we found these restrictions are no longer a primary concern because other phenomena lead to cut-off voltage before the manifestation of diffusion limitations at higher rates.

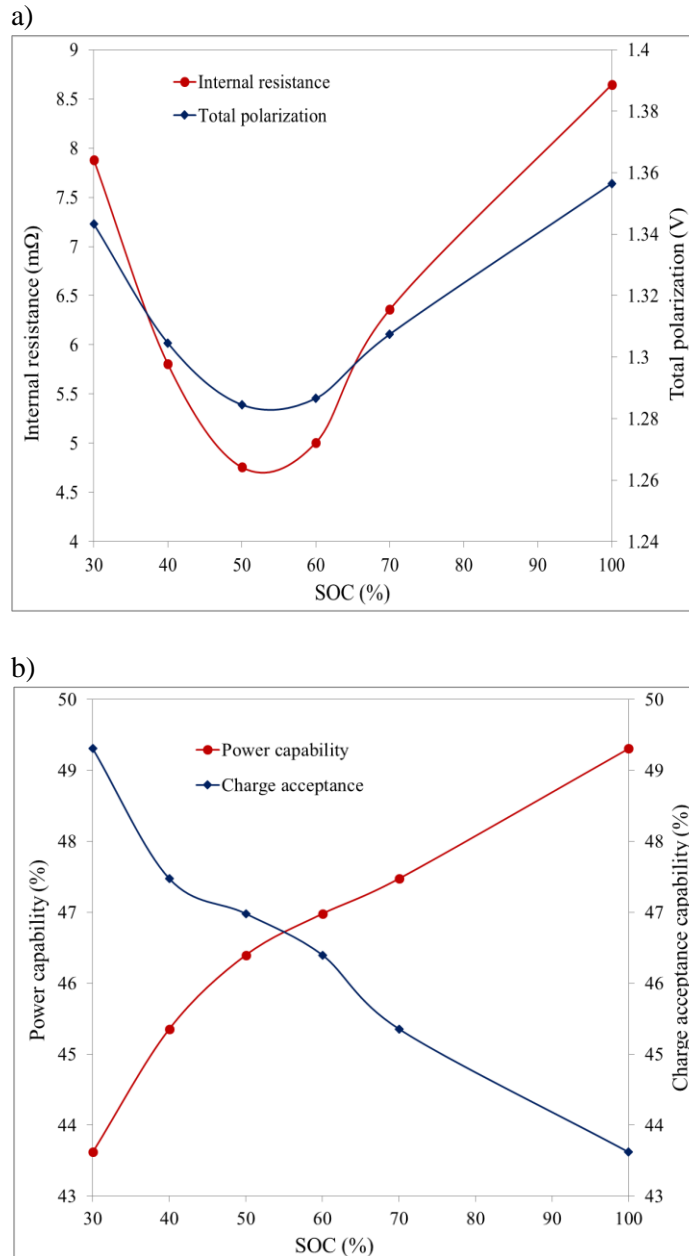


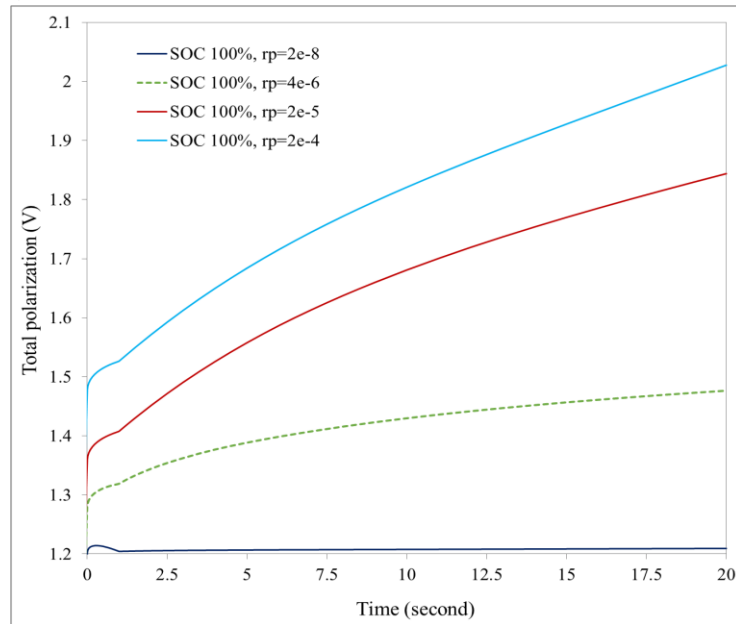
Figure 5.12. a) Averaged internal resistance and polarization value at various SOC. b) Battery charge acceptance indicating the slope of recharge currents at different SOC levels.

Figure 5.11a-c describes the effect of different initial SOC on the discharge voltage and the corresponding OCV, total polarization, internal resistance, and energy efficiency of the cell. From the data in Figure 5.11.a, it is understood that the discharge voltage and energy efficiency of the cell maintain a decreasing trend with reducing the initial SOC. On the other hand, Figure 5.11.b-C shown the polarization voltage and internal resistance are reduced up to SOC of 50%, then raised fast especially at initial SOC of 40% and 30%. The current is fixed to 0A for 20 seconds rest after discharge process, and 20 seconds rest also applied at the end of each charge, to calculate the Coulomb energy efficiency of the cell. The energy efficiency plotted on Figure 5.11.c gives a reliable battery performance on higher initial SOC's mainly at SOC of 100%. The results indicate that the design parameters are affected by the battery initial SOC. Therefore, the effects of SOC on discharge voltage, need to be considered in the modeling.

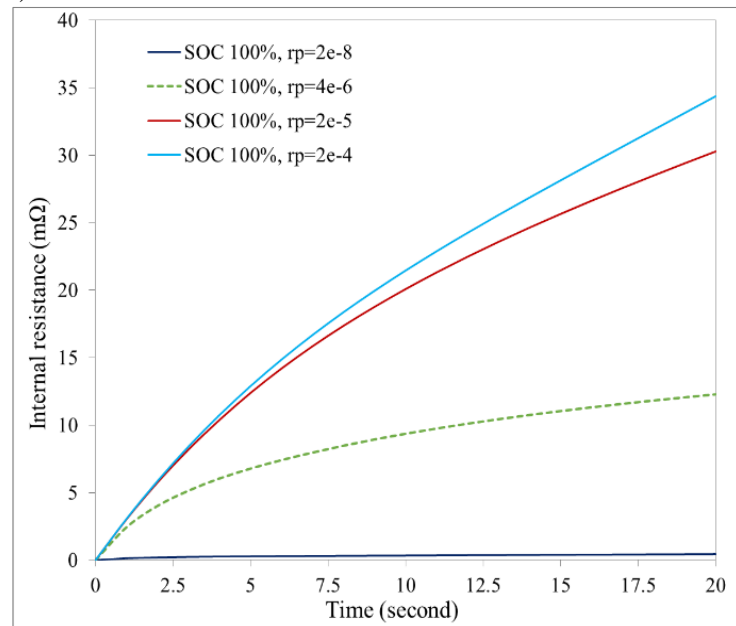
Figure 5.12.a represent the shape of averaged internal resistance curve and averaged polarization curve at different SOC. The capability of the battery to store energy can be affected by temperature, charge rate and state of charge. Likewise, battery recharge behavior was modeled using charge efficiency curve representing the slope of charge acceptance at high SOC shown in Figure 5.12.b.

The polarization of positive electrode is influenced significantly by the variation of the particle size and the porosity.

a)



b)



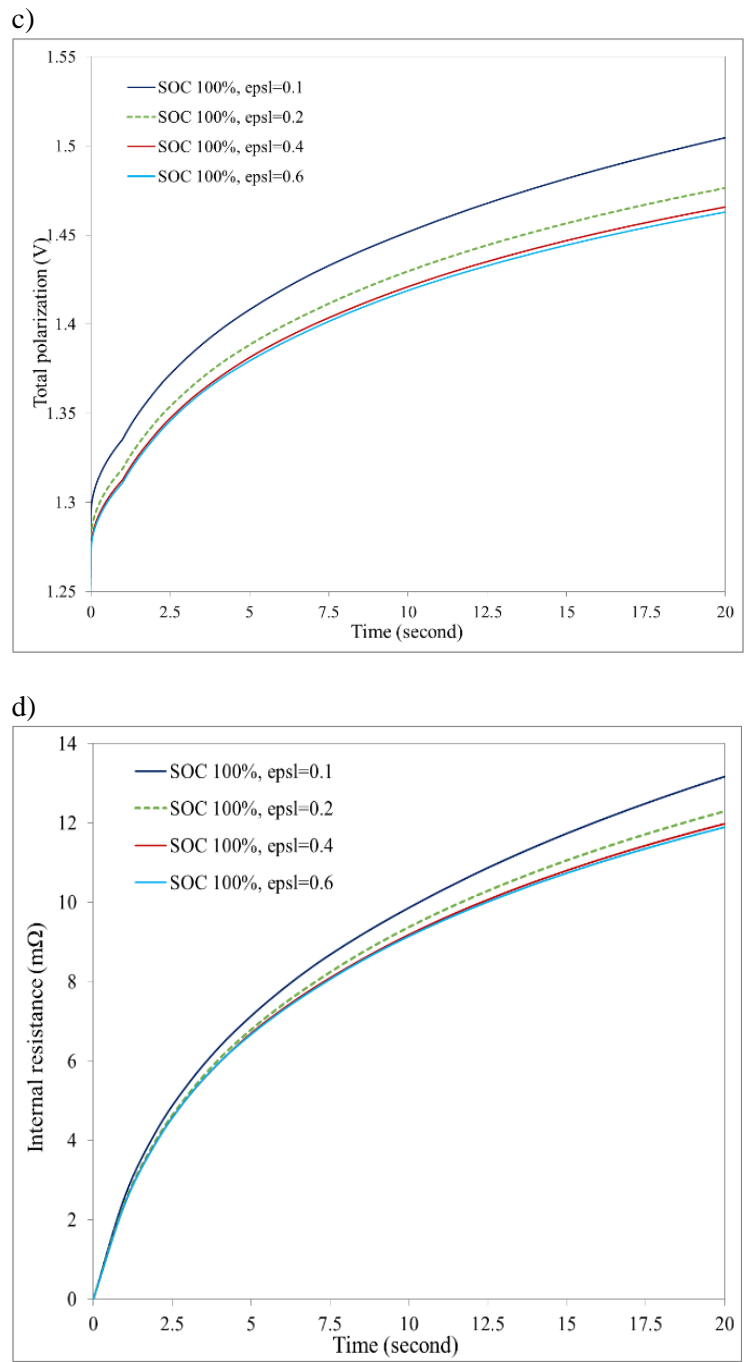


Figure 5.13. Effect of different particle size value of the positive electrode material at SOC of 100%: a) polarization and b) Internal resistance evolutions. Effect of different porosity value of the positive electrode at various SOC on: c) polarization and d) internal resistance evolutions. The dashed lines are the original value from the experimental cell.

The tremendous impact of different particle size value of the positive electrode material at SOC of 100% on polarization and internal resistance growth rate depicted on Figure 5.13.a-b respectively. In this case, the porosity of positive electrode fixed to original value of  $\epsilon_{pos} = 0.2$ , while the positive particle size is varied. The results suggested less polarization (1.2V) and less internal resistance ( $0.4\Omega$ ) at smaller particle size ( $r_p = 2e - 8$ ) than the battery actual size ( $r_p = 4e - 6$ ). The effect of different porosity value of the positive electrode on polarization and internal resistance evolution at SOC of 100% represented on Figure 5.13.c-d correspondingly. The higher porosity,  $\epsilon_{pos} = 0.6$  lowered the value of polarization (1.46V) and internal resistance ( $11\Omega$ ) of the cell considerably. The total polarization and internal resistance using the original particle size and porosity value are 1.4V and  $12\Omega$  correspondingly. The dashed lines in Figure 5.13 presented the initial value from the experimental cell. A thin battery domains, high porosities, and small active material particles decrease the internal resistance of the battery. Therefore, a cell with the different design characteristics has high internal resistance, however, can provide a lot of energy because of large active material particles and compressed electrodes. Accordingly, the battery is either power-optimized or energy-optimized since it cannot have both high energy and high power outputs.

It is understandable that the cell voltage is a function of the initial cell SOC and the material properties. Therefore, the lowered initial cell SOC drops the voltage all through the pulse.

To optimize the battery performance using the proper parameter values, Figure 5.14.a-b shows the averaged values of total polarization and the internal resistance curves against different porosity and particle size of the positive electrode material respectively.



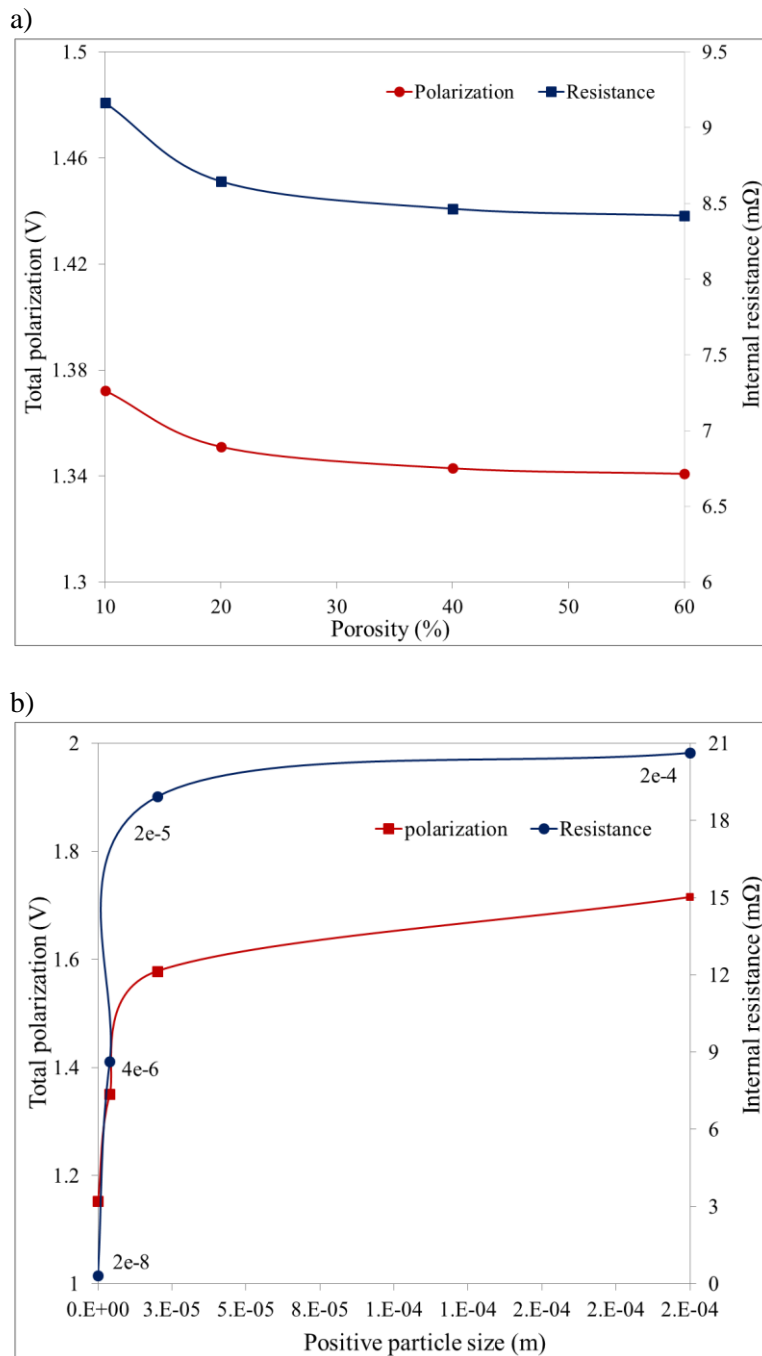
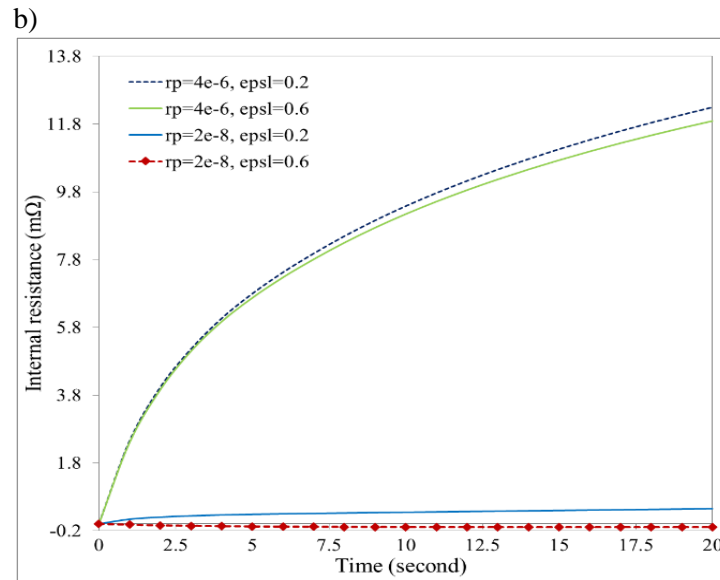
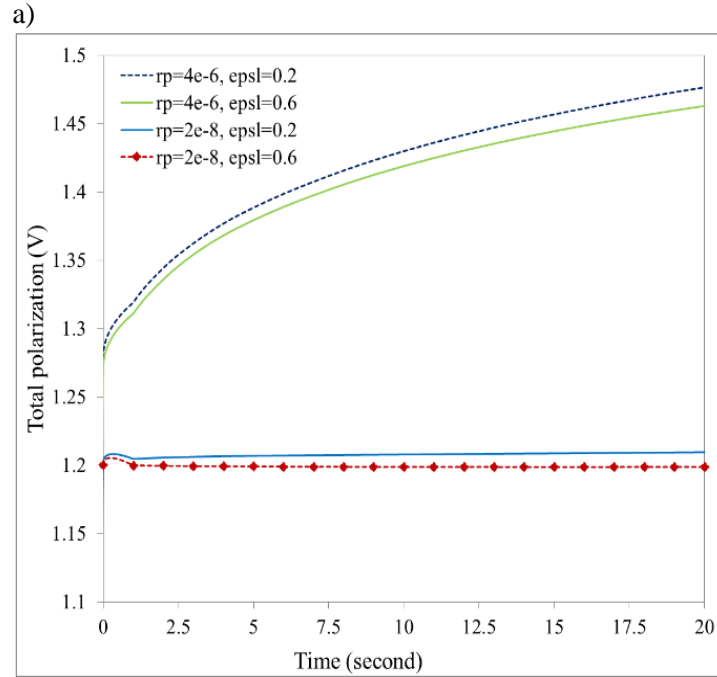


Figure 5.14. Variation of polarization and resistance as a function of: a) porosity and b) particle size.

Finally, the procedure was prepared and characterized to optimize the polarization and resistance changed for four groups of different battery design parameters reported on Figure

5.15.a and Figure 5.15.b. The dashed lines are shown the actual particle size with the actual porosity. The green lines are displayed the actual particle size by the porosity of 60%, and blue lines are presented the particle size of  $2e-8$  by the actual value of porosity.



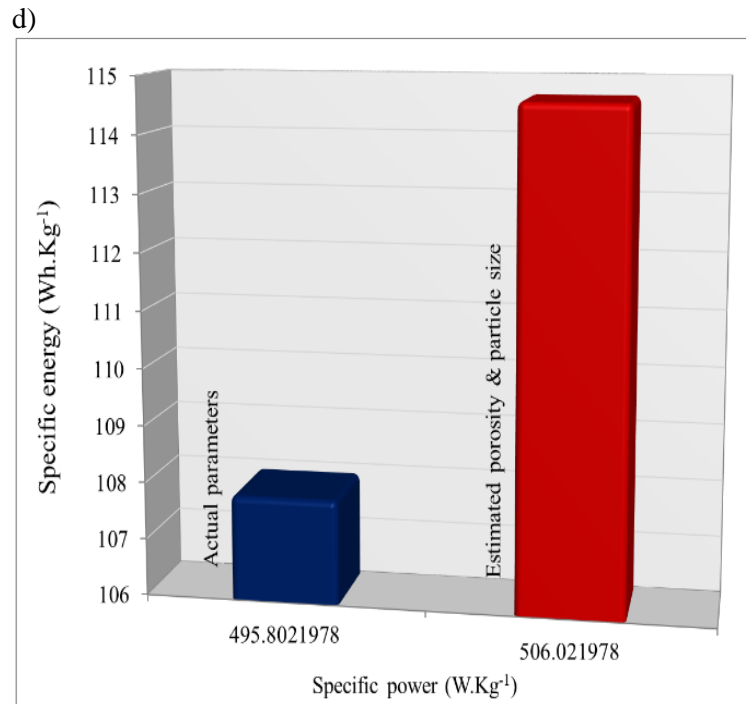
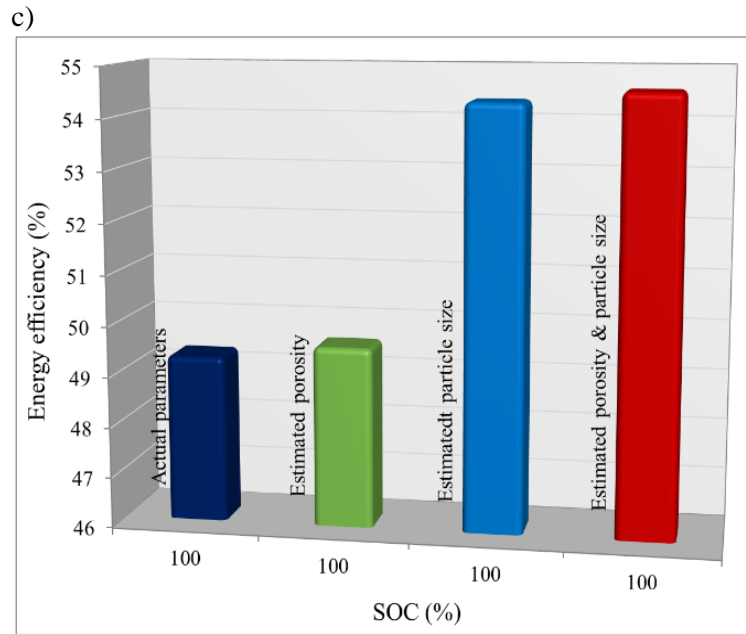


Figure 5.15. Cell response comparison at different design parameters: a) polarization, b) internal resistance. The dashed lines are actual parameters, solid lines are combination of actual parameters and estimated parameters, dashed lines with markers are estimated parameters. c) Comparison of energy efficiency against SOC. d) Comparison of specific energy versus specific power of the cell including actual design parameters and estimated parameters.

The marked dashed lines are shown the particle size of  $2e-8$  by the porosity of 60%. This method can be applied to the different battery types to determine the optimized design parameters. Figure 5.15.c shows the comparison of energy efficiency against SOC of 100% at different design parameters. The energy efficiency of the battery during the pulse should be significantly less than 100% because of the polarization since both the discharge and charge give considerable polarization. The actual parameters show less efficiency (49.3%) while the efficiency in estimated parameters is improved considerably (54.6%).

Moreover, the comparison of specific energy against the specific power applying the actual parameters and the estimated parameters depicted in Figure 5.15.d. The energy efficiency of the cell improved by almost  $6 \text{ Wh.Kg}^{-1}$  and power value optimized  $10 \text{ W.Kg}^{-1}$  using the calculated porosity and particle size.

This analysis method and simplified equivalent circuit presented in this paper have the potentiality to be applied in a battery pack system to optimum its heat generation, safety and lifetime. Therefore, the further analytical study will be deserving doing in future work. Moreover, the procedure of quantifying the internal resistance and the polarization could be improved by dividing the total contact resistance into the positive and negative electrode and extending the analysis method over a 3D model.

## **5.8 Conclusions**

A system based on electrochemical-thermal processes has been developed to study the polarization effects occurring in an NCA cathode base lithium-ion battery cell. Further internal

resistance exists in the experimental cells not primarily predicted by the mathematical modeling. Based on this approach, adding a SEI film resistance at the interface connecting the electrode and the electrolyte revealed a fair agreement between the theory and experimental data. This resistance is defined thoroughly by a SEI film resistance of the electrode particles.

The results represented a much higher rate of heat generation at the electrodes due to electric contact resistance at 4C-rate than heat generation rate at 0.2C-rates. Therefore, a heat flow initiated from the electrodes towards the battery caused a significant polarization at the 4C rate and decreased the battery performance considerably.

To optimize the power capability, the dependency of battery performance to the design parameters including but not limited to SOC, the positive electrode's particle size and porosity of the positive electrode are studied. To conclude it is worth mentioning that an essential effort devoted to optimization of both the energy efficiency and power capability at various stages of SOC, including the electrodes porosity and particle size.

## ***5.9 Acknowledgement***

This effort sponsored by the battery research laboratory at the University of Windsor. The authors would like to thank CMC Microsystems for the provision of products that facilitated this research including CAD tools and design methodology.

## 5.10 References

- [1] J.-M. Tarascon, M. Armand, Issues and challenges facing rechargeable lithium batteries, *Nature*, 414 (2001) 359-367.
- [2] G. Guo, B. Long, B. Cheng, S. Zhou, P. Xu, B. Cao, Three-dimensional thermal finite element modeling of lithium-ion battery in thermal abuse application, *Journal of Power Sources*, 195 (2010) 2393-2398.
- [3] W.F. Howard, R.M. Spotnitz, Theoretical evaluation of high-energy lithium metal phosphate cathode materials in Li-ion batteries, *Journal of Power Sources*, 165 (2007) 887-891.
- [4] W. Fang, O.J. Kwon, C.Y. Wang, Electrochemical–thermal modeling of automotive Li-ion batteries and experimental validation using a three-electrode cell, *International journal of energy research*, 34 (2010) 107-115.
- [5] D. Bernardi, E. Pawlikowski, J. Newman, A general energy balance for battery systems, *Journal of the electrochemical society*, 132 (1985) 5-12.
- [6] R. Heng, Z.M. Razlan, Review of the most recent literature on lithium-ion polymer battery for electric car, *Int. J. Emerg. Technol. Adv. Eng*, 5 (2015).
- [7] M.R. Khan, M.J. Swierczynski, S.K. Kær, Towards an Ultimate Battery Thermal Management System: A Review, *Batteries*, 3 (2017) 9.
- [8] E. Gümüŝsu, *Thermal Modeling of Lithium Ion Batteries*, Fen Bilimleri Enstitüsü, 2017.
- [9] T.M. Bandhauer, S. Garimella, T.F. Fuller, A critical review of thermal issues in lithium-ion batteries, *Journal of the Electrochemical Society*, 158 (2011) R1-R25.
- [10] T.M. Bandhauer, S. Garimella, T.F. Fuller, Temperature-dependent electrochemical heat generation in a commercial lithium-ion battery, *Journal of Power Sources*, 247 (2014) 618-628.
- [11] T. Stuart, F. Fang, X. Wang, C. Ashtiani, A. Pesaran, A modular battery management system for HEVs, *SAE Technical Paper*, 2002.
- [12] Y. Chen, J.W. Evans, Heat Transfer Phenomena in Lithium/Polymer-Electrolyte Batteries for Electric Vehicle Application, *Journal of the Electrochemical Society*, 140 (1993) 1833-1838.

- [13] G.G. Botte, V.R. Subramanian, R.E. White, Mathematical modeling of secondary lithium batteries, *Electrochimica Acta*, 45 (2000) 2595-2609.
- [14] K. Kumaresan, G. Sikha, R.E. White, Thermal model for a Li-ion cell, *Journal of the Electrochemical Society*, 155 (2008) A164-A171.
- [15] G.-H. Kim, A. Pesaran, R. Spotnitz, A three-dimensional thermal abuse model for lithium-ion cells, *Journal of Power Sources*, 170 (2007) 476-489.
- [16] L. Saw, Y. Ye, A. Tay, Electrochemical–thermal analysis of 18650 lithium iron phosphate cell, *Energy Conversion and Management*, 75 (2013) 162-174.
- [17] N. Sato, Thermal behavior analysis of lithium-ion batteries for electric and hybrid vehicles, *Journal of Power Sources*, 99 (2001) 70-77.
- [18] H.-K. Kim, T.-Y. Seong, J.-H. Lim, W.I. Cho, Y.S. Yoon, Electrochemical and structural properties of radio frequency sputtered cobalt oxide electrodes for thin-film supercapacitors, *Journal of power sources*, 102 (2001) 167-171.
- [19] A. Bernardes, D.C.R. Espinosa, J.S. Tenório, Recycling of batteries: a review of current processes and technologies, *Journal of Power Sources*, 130 (2004) 291-298.
- [20] J. Chen, C. Yao, S. Sheu, Y. Chiou, H. Shih, The study of carbon half-cell voltage in lithium-ion secondary batteries, *Journal of power sources*, 68 (1997) 242-244.
- [21] V. Srinivasan, J. Newman, Discharge model for the lithium iron-phosphate electrode, *Journal of the Electrochemical Society*, 151 (2004) A1517-A1529.
- [22] L. Rao, J. Newman, Heat-generation rate and general energy balance for insertion battery systems, *Journal of the Electrochemical Society*, 144 (1997) 2697-2704.
- [23] S. Zhang, K. Xu, T. Jow, The low temperature performance of Li-ion batteries, *Journal of Power Sources*, 115 (2003) 137-140.
- [24] C.-K. Park, Z. Zhang, Z. Xu, A. Kakirde, K. Kang, C. Chai, G. Au, L. Cristo, Variables study for the fast charging lithium ion batteries, *Journal of power sources*, 165 (2007) 892-896.
- [25] C. Daniel, *Materials and processing for lithium-ion batteries*, *Jom*, 2008, pp. 43-48.
- [26] S. Al-Hallaj, R. Kizilel, A. Lateef, R. Sabbah, M. Farid, J.R. Selman, Passive thermal management using phase change material (PCM) for EV and HEV Li-ion batteries, *Vehicle Power and Propulsion*, 2005 IEEE Conference, 2005, pp. 376-380.

- [27] S. Chen, C. Wan, Y. Wang, Thermal analysis of lithium-ion batteries, *Journal of Power Sources*, 140 (2005) 111-124.
- [28] D.H. Jeon, S.M. Baek, Thermal modeling of cylindrical lithium ion battery during discharge cycle, *Energy Conversion and Management*, 52 (2011) 2973-2981.
- [29] R. Zhao, J. Liu, J. Gu, The effects of electrode thickness on the electrochemical and thermal characteristics of lithium ion battery, *Applied Energy*, 139 (2015) 220-229.
- [30] P. Taheri, A. Mansouri, M. Yazdanpour, M. Bahrami, Theoretical analysis of potential and current distributions in planar electrodes of lithium-ion batteries, *Electrochimica Acta*, 133 (2014) 197-208.
- [31] P. Taheri, A. Mansouri, M. Yazdanpour, M. Bahrami, Potential and Current Distributions in Planar Electrodes of Lithium-Ion Batteries, Meeting Abstracts, The Electrochemical Society, 2014, pp. 397-397.
- [32] M. Yazdanpour, P. Taheri, A. Mansouri, M. Bahrami, A distributed analytical electro-thermal model for pouch-type lithium-ion batteries, *Journal of The Electrochemical Society*, 161 (2014) A1953-A1963.
- [33] S. Du, M. Jia, Y. Cheng, Y. Tang, H. Zhang, L. Ai, K. Zhang, Y. Lai, Study on the thermal behaviors of power lithium iron phosphate (LFP) aluminum-laminated battery with different tab configurations, *International Journal of Thermal Sciences*, 89 (2015) 327-336.
- [34] K. Somasundaram, E. Birgersson, A.S. Mujumdar, Thermal–electrochemical model for passive thermal management of a spiral-wound lithium-ion battery, *Journal of Power Sources*, 203 (2012) 84-96.
- [35] W. Gu, C.-Y. Wang, Thermal and electrochemical coupled modeling of a lithium-ion cell, *Proc.-Electrochem. Soc.*, 99 (2000) 748-762.
- [36] M. Doyle, T.F. Fuller, J. Newman, Modeling of galvanostatic charge and discharge of the lithium/polymer/insertion cell, *Journal of the Electrochemical Society*, 140 (1993) 1526-1533.
- [37] M. Doyle, J. Newman, A.S. Gozdz, C.N. Schmutz, J.M. Tarascon, Comparison of modeling predictions with experimental data from plastic lithium ion cells, *Journal of the Electrochemical Society*, 143 (1996) 1890-1903.
- [38] S. Basu, K.S. Hariharan, S.M. Kolake, T. Song, D.K. Sohn, T. Yeo, Coupled electrochemical thermal modelling of a novel Li-ion battery pack thermal management system, *Applied Energy*, 181 (2016) 1-13.



- [39] M. Guo, R.E. White, A distributed thermal model for a Li-ion electrode plate pair, *Journal of Power Sources*, 221 (2013) 334-344.
- [40] U.S. Kim, C.B. Shin, C.-S. Kim, Modeling for the scale-up of a lithium-ion polymer battery, *Journal of Power Sources*, 189 (2009) 841-846.
- [41] S. Mischie, L. Toma, Behavior of the Lead Acid Battery after the Rest Period, *WSEAS Trans. on Power Systems*, 3 (2008) 111-117.
- [42] F. Jiang, P. Peng, Y. Sun, Thermal analyses of LiFePO<sub>4</sub>/graphite battery discharge processes, *Journal of Power Sources*, 243 (2013) 181-194.
- [43] K.E. Thomas-Alyea, J. Newman, *Electrochemical Systems*, John Wiley & Sons, Inc., Hoboken, NJ, 2004.
- [44] D.R. Baker, M.W. Verbrugge, Temperature and Current Distribution in Thin-Film Batteries, *Journal of the Electrochemical Society*, 146 (1999) 2413-2424.
- [45] S.-C. Chen, Y.-Y. Wang, C.-C. Wan, Thermal analysis of spirally wound lithium batteries, *Journal of the Electrochemical Society*, 153 (2006) A637-A648.
- [46] M. Yazdanpour, P. Taheri, M. Bahrami, A computationally-effective thermal model for spirally wound nickel-metal hydride batteries, *Journal of The Electrochemical Society*, 161 (2014) A109-A117.
- [47] P. Taheri, M. Bahrami, Temperature rise in prismatic polymer lithium-ion batteries: An analytic approach, *SAE International Journal of Passenger Cars-Electronic and Electrical Systems*, 5 (2012) 164-176.
- [48] A. Nyman, T.G. Zavalis, R. Elger, M. Behm, G. Lindbergh, Analysis of the polarization in a Li-ion battery cell by numerical simulations, *Journal of the Electrochemical Society*, 157 (2010) A1236-A1246.
- [49] I. Bloom, A.N. Jansen, D.P. Abraham, J. Knuth, S.A. Jones, V.S. Battaglia, G.L. Henriksen, Differential voltage analyses of high-power, lithium-ion cells: 1. Technique and application, *Journal of Power Sources*, 139 (2005) 295-303.
- [50] L.C. Casals, A.M.S. González, B.A. García, J. Llorca, PHEV Battery Aging Study Using Voltage Recovery and Internal Resistance From Onboard Data, *IEEE Transactions on Vehicular Technology*, 65 (2016) 4209-4216.
- [51] Y. Kobayashi, H. Miyashiro, K. Kumai, K. Takei, T. Iwahori, I. Uchida, Precise Electrochemical Calorimetry of LiCoO<sub>2</sub>/Graphite Lithium-Ion Cell Understanding Thermal Behavior and Estimation of Degradation Mechanism, *Journal of The Electrochemical Society*, 149 (2002) A978-A982.

- [52] R. Wright, J. Christophersen, C. Motloch, J. Belt, C. Ho, V. Battaglia, J. Barnes, T. Duong, R. Sutula, Power fade and capacity fade resulting from cycle-life testing of advanced technology development program lithium-ion batteries, *Journal of Power Sources*, 119 (2003) 865-869.
- [53] S. Brown, N. Mellgren, M. Vynnycky, G. Lindbergh, Impedance as a tool for investigating aging in Lithium-ion porous electrodes II. Positive electrode examination, *Journal of The Electrochemical Society*, 155 (2008) A320-A338.
- [54] B.Y. Liaw, E.P. Roth, R.G. Jungst, G. Nagasubramanian, H.L. Case, D.H. Doughty, Correlation of Arrhenius behaviors in power and capacity fades with cell impedance and heat generation in cylindrical lithium-ion cells, *Journal of power sources*, 119 (2003) 874-886.
- [55] J. Jiang, Q. Liu, C. Zhang, W. Zhang, Evaluation of acceptable charging current of power Li-ion batteries based on polarization characteristics, *IEEE Transactions on Industrial Electronics*, 61 (2014) 6844-6851.
- [56] V. Johnson, Battery performance models in ADVISOR, *Journal of power sources*, 110 (2002) 321-329.
- [57] C. Birkl, E. McTurk, M. Roberts, P. Bruce, D. Howey, A parametric open circuit voltage model for lithium ion batteries, *Journal of The Electrochemical Society*, 162 (2015) A2271-A2280.
- [58] D. Dees, E. Gunen, D. Abraham, A. Jansen, J. Prakash, Alternating current impedance electrochemical modeling of lithium-ion positive electrodes, *Journal of the Electrochemical Society*, 152 (2005) A1409-A1417.
- [59] K. Li, K.J. Tseng, Energy efficiency of lithium-ion battery used as energy storage devices in micro-grid, *Industrial Electronics Society, IECON 2015-41st Annual Conference of the IEEE, IEEE*, 2015, pp. 005235-005240.
- [60] K.S. Ng, C.-S. Moo, Y.-P. Chen, Y.-C. Hsieh, Enhanced coulomb counting method for estimating state-of-charge and state-of-health of lithium-ion batteries, *Applied energy*, 86 (2009) 1506-1511.
- [61] A.A. Pesaran, Battery thermal models for hybrid vehicle simulations, *Journal of power sources*, 110 (2002) 377-382.

## CHAPTER 6

### CONCLUSIONS AND FUTURE RESEARCH DIRECTIONS

---

#### *6.1 Summary of thesis*

Lithium-ion batteries are being used increasingly worldwide as energy storage system for EVs/HEVs and designs are being changed continuously to improve the electrochemical performance of the battery with adopting new and improved materials.

As demonstrated by this study, the thermal management of Li-ion batteries plays a significant role in battery cycle life, safety issues, and reliability. Consequently, an essential diagnostic examination and practical modeling attempts are required to fully understand the thermal characteristics of the Li-ion batteries at the different operating conditions.

This study intended to develop a modeling system as a fast simulation tool to predict the temperature distribution within the prismatic batteries and optimal design configuration for the next generation of lithium ion battery. Therefore the models proposed in this research has been divided into analytical solutions and numerical simulations.

The analytical model presented in the first part of the study described the distribution of potential, current density, and temperature of the battery during charge/discharge processes. First, a one-dimensional multiphysics model is developed to study the electrochemical-thermal characteristics. Next, the solution is adjusted to study a three-dimensional electro-thermal model to demonstrate the most efficient estimation of the system temperature response, overall

heat generation and heat distribution inside a pouch-type Li-ion cell controlled by the convective cooling on its surfaces.

The results are in agreement with the data obtained from constant current discharge experiments. The results indicated that the most heat generation in the battery arises close to the battery tabs, where the ohmic heat occurs as a result of non-uniform current distribution and local internal resistance, and the entropic heat due to heat of reaction linked to the type electrode materials.

In the second part of the study, an experimentally validated modeling technique has been developed to investigate and optimize performance of the battery at various discharge current rates. To achieve this, the resistance is determined by adding a SEI film to the electrode/electrolyte interface. The model is estimated the capacity, energy efficiency, polarization, internal resistance, rate capability, heat distribution, and the optimized achievable specific energy and power capability of a lithium-ion cell. The results expressed the battery performance is affected by a significant polarization due to the heat flow through the battery, especially at higher C rates. Eventually, the idea of modifying the system parameters such as porosity and particle size has been used to optimize the energy efficiency and power value of the cell at various Power/Energy ratios for different applications.

## ***6.2 Suggested Future Work***

The electrochemical-thermal performance of the LIBs has been investigated in the current study. The battery performance is determined as a function of the SOC, the design parameters,

and the current rates while the impact of the various initial temperature has been neglected which may not be appropriate for high power applications.

Therefore, more experimental investigations at various initial temperature are required to include this influence. Furthermore, it is a good idea to add the effect of initial temperature on SOH of the battery in the presented model. Also, the cell model can be utilized to develop a 3D BMS for the battery module and pack for monitoring the SOC, SOH and heat generation across the system at different operating conditions. The ECT model has the potential to be customized to other types of battery, in terms of battery chemistry and geometry for the next generation power sources.

To design an optimal BTMS, it is worthy to consider the impact of tab location for large format LIB for improving uniformity of current distribution and heat response of the system.

## **VITA AUCTORIS**

---

Maryam Ghalkhani received the B.Sc. degrees in electrical engineering in 2010 in Iran. From there she went on to the Université du Québec à Chicoutimi (UQAC) where she obtained a M.Sc. in electrical engineering in 2012. She is currently a candidate for Doctoral degree in electrical engineering at the University of Windsor, Windsor, ON, Canada and is graduating in 2017. Thermal modeling and optimization of Lithium-Ion batteries for electric vehicles is her main research interest.